Exciton Dynamics in Alternative Solar Cell Materials: Polymers, Nanocrystals, and Small Molecules

A THESIS

SUBMITTED TO THE FACULTY OF THE GRADUATE SCHOOL

OF THE UNIVERSITY OF MINNESOTA

BY

Thomas J. Pundsack

IN PARTIAL FULFILLMENT OF THE REQUIREMENTS

FOR THE DEGREE OF

DOCTOR OF PHILOSOPHY

David A. Blank

July, 2014

In memory of Matthew Carlson who introduced me to physics.

Acknowledgements

While preparing this thesis I have tried to untangle the path I have taken in order to give proper credit to those who have helped me along the way. While the list is long, I do not want to imply that any single individual was not imperative to the success I have been lucky to attain.

First, I would like to thank the physics faculty at St. Cloud State University for not only giving me the necessary background in physics but also for encouraging me to pursue a career in science. In particular I need to thank Sneh Kalia whose quantum class convinced me to study physics, John Harlander who introduced me to advanced optics through interesting lectures and unique experiments, Kevin Haglin who's instruction taught me how to approach and comprehend advanced topics, and Russ Lidberg who introduced me to the pain of experimental research and the associated joy of finally getting it to work.

At the University of Minnesota the members of the Blank Group have been integral to the research presented in this thesis. When I joined the group Matt Ammend, Andy

Healy, Jon Hinke, and Adam Huss were quick to welcome me and introduce me to ultrafast spectroscopy. They, along with other members of the Blank Group including Francesc Domenech, Benj Fitzpatrick, Philip Goff, Matthew Hauwiller, Lingxun Kong, Eric Nordland, Emily Pelton, Toni Sanchez-Diaz, and Yefeng Wang, contributed to this work with illuminating discussions and many hours of work keeping the laser happy. Thank you all very much! Lingxun Kong's contribution to Chapter 3 of this work were extensive. Lingxun made the majority of the P3HT thin films studied and performed many of the steady state spectroscopic measurements on the films. Jon Hinke performed the ultrafast spectroscopy on the PtOEP films and helped develop the analysis schemes presented in Chapter 6. It was a pleasure to work closely with both of you!

In my graduate work I have also been lucky to work with great collaborators outside of the Blank Group. Dr. Zhongjian Hu, Professor David Vanden Bout, and Professor Peter Rossky at the University of Texas at Austin provided the triblock polymer sample presented in Chapter 4 and were part of many stimulating discussions. Boris Chernomordik synthesized and characterized the CZTS nanocrystals and, along with Professor Eray Aydil, assisted in forming conclusions about the ultrafast data in Chapter 5. In addition to producing optically clear PtOEP films, discussions with Professor Russell Holmes, Wade Luhmen, and Matt Menke helped clear up many confusions concerning annihilation, kinetics, and energy transfer. The ideas that grew from these discussions are presented in Chapter 6. I would also like to thank Aaron Massari and his research group who offered insight in group meetings and conversations.

My parents and sister have given me unwavering support throughout my (many) years in school. They were my first teachers and, as such, are the basis of all of this work. Thank you so much for everything! My wife Kaylan should be given a whole chapter for all she has done for me, but it will have to be sufficient to say that I wouldn't have made it through my first month of graduate school without her.

Finally, I would like to thank Professor David Blank who has been a model adviser. Professor Blank always made time for discussions and consistently had new ideas or interpretations when things got difficult. He has taught me so much and I will continue to glean knowledge from him for as long as I can. Thank you for making my time at the University of Minnesota enlightening and enjoyable.

Dedication

This thesis is dedicated to my wonderful wife Kaylan who has patiently listened to talks, graciously paid the mortgage, and lovingly supported me throughout my time in graduate school. Thank you.

Abstract

To keep fossil fuel usage in 2040 even with 2010 usage, 50% of global energy will need to come from alternative sources such as solar cells. While the photovoltaic market is currently dominated by crystalline silicon, there are many low-cost solar cell materials such as conjugated polymers, semiconductor nanocrystals, and organic small molecules which could compete with fossil fuels. To create cost-competitive devices, understanding the excited state dynamics of these materials is necessary.

The first section of this thesis looks at aggregation in poly(3-hexylthiophene) (P3HT) which is commonly used in organic photovoltaics. The amount of aggregation in P3HT thin films was controlled by using a mixture of regioregular and regiorandom P3HT. Even with few aggregates present, excited states were found to transfer from amorphous to aggregate domains in $<$50 fs which could indicate efficient long-range energy transfer.

To further study P3HT aggregation, a triblock consisting of two P3HT chains with a coil polymer between them was investigated. By changing solvents, aggregation was induced in a stable and reversible manner allowing for spectroscopic studies of P3HT aggregates in solution. The polarity of the solvent was adjusted, and no change in excited state dynamics was observed implying the excited state has little charge-transfer character.

Next, the conduction band density of states for copper zinc tin sulfide nanocrystals (CZTS NCs) was measured using pump-probe spectroscopy and found to be in agreement with theoretical results. The density of states shifted and dilated for smaller NCs indicative of quantum confinement. The excited state lifetime was found to be short ($\sim$20 ps) and independent of NC size which could limit the efficiency of CZTS photovoltaic devices.

Finally, triplet-triplet annihilation (TTA) was studied in platinum octaethylporphyrin (PtOEP) thin films. By analyzing pump-probe spectra, the product of TTA in PtOEP thin films was assigned to a long-lived metal-centered state. To elucidate the mechanism of TTA, the annihilation dynamics were modeled using second order kinetics as well as Förster and Dexter energy transfer. Dexter energy transfer provided the best fits and the most reasonable fitting parameters.

Contents

List of Tables

List of Figures

List of Abbreviations

ΔOD	change in optical density
CIGS	copper indium gallium selenide
CW	continuous wave (laser)
CZTS	copper zinc tin sulfide
DSC	differential scanning calorimetry
DSSC	dye sensitized solar cell
$\mathbf{E}_g$	band gap
ESA	excited state absorption
FRET	Förster resonance energy transfer
FWHM	full width at half maximum
GSH	ground state hole
HOMO	highest occupied molecular orbital
LED	light emitting diode
LUMO	lowest unoccupied molecular orbital
NC	nanocrystal
NOPA	noncollinear optical parametric amplifier (amplification)
OLED	organic light emitting diode
OPV	organic photovoltaic (device)
P3HT	poly(3-hexylthiophene)
PL	photoluminescence
PMT	photomultiplier tube
P*t*BA	poly(*tert*-butyl acrylate)
PtOEP	platinum octaethylporphyrin
PV	photovoltaic (device)
QD	quantum dot

QY	quantum yield (fluorescence)
regen	regenerative amplifier
rrP3HT	regioregular poly(3-hexylthiophene)
rraP3HT	regiorandom poly(3-hexylthiophene)
SE	stimulated emission
SHG	second harmonic generation
Ti:Sapph	titanium sapphire (crystal)
TTA	triplet-triplet annihilation

Chapter 1

Introduction

1.1 Energy Outlook

Global energy demand continues to increase with usage expected to rise from 17.5 TW in 2010 to 27.4 TW in 2040, an increase of 55% over 30 years.[1] With over 60% of energy currently being produced by fossil fuels (Figure 1.1), the increase in global energy usage will substantially increase the demand for fossil fuels, resulting in increased costs and greenhouse gas emissions.[2;3] In order to maintain an acceptable amount of atmospheric CO_2, emission-free energy sources will need to replace a large portion of fossil fuel combustion, providing at least 10-20 TW of clean power.[4;5]

An enlightening, if somber, look at different options to reduce carbon emissions was presented by Nathan Lewis in 2007.[6] Many energy sources do not scale to the required 10-20 TW: biomass would only account for 5 TW if all non-food producing rain-fed

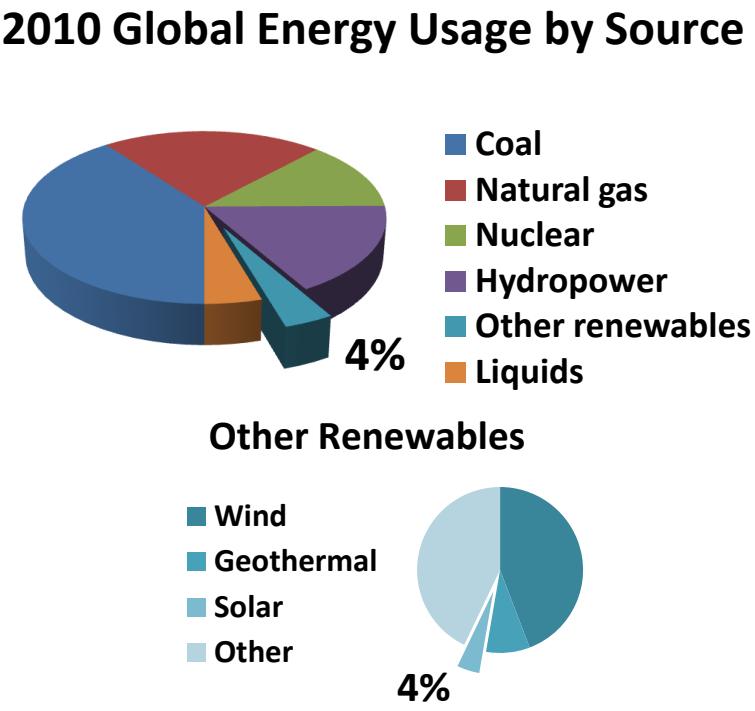

Figure 1.1: Global energy use by source for 2010 (top). Further breakdown of 'other renewable' category (bottom). Data from the International Energy Outlook 2013.[1]

land was converted to energy farmland, only 2 TW of wind power would be generated if turbines were built on all suitable locations globally, and if every feasible waterway was dammed less than 1 TW of power would be produced. While nuclear power is scalable, in order to reach 10 TW a nuclear plant would need to be commissioned every day for 25 years. Furthermore, all available terrestrial uranium would only provide 10 TW of power for 10 years. Research into the viability and safety of other radioactive materials would be necessary for nuclear to be a long-term energy solution, further delaying its implementation.

When compared to other alternative sources, solar energy is more scalable and has a much higher theoretical limit. The capacity of solar energy is far above the global energy demand due to the large amount of energy (∼120,000 TW) supplied to the earth by the sun each year.[3] Even with this large energy source, solar power makes up less than 0.2% of the global energy usage as shown in Figure 1.1. This is due to the current high cost of implementing solar technologies. The photovoltaic (PV) market is dominated by crystalline silicon which costs \$0.25-\$0.50/kWh compared to \$0.01-\$0.08/kHh for fossil fuel combustion.[7] From a purely financial standpoint, solar power can not achieve widespread usage in its current form.

To become competitive with fossil fuels, PV efficiencies need to substantially increase or prices need to drastically decrease. Because silicon PV efficiencies, currently ∼25%, are approaching the theoretical Shockley-Queisser limit of 29% further increases in device performance are difficult and costly to achieve.[8;9] Furthermore, production of silicon solar cells requires high vacuum and clean room facilities which makes decreasing costs difficult, especially to the extent required to compete with fossil fuels. Thus, many new materials have been studied for use in PV devices over the past two decades.

Thin film solar cells using copper indium gallium selenide (CIGS) and cadmium telluride (CdTe) have shown promise with efficiencies reaching 20% and production costs below crystalline silicon.[11] The long term viability of CIGS and CdTe is still in question due to the scarcity of indium and tellurium as well as the high toxicity of cadmium.[12]

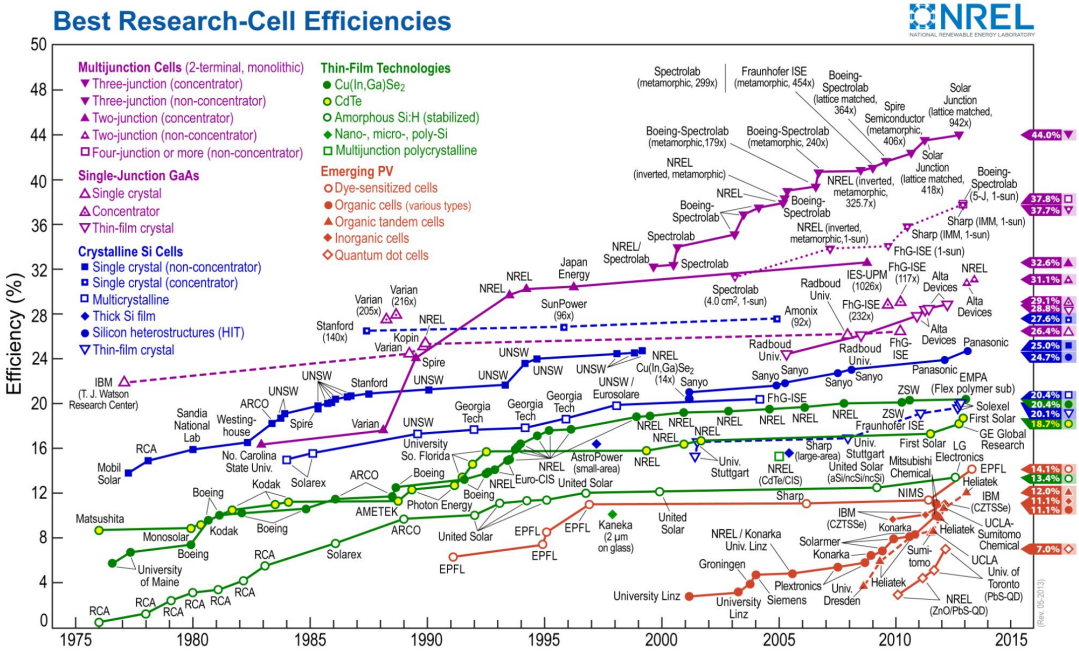

Figure 1.2: Record solar cell efficiencies for different PV technologies. Figure reproduced from NREL.[10]

Research has turned to alternative earth-abundant non-toxic materials including organics, quantum dots, and dye-sensitizers. While the efficiencies of devices made with these alternative materials are relatively low, improvements have occurred over the years as shown by the red symbols in Figure 1.2. Furthermore, the production costs are much lower than silicon. For example, assuming only 5% efficiencies and 5 year device lifetimes organic solar cells would cost \$0.49-\$0.85/kWh which is approaching the cost of silicon solar cells. With an efficiency increase to 15% and an improved

lifetime of 20 years, organic device prices would plummet to \$0.07-\$0.13/kWh.[7] This not only outpaces silicon but also compete with fossil fuels.

Continued research into alternative solar cell materials is an important step to reduce fossil fuel usage and minimize atmospheric CO_2. This thesis will focus on three different alternative materials: the conjugated polymer poly(3-hexylthiophene) (P3HT) which is commonly used as an electron donating material in organic solar cells, copper zinc tin sulfide nanocrystals (CZTS NCs) which can be used to make thin film solar cells similar to CIGS or CdTe, and platinum octaethylporphyrin (PtOEP) a small molecule used in organic solar cells. All of these materials have shown promise in PV devices, but increased efficiencies are required for commercial viability. The work presented here investigates the dynamics of excited species in these materials to understand the underlying physics and help optimize future device performance.

1.2 Solar Cell Operation

Understanding solar cell operation is necessary to investigate the efficiency difference between silicon solar cells and solar cells made with alternative materials. This section will give a brief overview of silicon and organic solar cell operation, focusing on the differences between the two and sources of loss.

1.2.1 Conventional Silicon Solar Cells

A conventional silicon solar cell consists of p-n junction created within a silicon single crystal.[13] The p-n junction is created by atomically doping a silicon crystal such that one region has added electrons (n-type) and one region is missing electrons (p-type). The missing electrons in the p-type silicon leave empty sites in the lattice which can be thought of as positive charges called holes. At the interface between the regions, charges diffuse between the n-type and p-type silicon and recombine. As charges cross the interface an electric field is built up opposing further diffusion. This creates a zone with no extra charges called the depletion region (Figure 1.3).

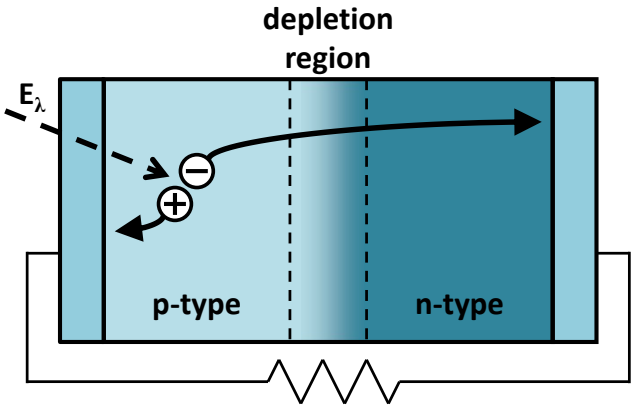

Figure 1.3: Schematic of a conventional silicon solar cell showing light (dashed line) being absorbed by the cell creating free charges which move through the device, are collected at electrodes, and drive an external load.

When light is absorbed by the device an electron is excited from the valence band, which is filled with electrons, to the empty conduction band. This excitation leaves a

hole in the valence band. The high dielectric constant of silicon screens the electron and hole from influencing each other, creating free charges. Due to the built in electric field, the depletion region acts as a diode sweeping electrons to the n-type silicon and holes to the p-type silicon as shown in Figure 1.4. The charges are then collected at the electrodes giving an electrical current that can be used to drive an external circuit.

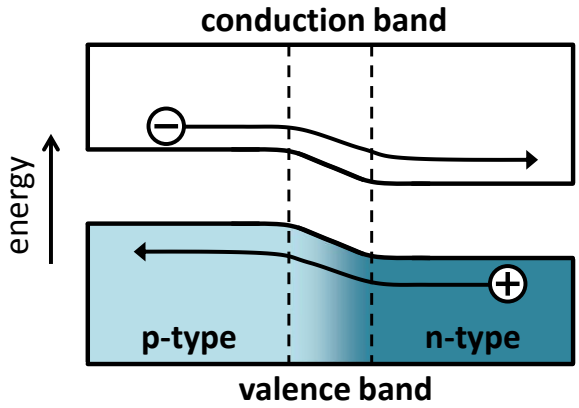

Figure 1.4: Energy diagram for a p-n junction in a conventional solar cell showing electrons being swept to the n-type silicon and hole being swept to the p-type silicon. The dashed lines represent the depletion region.

Figure 1.5 shows the three main sources of loss that prevent device efficiency from surpassing the Shockley-Queisser limit.[14] First, silicon can only absorb light with certain energies. The threshold for absorption is determined by the energy spacing between the valence and the conduction band, known as the bandgap (E_g). Light in the solar spectrum with energy less than E_g will not be absorbed as there is no state for the electron to occupy in the energy gap. Second, when high energy light is absorbed, any

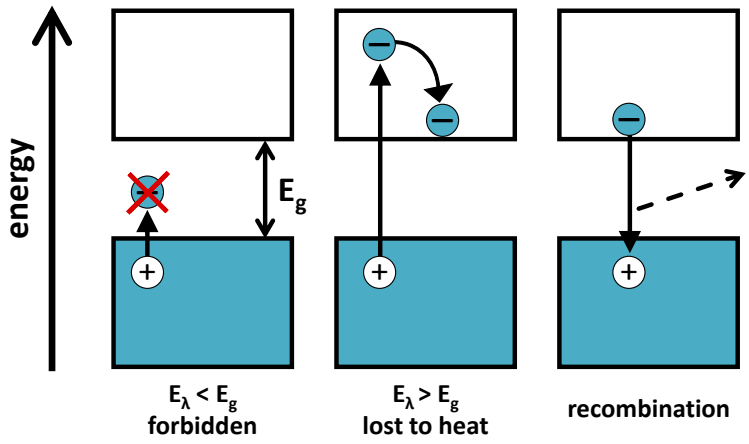

Figure 1.5: Three sources of loss in solar cells. Valence bands (inorganic) or HOMOs (organic) are depicted in teal while conduction bands (inorganic) or LUMOs (organic) are depicted in white.

energy above E_g is lost to heat as the electrons rapidly cool to the conduction band minimum. Finally, energy is lost when electrons and holes recombine before they are harvested. The energy lost during recombination is lost to heat or converted to light. Because these sources of loss are imposed by the physics of the processes occurring, no amount of optimization will be able to increase efficiencies above the Shockley-Queisser limit, although changes in the device architecture or materials used may be able to circumvent the limitations.

1.2.2 Organic Solar Cells

Many underlying principles are shared between organic and silicon solar cells including the need to absorb light and collect charges. One of the main differences is the nature

of the excited state created by light absorption. As stated above, when light is absorbed by silicon free charges are created because the electron and hole are screened from each other due to the high dielectric constant of silicon. Organic materials have much lower dielectric constant and, therefore, less screening.[15] Because of this, the electron and hole are coulombically attracted to each other which creates a bound electron-hole pair called an exciton. Because excitons are neutral species (being made up of the negatively charged electron and the positively charged hole) they can not be used to do electrical work. Thus, the charges in the exciton need to be separated in order to power an external load.

One way the charges can separate is at an interface between two materials, an electron acceptor and an electron donor. Because organic materials generally do not form periodic lattices which result in the formation of energy bands,[13;16] the nature and terminology of their energetic states are different than for inorganic semiconductors. In place of the valance band there is the highest occupied molecular orbital (HOMO), while the lowest unoccupied molecular orbital (LUMO) is analogous to the conduction band. In an electron acceptor-donor pair, the electron acceptor has a lower energy HOMO and LUMO than the electron donor, as shown in Figure 1.6. When an exciton is near this interface the electron will want to occupy the low energy LUMO of the acceptor while the hole will want to occupy the high energy HOMO of the donor. This can result in the exciton dissociating into separate charges.

This ability to separate charges at an interface is used in organic solar cells as

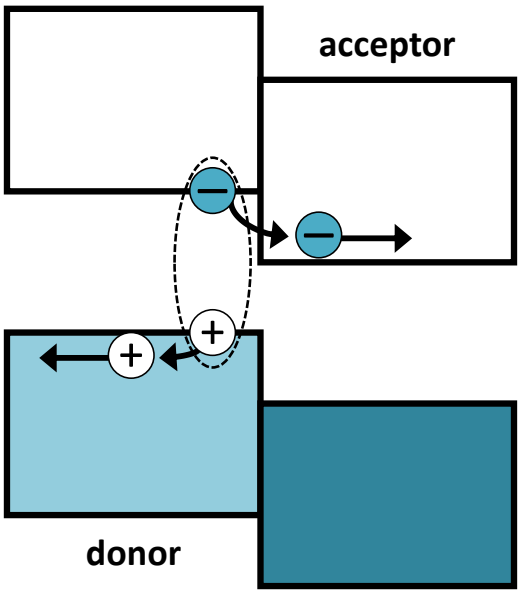

Figure 1.6: Charge separation across a donor-acceptor interface. HOMOs are in teal while LUMOs are in white. The exciton is depicted by the dashed oval.

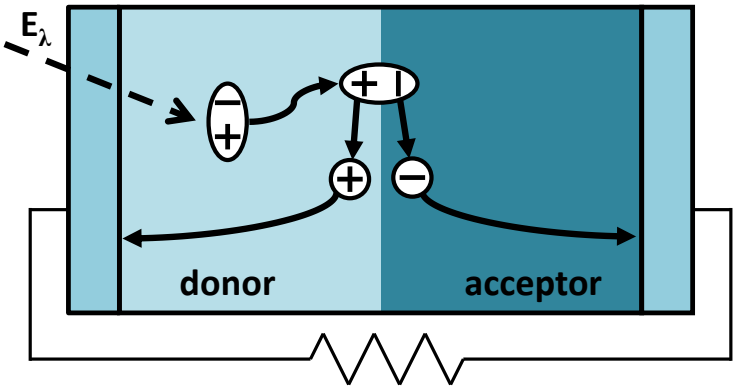

Figure 1.7: Schematic of a conventional silicon solar cell showing light (dashed line) being absorbed by the cell creating an exciton which diffuses to the interface where charge separation occurs. Charges are collected at electrodes to drive an external load.

depicted in Figure 1.7. Light is absorbed by the device creating an exciton which needs to diffuse to the donor-acceptor interface where charge separation can occur. After the charges separate they can diffuse to the electrodes where they are collected to drive an external circuit.

Comparing this type of organic cell to a silicon cell (Figure 1.3) the main difference is the presence of the exciton. Because the electron and hole in an exciton are bound in close proximity to each other, they can recombine quickly compared to the free charges in a silicon solar cell. Exciton diffusion to the interface must compete with this recombination. In most organic materials, excitons diffuse less than 20 nm before they recombine[17;18;19], whereas 100-200 nm of material are required to absorb the majority of incident sunlight[20]. This means that, on average, only excitons created in 10-20% of the device contribute to power generation which limits the overall efficiency. Referring back to the sources of loss depicted in Figure 1.5, in addition to limitations on absorption and energy lost to heat, organic PVs have increased recombination compared to silicon PVs. In order to overcome this limitation devices with different architectures have been proposed,[21;22] yet the underlying physics of the exciton are not well understood. Further knowledge of exciton dynamics would improve device efficiency by guiding research of new materials and architectures.

1.3 Photophysics of Excitons

This section focuses on the formation, transport, and decay of excitons. This will give the opportunity to discuss a variety of topics including absorption, diffusion, energy transfer, fluorescence, internal conversion, and intersystem crossing.

1.3.1 Exciton Formation

Light incident on a material can be absorbed exciting an electron from the ground state to an excited state. The electron can then be bound to its associated hole creating an exciton. The probability to absorb light of a given frequency depends on the electronic structure of the material. The energy surface for the ground (S_0) and first excited (S_1) states can be modeled as harmonic oscillations of some normal coordinate (often a bond stretching) giving different vibrational levels (0, 1, 2, etc.) separated by the energy of the oscillation (ω_0) as depicted in Figure 1.8.[23] The equilibrium position of the normal coordinate can be different for the ground and excited states resulting in the harmonic wells being displaced by an amount, Δ. For many vibrational frequencies, electrons in S_0 predominantly occupy the ν=0 vibrational level at room temperature due to the high energy of oscillations when compared to the thermal energy kT where k is the Boltzmann constant. For example, at room temperature kT = 0.026 eV while $\omega_0 \approx$ 1600 cm^{-1} = 0.18 eV for a C=C stretch.[24] If this is the case, absorption occurs from the ν=0 vibrational level of S_0 to different vibrational levels of S_1.

The absorption probability of each vibrational transition (0-0, 0-1, 0-2, etc.) is

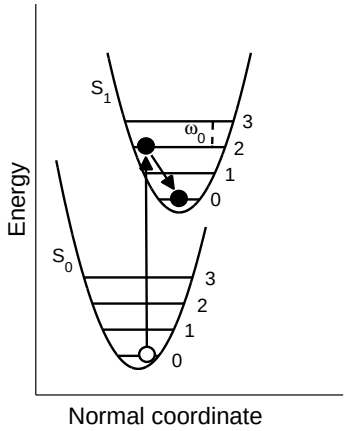

Figure 1.8: Schematic of absorption from the ν=0 vibrational level of the ground state (S_0) to the ν=2 vibrational level of the first excited state (S_1). The excited electron typically decays to the ν=0 vibrational level of S_1.

proportional to the square of the transition moment integral, M:

$$M = \int \psi'^{*}\, \hat{\mu}\, \psi \, \mathrm{d}\tau \tag{1.1}$$

where ψ is the initial wavefunction, ψ' is the final wavefunction, and $\hat{\mu}$ is the dipole operator.[24] The Born-Oppenheimer approximation allows for the wavefunctions to be separated into vibrational (ψ_v), electronic (ψ_e), and spin (ψ_s) components, while the dipole operator can be written as the sum of a component that depends on nuclear coordinates ($\hat{\mu}_v$) and a component that depends on electron coordinates ($\hat{\mu}_e$). Splitting the integrals and noting that $\int \psi_e'^{*}\, \psi_e \, \mathrm{d}\tau = 0$ due to the orthogonality of the electronic

wavefunctions, Equation 1.1 can be written:

$$M = \int \psi_v'^{*}\, \psi_v \, \mathrm{d}\tau_n \int \psi_e'^{*}\, \hat{\mu}_e \, \psi_e \, \mathrm{d}\tau_e \int \psi_s'^{*}\, \psi_s \, \mathrm{d}\tau_s. \tag{1.2}$$

The second and third integrals in Equation 1.2 form the basis of orbital and spin selection rules, respectively. If one of these integrals is zero, the transition is "forbidden" and, generally, has a low probability of occurring. For a given electronic transition, the square of the first integral gives the relative strength of the different vibrational transitions and is called the Franck-Condon factor. It should be noted that because S_0 and S_1 are displaced along the normal coordinate, the vibrational wavefunctions are not necessarily orthogonal, and none of the vibrational integrals can, a priori, be set to zero.

Evaluation of Franck-Condon factors involves integrals of Hermite polynomials[25] which can be carried out numerically or, under certain approximations, simplified to a closed form[26]. Example Maple code to calculate Franck-Condon factors is shown in Appendix A.1. Each Franck-Condon factor corresponds to a vibrational transition with a specific energy and the absorption of light at the associated wavelength or frequency as determined by

$$E = h\nu = \hbar\omega = \frac{hc}{\lambda} \tag{1.3}$$

where h ($\hbar$) is the (reduced) Planck constant and ν, ω, and λ are the frequency, angular frequency, and wavelength of the light, respectively.[27] To simulate an absorption

spectrum the Franck-Condon factors can be multiplied by a Lorentzian or Gaussian broadening function representing homogeneous or inhomogeneous broadening, respectively.[28] Figure 1.9 shows simulated absorption spectra for different values of Δ. If Δ is zero, excitation from S_0 to S_1 does not perturb the vibration, and the vibrational wavefunctions are orthonormal. Thus, only 0-0 absorption is observed. As Δ increases the vibrations are perturbed and the orthonormality is broken. Absorption to other vibrational states becomes possible and a vibrational progression is observed. Note that the broadening of each peak was kept small in this example to accentuate the vibrational progression; in some systems the broadening may obscure the vibrational progression.

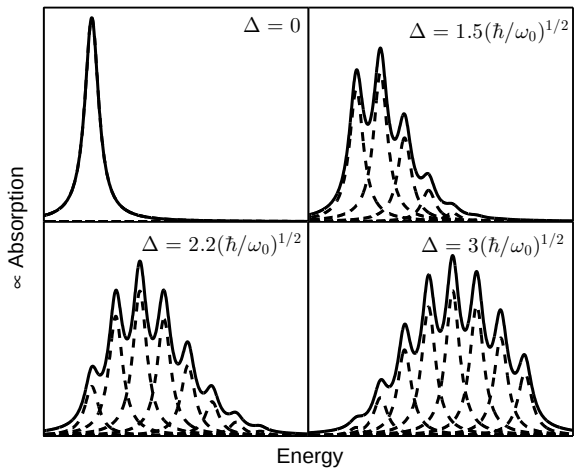

Figure 1.9: A series of simulated absorption spectra for different values of displacement, Δ. Dashed lines represent absorption to a specific vibrational state (0-0, 0-1, 0-2, etc. in order of increasing energy). The sums of these individual absorptions are represented with solid lines.

1.3.2 Exciton Transport

Understanding exciton transport in solar cell materials is very important as the exciton needs to reach an interface in order to dissociate into usable charges. This section will look at exciton diffusion as well as Förster and Dexter energy transfer.

Diffusion

Diffusion can be expressed in two different, but mathematically consistent ways. First, diffusion can be thought of as a random walk. Imagine an exciton on a line and it randomly steps a distance l left $(-l)$ or right $(+l)$ every time interval Δt. The goal is to calculate the most probable position of the exciton after some time t, usually the lifetime of the exciton. The expectation value of displacement for any given step is

$$\langle d_i \rangle = \sum_i p_i x_i = 0.5(+l) + (0.5)(-l) = 0 \tag{1.4}$$

where the sum is over all possible steps, p_i is the probability of step i, and x_i is the displacement of step i. Because there is an equal probability of stepping positive or negative the expectation value is zero. After time t there will have been a total of $n = t/\Delta t$ steps and the expected displacement will be

$$\langle d \rangle = \left\langle \sum_{i=1}^{n} d_i \right\rangle = \sum_{i=1}^{n} \langle d_i \rangle = \sum_{i=1}^{n} 0 = 0 \tag{1.5}$$

meaning the average displacement is zero. To get an idea of how far the excitons are

moving, instead of looking at $\langle d \rangle$, $\langle d^2 \rangle$ can be calculated:

$$\begin{aligned} \langle d^2 \rangle &= \left\langle \left[\sum_i d_i \right]^2 \right\rangle = \left\langle \sum_i d_i^2 + \sum_{i \neq j} d_i d_j \right\rangle = \sum_i \langle d_i^2 \rangle + \sum_{i \neq j} \langle d_i d_j \rangle = nl^2 \\ \langle d_i^2 \rangle &= 0.5(+l)^2 + 0.5(-l)^2 = l^2 \\ \langle d_i d_j \rangle &= 0.25(+l)(+l) + 0.25(+l)(-l) + 0.25(-l)(+l) + 0.25(-l)(-l) = 0 \end{aligned} \tag{1.6}$$

giving a root mean square distance after time t of

$$d_{rms} = \sqrt{\langle d^2 \rangle} = \sqrt{nl^2} = \sqrt{l^2 \frac{t}{\Delta t}}. \tag{1.7}$$

The above discussion was for a random walk along a line, but Equation 1.7 is correct for a random walk in three dimensions as well. This can be confirmed mathematically [29], but can also be shown by simulating a three dimensional random walk a sufficiently large amount of times for a variety of step numbers. Matlab code and results for this are shown in Appendix A.2.

The second way to approach diffusion is to recast the random walk problem as a differential equation and solve. Starting with an exciton on a line, the probability of finding the exciton in position i after time step n is related to the location of the exciton after time step $n-1$. After time step $n-1$ if the exciton is located on $i-1$ or $i+1$ there is a 50% chance the exciton will move to position i during step n. Thus, the probability

of the exciton being in position i after time step n is

$$P(i,n) = \frac{1}{2}P(i-1,n-1) + \frac{1}{2}P(i+1,n-1). \tag{1.8}$$

Subtracting $P(i,n-1)$ from both sides gives

$$P(i,n) - P(i,n-1) = \frac{1}{2}\left(P(i-1,n-1) - 2P(i,n-1) + P(i+1,n-1)\right). \tag{1.9}$$

Assuming the step size, l, and the time interval between steps, Δt, are small compared to the total distance and total time, Equation 1.9 can be rewritten as derivatives using the finite difference method.[30] The left hand side looks like a first derivative with respect to time and the right hand side looks like a second derivative with respect to space:

$$\Delta t \frac{\partial P}{\partial t} = \frac{1}{2} l^2 \frac{\partial^2 P}{\partial x^2}. \tag{1.10}$$

Defining the diffusion constant

$$D_{1D} = l^2/2\Delta t \tag{1.11}$$

Equation 1.10 takes the form of the one dimensional diffusion equation

$$\frac{\partial P}{\partial t} = D_{1D} \frac{\partial^2 P}{\partial x^2}. \tag{1.12}$$

The solution to Equation 1.12 is[31]

$$P(x,t) = \frac{1}{\sqrt{4D\pi t}} e^{-\frac{x^2}{4Dt}} \tag{1.13}$$

which can be confirmed by substituting into Equation 1.12 as well as the appropriate boundary and initial conditions as shown in Appendix A.3. The expectation value of x and x^2 are:

$$\begin{aligned} \langle x \rangle &= \int_{-\infty}^{\infty} xP(x,t)\,\mathrm{d}x = 0 \\ \langle x^2 \rangle &= \int_{-\infty}^{\infty} x^2 P(x,t)\,\mathrm{d}x = 2D_{1D}t \end{aligned} \tag{1.14}$$

giving a rms displacement, often called the diffusion length $L_{D,1D}$, of

$$L_{D,1D} = \sqrt{2D_{1D}t} \tag{1.15}$$

which is consistent with Equations 1.7 and 1.11.

A similar procedure can be followed for three dimensions, but instead of a factor of 1/2 in Equation 1.9 there is a factor of 1/6 due to the increase in dimension. The results (see Appendix A.3) are

$$\begin{aligned} D_{3D} &= l^2/6\Delta t \\ \langle r \rangle &= \int_{-\infty}^{\infty} rP(r,t)\,\mathrm{d}\tau = 0 \\ \langle r^2 \rangle &= \int_{-\infty}^{\infty} r^2 P(r,t)\,\mathrm{d}\tau = 6Dt \end{aligned} \tag{1.16}$$

giving a diffusion length of

$$L_{D,3D} = \sqrt{6D_{3D}t}. \tag{1.17}$$

As a final note on diffusion, both the random walk and differential equation approach require the step size and step time to be small compared to the overall distance traveled and the lifetime of the exciton. Also, the motion of the exciton must remain constant throughout its lifetime, t. If there are many hops with a characteristic diffusion constant, D, that does not change with time, the physics of each individual hop can be neglected, and the equations in this section are valid. This is often not the case, especially when considering exciton trapping, inhomogeneous samples, or ultrafast dynamics. The following sections will discuss energy transfer mechanisms which can be used to more accurately model exciton transport.

Energy Transfer

Energy transfer can occur between one initially excited chromophore, called the donor, and another chromophore called the acceptor. In the following discussion it is assumed the initial state consists of the donor in the first excited state and the acceptor in the ground state, while the final state consists of the donor in the ground state and the acceptor in the first excited state. Energy transfer can also occur between two initially excited states. One example of this is exciton-exciton annihilation which will be discussed in Chapter 5. For the current discussion the initial and final wavefunctions

may be inappropriately written

$$\begin{aligned} \widetilde{\Psi}_I &= \psi'_D(\mathbf{r_1})\psi_A(\mathbf{r_2}) \\ \widetilde{\Psi}_F &= \psi_D(\mathbf{r_1})\psi'_A(\mathbf{r_2}) \end{aligned} \tag{1.18}$$

where the D (A) subscript refers to the donor (acceptor) and the prime denotes an excited state wavefunction. The position of the electron in the donor is labeled $\mathbf{r_1}$ whereas the position of the electron in the acceptor is labeled $\mathbf{r_2}$. These wavefunctions are incorrect because of this labeling. It is impossible to label the electrons or tell which one is on the acceptor or the donor. Because of this, the wavefunctions should be written as linear combinations of the two possibilities:

$$\begin{aligned} \Psi_I &= \frac{1}{\sqrt{2}}\left[\psi'_{D,1}\psi_{A,2} - \psi'_{D,2}\psi_{A,1}\right] \\ \Psi_F &= \frac{1}{\sqrt{2}}\left[\psi_{D,1}\psi'_{A,2} - \psi_{D,2}\psi'_{A,1}\right] \end{aligned} \tag{1.19}$$

where the explicit dependence on $\mathbf{r_1}$ and $\mathbf{r_2}$ has been replaced with a subscript. Because electrons are fermions the linear combination is the difference of the two terms.[16] To determine the probability of transition from Ψ_I to Ψ_F Fermi's golden rule can be employed:

$$P_{DA} = \frac{2\pi}{\hbar}\left|\langle\Psi_F|\, H_1\, |\Psi_I\rangle\right|^2 \rho_f(E_f = E_i) \tag{1.20}$$

where H_1 is the Hamiltonian representing the Coulombic donor-acceptor interaction

and $\rho_f(E_f = E_i)$ is the density of final states that have the same energy as the initial state.[32] The braket in Equation 1.20 can be expanded and simplified to[33]

$$\langle H_1 \rangle = \underbrace{\langle \psi_{D,1}\psi'_{A,2}| \, H_1 \, |\psi'_{D,1}\psi_{A,2}\rangle}_{\text{Coulombic, Förster}} - \underbrace{\langle \psi_{D,1}\psi'_{A,2}| \, H_1 \, |\psi'_{D,2}\psi_{A,1}\rangle}_{\text{Exchange, Dexter}} . \tag{1.21}$$

The first term has no exchange of electrons and represents the Coulombic interaction between the donor and acceptor. If dipole-dipole interactions dominate this term leads to Förster resonance energy transfer. The second term accounts for the possibility of electron exchange between the donor and acceptor and gives Dexter energy transfer.

Förster Energy Transfer

Förster resonance energy transfer (FRET) is the result of the dipole-dipole coupling between a donor and acceptor.[34;35;36;37] The initially excited donor decays transferring its energy to the acceptor as depicted in Figure 1.10. Simplifying the first integral in Equation 1.21 the rate constant for this process is found to be

$$k_F = \frac{1}{\tau}\left(\frac{R_F}{r}\right)^6 \tag{1.22}$$

where τ is the lifetime of the donor, R_F is the Förster radius, and r is the distance between the donor and the acceptor.[37] The Förster radius is defined such that when $r = R_F$, FRET from the donor to the acceptor and natural deactivation of the donor are equally probable. Thus, two chromophores that have identical Förster transfer

properties, but different excited state lifetimes will have different Förster radii. The Förster radius can be written

$$R_F^6 = \frac{9\phi_D ln(10)\kappa^2}{128\pi^5 n^4 N_A} \int_0^\infty f_D(\lambda)\epsilon_A(\lambda)\lambda^4 \, \mathrm{d}\lambda \tag{1.23}$$

where ϕ_D is the fluorescence quantum yield of the donor, κ^2 is an orientation factor which equals 2/3 for an isotropic distribution of dipoles, n is the index of refraction of the solvent or medium between the donor and acceptor, N_A is Avagadro's number, f_D is the fluorescence spectrum of the donor normalized to have unit area, and ϵ_A is the molar extinction coefficient of the acceptor.[37] Förster's original derivation of equations 1.22 and 1.23 is in German, but it has been translated to English in *Biological Physics* edited by Mielczarek.[38] The derivation is also carried out by Agranovich and Maradudin.[39]

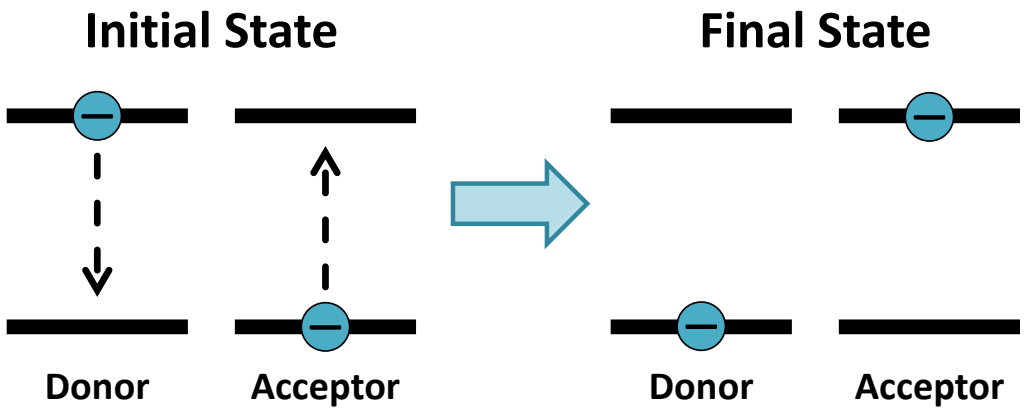

Figure 1.10: Schematic for Förster energy transfer. Initially an exciton is on the donor. The exciton on the donor decays to the ground state transferring its energy to the acceptor. The final state is the exciton on the acceptor.

Equation 1.23 shows that the Förster radius and, therefore, the Förster rate constant depend on the fluorescence quantum yield of the donor and the spectral overlap of the donor fluorescence and the acceptor absorption. Because of this, FRET can be compared to reabsorption where the donor emits a photon and the acceptor absorbs it. Care should be taken when making this comparison as no photon is present in FRET. Sometimes this lack of a photon is called a virtual photon which can cause its own confusion. FRET is a purely dipole-dipole interaction where resonance between oscillations in the donor and acceptor can cause direct energy transfer.

FRET is usually long-range when compared to other energy transfer mechanisms. Förster radii are typically 1-10 nm allowing excitons to transfer between molecules. If excitons transfer many times during their lifetimes, this type of motion can lead to diffusion. Taking the hopping time to be the inverse of the rate constant (Equation 1.22) and the step size to be the intermolecular distance, d, the three dimensional diffusion constant (Equation 1.16) and diffusion length (Equation 1.17) can be written

$$\begin{aligned} D_F &= \frac{R_F^6}{6\tau d^4} \\ L_{D,F} &= \sqrt{\frac{R_F^6}{d^4}}. \end{aligned} \tag{1.24}$$

Dexter Energy Transfer

In contrast to FRET, Dexter energy transfer involves the physical exchange of electrons between the donor and acceptor as depicted in Figure 1.11.[33;34] Solving the second

integral in Equation 1.21 the Dexter rate constant can be written

$$k_D = \frac{2\pi}{\hbar} K^2 e^{-2r/L} \int f_D(E) F_A(E)\, \mathrm{d}E \equiv \kappa e^{-2r/L} \tag{1.25}$$

where K is a constant with units of energy, r is the distance between the donor and acceptor, L can be thought of as an average effective Bohr radius of the excited donor and the unexcited acceptor, f_D is the donor emission spectra, and F_A is the acceptor absorption spectra.[33] Both the emission and absorption spectra are normalized so that integrating over photon energy gives unity. Note, this is a different normalization scheme than for FRET. Collecting all the constants into κ gives the simplified final equality.

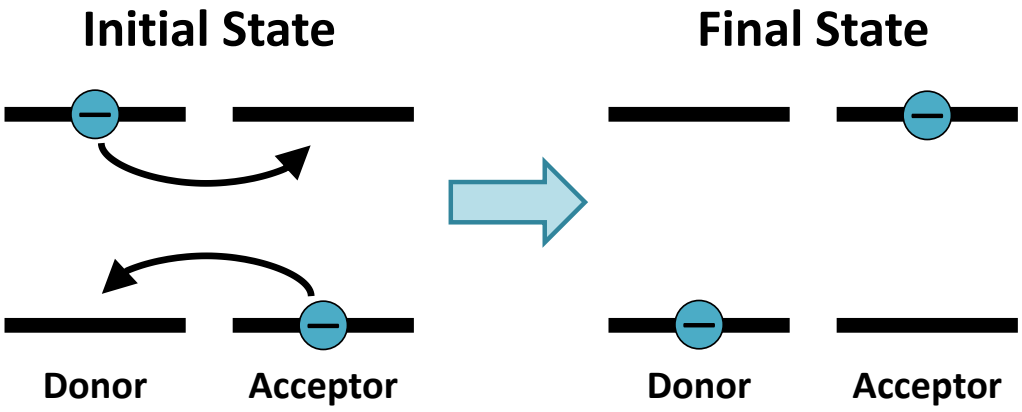

Figure 1.11: Schematic for Dexter energy transfer. Initially an exciton is on the donor. The electrons in the donor and the acceptor are exchanged. The final state is an exciton on the acceptor.

Dexter transfer occurs by the exchange of electrons, so the wavefunctions of the donor and acceptor must overlap to achieve transfer. Dexter transfer usually only occurs with

nearest neighbors over short distances (1-2 nm). In general, at longer distances FRET is the most probable energy transfer mechanism, while at shorter distances Dexter transfer dominates as shown in Figure 1.12.[40] Similar to the treatment of FRET above, the Dexter transfer rate can be used to estimate the corresponding diffusion constant and diffusion length assuming many hops occur over the excited state lifetime:

$$\begin{aligned} D_D &= \frac{d^2 \kappa e^{-2d/L}}{6} \\ L_{D,D} &= \sqrt{d^2 \tau \kappa e^{-2d/L}}. \end{aligned} \tag{1.26}$$

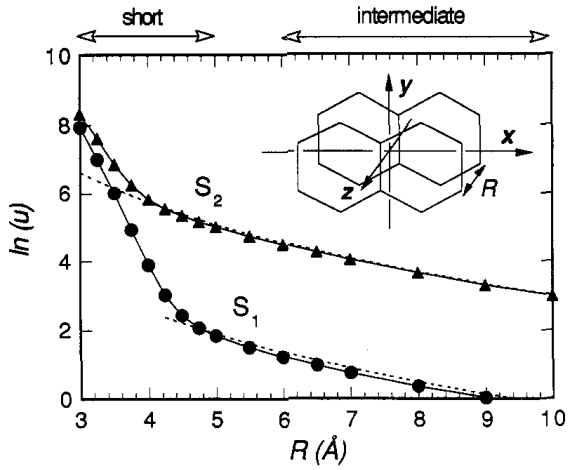

Figure 1.12: Calculated electronic coupling (solid lines) in naphthalene as a function of interchromophore separation. Dashed lines show dipole-dipole (FRET) coupling. At longer separations coupling matches FRET result, while at shorter separations coupling follows Dexter result. Figure reproduced with permission from Scholes and Ghiggino.[40] Copyright 1994 American Chemical Society.

1.3.3 Exciton Decay

The previous section dealt with exciton transport. In determining how far an exciton can move, two phenomena are important. The first deals with how easily the exciton moves through the sample which is determined by, for example, the diffusion constant, the Förster radius, and the average effective Bohr radius. The second factor is how long the exciton lives. If an exciton is very mobile but lives for a short amount of time it won't travel very far. Conversely, if an exciton moves slowly but lives for a long time it may be able to move sizable distances. This section will focus on understanding the different relaxation pathways that lead to exciton decay.[23]

During light absorption a molecule is excited from the ground state, S_0, to an excited vibrational state of S_1 as depicted in Figure 1.13. After excitation the excited state will quickly undergo vibrational relaxation to the bottom of S_1. Often, vibrational relaxation is very fast so that decay of the excited state predominantly occurs from the lowest vibrational level; this is called Kasha's rule.[41] From the lowest vibrational level of S_1 the excited state can decay back to the ground state through nonradiative and radiative pathways. A nonradiative decay process between states that have the same spin multiplicity, such as $S_1 \rightarrow S_0$, is called internal conversion, while radiative decay between states of the same spin multiplicity is called fluorescence.

Just as absorption gives rise to a vibrational progression due to transitions to different vibrational levels of S_1, fluorescence gives a vibrational progression due to transitions to different vibrational levels of S_0 as depicted in Figure 1.14. Equation 1.2

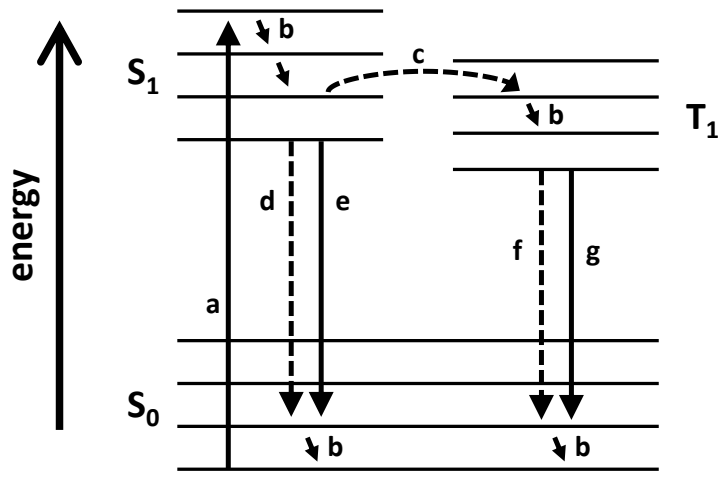

Figure 1.13: Schematic for different exciton decay pathways after excitation (a): b – vibronic relaxation ($S_1 \rightarrow S_1$, $T_1 \rightarrow T_1$ or $S_0 \rightarrow S_0$), c – intersystem crossing (nonradiative $S_1 \rightarrow T_1$), d – internal conversion (nonradiative $S_1 \rightarrow S_0$), e – fluorescence (radiative $S_1 \rightarrow S_0$), f – intersystem crossing (nonradiative $T_1 \rightarrow S_0$), g – phosphorescence (radiative $T_1 \rightarrow S_0$).

was used to determine the probability of absorption, but can also be used to determine the probability of emission. This allows for the simulation of fluorescence spectra using Franck-Condon factors, just as absorption spectra were simulated in Figure 1.9. Franck-Condon fitting for emission from an amorphous P3HT film is presented in Figure 1.14 showing emission from individual vibronic transitions summing to match the total fluorescence spectrum.

If vibrational levels of S_1 overlap in energy with vibrational levels of the first excited triplet state, T_1, a nonradiative transition can occur between the states. Nonradiative transitions between states of different spin multiplicities are called intersystem crossing.

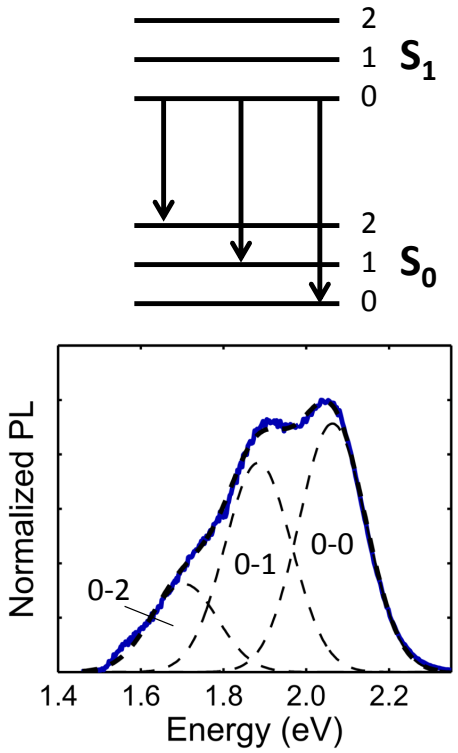

Figure 1.14: Top: Schematic of fluorescence showing emission from the 0th vibrational level of S_1 to different vibrational levels of S_0. Bottom: Franck-Condon fit to emission from an amorphous P3HT film. Blue line is fluorescence data, thick dashed line is the overall fit (overlaps with data), and thin dashed lines are emission for individual vibronic transitions as labeled.

After transitioning to the triplet manifold, the excited state will quickly relax to the lowest vibrational level of T_1. From this state it can nonradiatively or radiatively decay to S_0. The nonradiative pathway is another instance of intersystem crossing, while the radiative pathway gives phosphorescence.

The timescales of these different decay pathways can vary by upto 10 orders of magnitude as shown in Table 1.1. Because intersystem crossing and phosphorescence require

a spin flip they are generally much slower than internal conversion and fluorescence. Relaxation can occur on ps (10^{-12} s) and fs (10^{-15} s) time scales which is much faster than the ∼1 ns (10^{-9} s) electronic response of detectors such as photodiodes and photomultiplier tubes. This makes direct observation of internal conversion, for example, difficult if not impossible.

Table 1.1: Time scales of different excited state decay pathways.[23]

Process	Transition	Radiative?	Change in spin?	Time scale
Vibrational relaxation	—	No	No	10^{-14} s
Internal conversion	$S_1 \rightarrow S_0$	No	No	$10^{-12} - 10^{-7}$ s
Fluorescence	$S_1 \rightarrow S_0$	Yes	No	10^{-9} s
Intersystem crossing	$S_1 \rightarrow T_1$	No	Yes	$10^{-12} - 10^{-6}$ s
Phosphorescence	$T_1 \rightarrow S_0$	Yes	Yes	$10^{-7} - 10^{-5}$ s
Intersystem crossing	$T_1 \rightarrow S_0$	No	Yes	$10^{-8} - 10^{-3}$ s

For the case of a molecule which undergoes only internal conversion and fluorescence, the decay rates can be calculated using a combination of fluorescence quantum yield and fluorescence lifetime measurements. The mechanism for this decay can be written:

$$\begin{aligned} S_1 &\xrightarrow{k_{nr}} S_0 \\ S_1 &\xrightarrow{k_r} S_0 \end{aligned} \tag{1.27}$$

where k_{nr} is the non-radiative decay rate of internal conversion and k_r is the radiative decay rate of fluorescence. This is analogous to a parallel kinetic reaction.[42] The

differential equation for this system is then

$$\begin{aligned} -\frac{d\left[S_1\right]}{dt} &= k_{nr}\left[S_1\right] + k_r\left[S_1\right] \\ &= \left(k_{nr} + k_r\right)\left[S_1\right] \\ &= k_T\left[S_1\right] \end{aligned} \tag{1.28}$$

where $k_T = k_{nr} + k_r$ is the sum of the decay rates. The solution to Equation 1.28 gives the number of excited states as a function of time. The amount of fluorescence observed is proportional to the number of excited states, so the solution to Equation 1.28 also gives the functional form of fluorescence decay:

$$\text{fluorescence} \propto e^{-k_T t}. \tag{1.29}$$

Thus, conducting a fluorescence lifetime experiment, such as time correlated single photon counting (Chapter 2), gives the total rate, k_T. In order to determine the individual rates, the fluorescence quantum yield, ϕ, can be found by comparing the emission of the sample to that of a known standard (Chapter 2). The fluorescence quantum yield can be written in terms of the decay rates as[43]

$$\phi = \frac{k_r}{k_T}. \tag{1.30}$$

Thus, if ϕ and k_T are measured, k_{nr} and k_r can be calculated.

The prescription above to calculate decay rates only works for fluorescent molecules with measurable lifetimes. Furthermore, any energy transfer or intersystem crossing

can not be observed. If there are multiple non-radiative decay pathways, they would all contribute to k_{nr}, but further analysis of k_{nr} is not possible. One way to overcome these limitations is to use ultrafast spectroscopy which will be discussed in the next section.

1.4 Pump-Probe Spectroscopy

This section will discuss the physics of pump-probe spectroscopy and the different phenomena that contribute to pump-probe signals. The laser system and pump-probe apparatus used for the work presented in this thesis are discussed in Chapter 2.

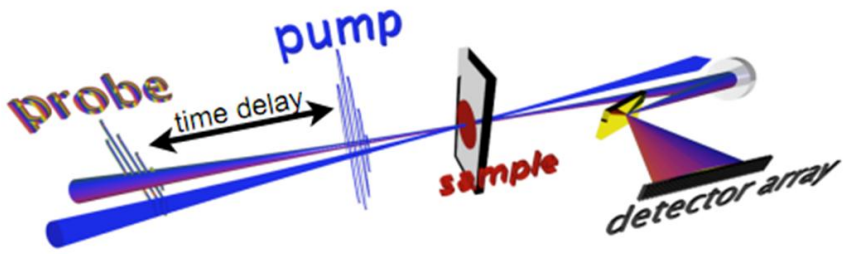

Figure 1.15: Schematic of pump-probe spectroscopy.

Pump-probe spectroscopy, which is sometimes referred to as transient absorption spectroscopy, is one technique that can be used to study excited state dynamics. A schematic of pump-probe spectroscopy is shown in Figure 1.15. Two ultrafast laser pulses are incident on the sample with a controllable time delay between them. The first pulse is the pump pulse which is absorbed by the sample creating excited states. The second pulse probes the sample and can be influenced by the presence of the excited

states created by the pump. The pump is chopped at half the laser repetition rate so that only every-other probe pulse is influenced by the pump. After passing through the sample the probe is dispersed by a grating and the intensity is measured with (I) and without (I_0) the pump pulse incident on the sample. These intensities are compared in order to calculate the change in absorption (ΔOD) induced by the pump:

$$\Delta OD = -\log_{10}\left(\frac{I}{I_0}\right). \tag{1.31}$$

Equation 1.31 is the same equation used for ground state absorption measurements. In ground state absorption experiments, the amount of light transmitted through a neat solvent is measured (I_0). A solute is then added to the solvent and the amount of transmitted light is measured again (I). Equation 1.31 is then used to calculate the change in absorption caused by adding the solute. Because the neat solvent is thought of as a baseline, ground state absorption signal is referred to as an optical density (OD) not a ΔOD. In pump-probe spectroscopy the same type of measurement is made, but instead of adding solute, excited states are 'added' and the induced change in absorption, ΔOD, is measured.

There are three main sources that contribute to pump-probe spectra as depicted in Figure 1.16. First, excited states created by the pump can absorb probe light. This results in more probe light being absorbed compared to the reference probe pulse giving a positive ΔOD. Second, depopulation of the ground state by the pump pulse causes there to be less ground state absorption of the probe pulse when compared to the

reference probe pulse. Because there is less absorption this appears as a negative ΔOD feature. Finally, the probe pulse can stimulate excited states created by the pump to radiatively decay. This causes more light to be transmitted in comparison to the reference pulse and gives a negative ΔOD signal.

Measured pump-probe spectra are the summation of all the signals presented in Figure 1.16 which makes proper analysis difficult and very important. A simulated pump-probe spectrum is shown in Figure 1.17 illustrating that three simple gaussian shapes can give a complicated overall spectrum. Because ground state holes come about due to loss of ground state absorption, the spectral shape of a ground state hole matches the ground state absorption spectrum of the excited chromophore. Similarly, stimulated emission often overlaps with the steady state fluorescence spectrum. At early delay times the excited state may not have cooled to the lowest vibrational level, so stimulated emission may appear blueshifted in comparison to the steady state fluorescence. As the delay time increases the stimulated emission often redshifts to better match the steady state fluorescence (the steady state fluorescence is actually the integral of all stimulated emission). Similar shifts can occur in excited state absorption as excited states cool. These types of shifts are an example of spectral diffusion. Using steady state measurements is important when attempting to assign features or deconvolute spectra from pump-probe experiments.

Finally, the timing between the pump and probe pulses can be adjusted so that ΔOD spectra for different pump-probe delays can be collected. In the simplest case,

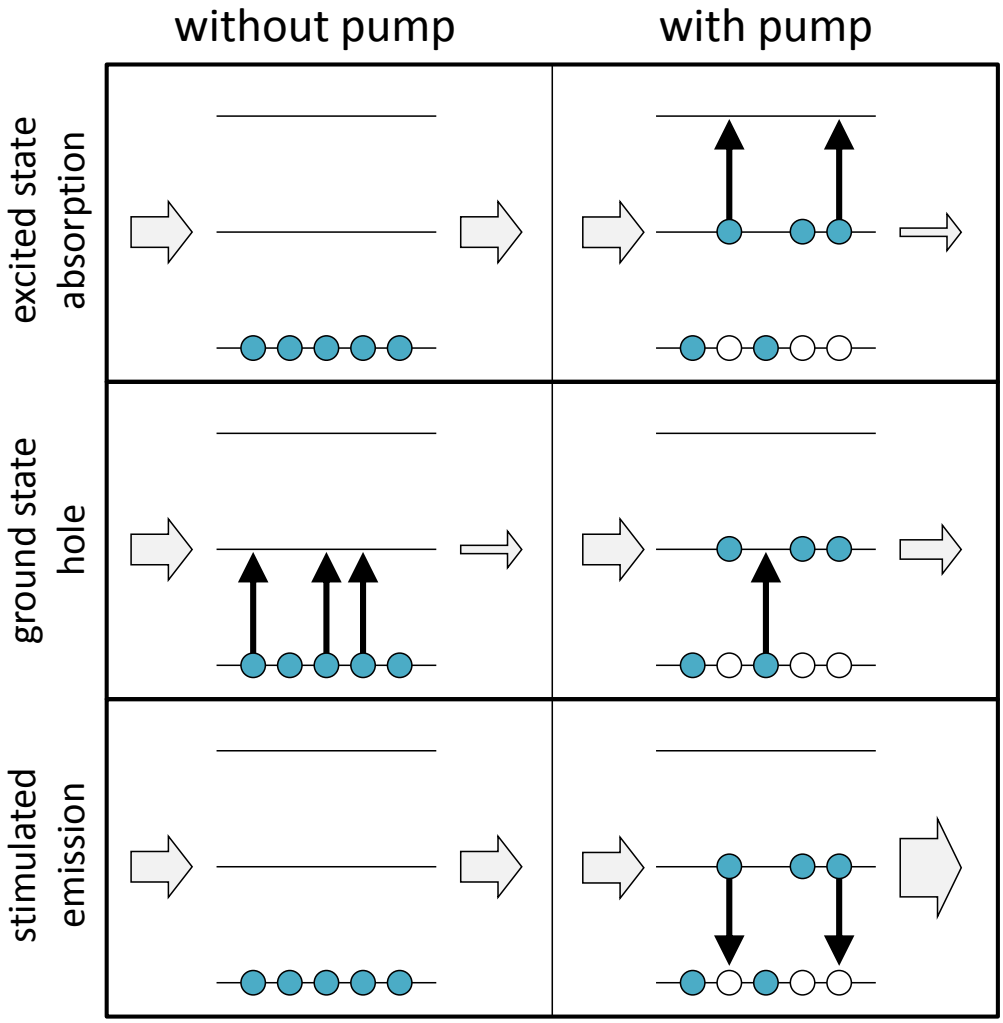

Figure 1.16: Sources of signal in pump-probe spectroscopy. Top: Excited state absorption. Before pump, photons not absorbed. After pump, excited states absorb photons. Less photons transmitted with pump, positive ΔOD. Middle: Ground state hole. Before pump, ground state electrons absorb photons. After pump, less electrons in ground state so less photons absorbed. More photons transmitted with pump, negative ΔOD. Bottom: Stimulated emission. Before pump, no excited states so no stimulated emission. After pump, incident photons stimulate excited states to radiatively decay. More photons transmitted with pump, negative ΔOD.

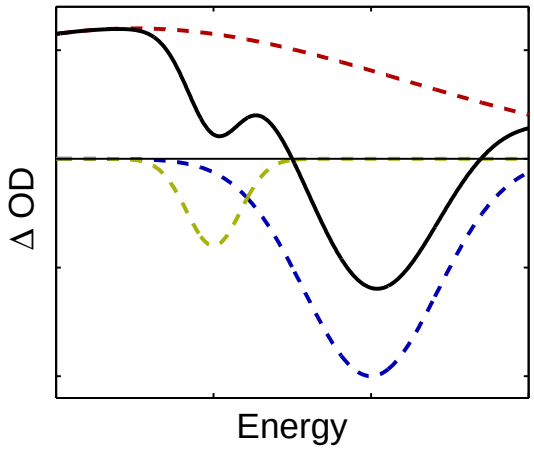

Figure 1.17: Simulated pump-probe spectrum showing different sources of signal. Individual sources are depicted as dashed lines (blue: ground state hole, yellow: stimulated emission, red: excited state absorption), while the total spectrum is shown as a solid black line. Only the solid black line is obtained from experiment.

this allows for the concentration of excited states to be measured as a function of time. At early times the pump will have created many excited states providing high amplitude signals. As time goes on, these excited states will decay resulting in lower amplitudes. A kinetic model can then be proposed and decay rates can be found by fitting the data. In more complex cases energy transfer, intersystem crossing, and charge separation events can cause spectra to change shape as a function of pump-probe delay time. In these cases more complicated analysis is required to correctly model the system.

Chapter 2

Instrumentation

In Chapter 1 the principles of absorption, fluorescence, and pump-probe spectroscopy were discussed in the context of exciton formation and decay. In the current chapter the instrumentation and methods of performing these experiments will be discussed.

2.1 Absorption Spectroscopy

Absorption spectra presented in this thesis were collected using an OLIS Cary 14 double beam spectrophotometer. Light from a tungsten (visible/infrared) or deuterium (ultraviolet) lamp passes through a monochromator to select a specific wavelength of light. The light is incident on a rotating disk which has reflective and transmissive segments. When the light is incident on a reflective segment of the disk it is directed to the sample chamber, and when light is incident on a transmissive segment it is directed to the reference chamber. After passing through the sample or reference chamber the intensity

of the light is measured using a photomultiplier tube (PMT) for ultraviolet/visible light or a PbS detector for infrared light. Optical densities are calculated by the software using the following equation:

$$OD = -\log_{10}\left(\frac{I}{I_0}\right) \tag{2.1}$$

where I is the intensity of the beam after passing through the sample chamber and I_0 is the intensity of the beam after passing through the reference chamber. Wavelength calibration is confirmed by measuring the absorption of a holmium oxide glass standard.[44]

In order to collect accurate spectra, both a baseline and sample OD are collected. First, a bare substrate (solid state samples) or a cuvette with solvent (solution samples) is placed in the sample chamber while the reference chamber is left empty. A baseline absorption spectrum is collected:

$$OD_{bl} = -\log_{10}\left(\frac{I_{bl}}{I_0}\right) \tag{2.2}$$

where I_{bl} is the intensity transmitted through the substrate or cuvette. The sample is then placed in the sample chamber (using the same substrate or cuvette if possible) and another absorption spectrum is collected:

$$OD_{bl+s} = -\log_{10}\left(\frac{I_{bl+s}}{I_0}\right) \tag{2.3}$$

where I_{bl+s} is the intensity transmitted through the sample and the substrate or cuvette. Taking the difference of Equations 2.3 and 2.2 gives the optical density of the sample:

$$\begin{aligned} OD_s = OD_{bl+s} - OD_{bl} &= -\log_{10}\left(\frac{I_{bl+s}}{I_0}\right) + \log_{10}\left(\frac{I_{bl}}{I_0}\right) \\ &= -\log_{10}\left(\frac{I_{bl+s}}{I_{bl}}\right). \end{aligned} \tag{2.4}$$

Example baseline, sample, and corrected absorption spectra are shown in Figure 2.1 for the laser dye DCM in methanol. Note that data has been converted from nm to eV. Because the data is a ratio of measured intensities, any correction to the intensities due to the conversion cancel out, so only the x-axis is adjusted using Equation 1.3.

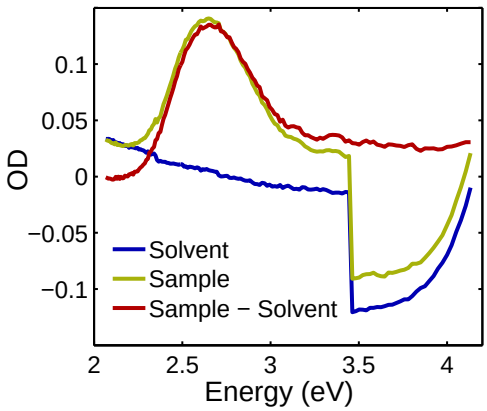

Figure 2.1: Absorption spectrum of the laser dye DCM showing background subtraction. Blue line shows collected absorption spectrum of the solvent (methanol), yellow line shows collected absorption spectrum after the addition of DCM, and red line shows the difference of the two spectra, giving the absorption spectrum of DCM.

2.2 Fluorescence Spectroscopy

Fluorescence spectra were collected using a SPEX Fluorolog 1680. Light from a xenon lamp is directed through a double monochromator to select the excitation wavelength. The light is directed at the sample and the fluorescence of the sample is collected at a right-angle to the excitation light (dilute solutions) or in a front-face geometry (solid state samples). The fluorescence is directed through a double monochromator and detected using a PMT. The transmission wavelength of the second monochromator is scanned while the response of the PMT is measured giving a fluorescence spectrum.

Because the PMT response and the monochromator grating efficiency are wavelength dependent, the collected fluorescence spectrum needs to be corrected. A correction curve was found by collecting the emission spectra of quinine sulfate, coumarin 153, DCM, and LDS 751 (Figure 2.2 inset, dashed lines) and comparing to the emission spectra reported in the literature (Figure 2.2 inset, solid lines).[45;46] A correction curve was generated such that the collected spectra best matched the reported spectra (Figure 2.2, black line). Every subsequent spectrum collected is corrected using this curve.

While corrected spectra are proportional to the emission of the sample, they are not on an absolute scale. Only a portion of the emission is collected and measured by the PMT, so the fluorescence quantum yield (QY) cannot be immediately calculated. To determine the QY, the fluorescence of a standard with a known QY, ϕ_S, is also

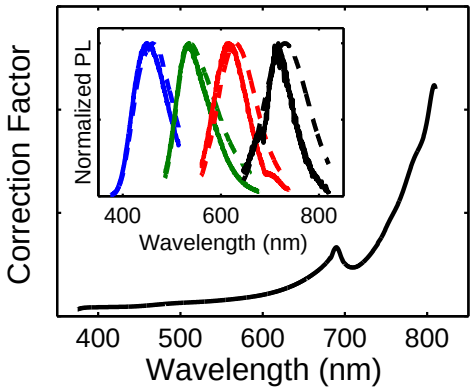

Figure 2.2: Fluorescence wavelength calibration curve for a SPEX Fluorolog 1680. Inset: Measured (solid) and reported (dashed) fluorescence of quinine sulfate (blue), coumarin 153 (green), DCM (red), and LDS 751 (black).

measured. The QY of the sample, ϕ, is calculated using

$$\phi = \phi_S \frac{I A_S n^2}{I_S A n_S^2} \tag{2.5}$$

where I is the integrated fluorescence, A is the absorption at the fluorescence excitation wavelength, and n is the index of refraction. Variables with the subscript S refer to values of the standard.[43] The sample and standard should be excited at the same wavelength and their absorption at the excitation wavelength should be kept within 10% of each other so that the geometry of absorption and emission is similar for the sample and standard.

Finally, care should be taken when converting units of emission spectra as the band-pass of the monochromator is constant for wavelength but not for energy. For example,

if the monochromator is set to pass 2 nm, it will pass 31 meV when tuned to 400 nm and 7.8 meV when tuned to 800 nm. To account for this, the intensity at each wavelength needs to be multiplied by λ^2 when converting an emission spectra from wavelength to energy.[43] This conversion factor is called the Jacobian and can have a large effect on emission spectra.[47]

2.3 Time Correlated Single Photon Counting

Time correlated single photon counting was conducted by first exciting the sample with a 40 MHz diode laser (Driver: Picoquant PDL 800-B; Heads: Picoquant LDH series). Emission from the sample is directed through a double monochromator (Jobin-Yvon TRIAX-320) and detected using an avalanche photodiode (Picoquant MPD PDM). The wavelength of the diode laser must overlap with the absorption spectrum of the sample, while the monochromator is tuned to the sample emission. When the laser fires, a trigger is sent to a timing card (Picoquant TimeHarp200). When a photon is detected by the photodiode another trigger is sent to the timing card. The time between these triggers is recorded. This process continues creating a histogram of times between excitation (laser trigger) and emission (diode trigger).

The instrument response of the system is measured by placing a cuvette of salt in the excitation beam and tuning the monochromator to the excitation wavelength. The scatter from the salt is detected by the photodiode and the returned histogram gives the instrument response, which is typically ∼500 ps FWHM. Fits to photon counting

data are convoluted over this instrument response as shown in Figure 2.3 for the laser dye DCM. This fit consists of a single exponential decay convoluted over the measured instrument response giving a lifetime of 1.3 ns in agreement with literature values.[48]

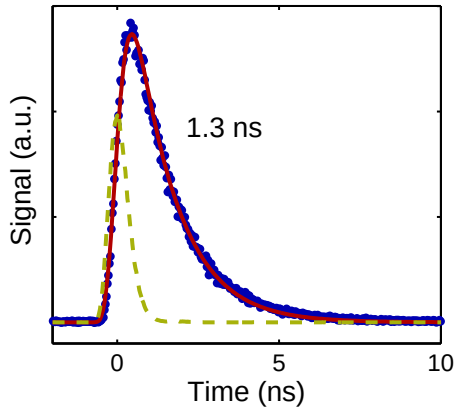

Figure 2.3: Time correlated single photon counting of the laser dye DCM in methanol. Data is shown as blue circles, the fit to the data as the red line, and the instrument response as the dashed yellow line.

For each laser trigger, only the first diode trigger will be recorded. This means that samples should be diluted (or the salt cuvette should be angled) such that the number of photons incident on the detector per laser pulse is much less than 1, hence naming the experiment single photon counting. If many photons are incident on the detector for each laser pulse, the histogram recorded will be weighted to early times giving an erroneously short excited state lifetime or instrument response.

2.4 Ultrafast Laser System

The ultrafast laser system used in this work consists of a mode-locked oscillator, a pulse stretcher, a regenerative amplifier, and a pulse compressor.[49] Each of these components and processes will be described in this section. A note on polarizations: light that is polarized horizontally, that is parallel to the laser table, is referred to as p-polarized light, whereas light that is polarized vertically, perpendicular to the laser table, is referred to as s-polarized light.

2.4.1 Mode-Locked Oscillator

The first task of the laser system is to create a train of ultrafast pulses. This is accomplished using a mode-locked oscillator. In a laser cavity of length d many standing longitudinal modes can oscillate simultaneously with wavelengths of $\lambda_m = 2d/m$ and frequencies $\omega_m = 2\pi mc/2d$ where m is a positive integers and c is the speed of light. The frequency spacing between modes is then $\Delta\omega = 2\pi c/2d$. The time-dependent complex electric field for a series of $2n+1$ modes with center frequency ω_0 can be written

$$E(t) = \sum_{l=-n}^{n} E_{0,l} \exp\left\{i\left[(w_0 + l\Delta\omega)t + \phi_l\right]\right\} \tag{2.6}$$

where $E_{0,l}$ and ϕ_l are the amplitude and phase of mode l.[50] Normally, each individual mode will have a random onset compared to the other modes, resulting in a random phase relationship between modes giving continuous wave (CW) operation. The square of the electric field of 31 modes with equal amplitudes ($E_{0,l} = E_0$) and random phases

is shown in the top panel of Figure 2.4. Because there is no phase relationship between the modes there are points in time where the modes add constructively and points in time where they add destructively giving an average value depicted by the dashed line. Note that the random pattern still repeats with a period of $T = 2d/c$.

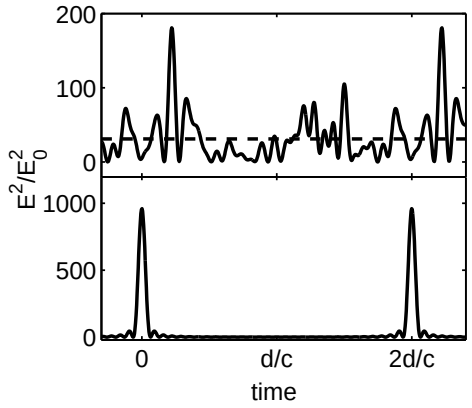

Figure 2.4: Square of the electric field for 31 modes in a cavity with random (top) and locked (bottom) phases. All of the modes have the same amplitude, E_0. In the top panel the dashed line is the average of the squared electric field which is proportional to the CW power. Note that the y-axes are on different scales for the top and bottom panels.

If, by luck or ingenuity, all the modes began at once, the phases would have equal value ($\phi_l = \phi_0$) and all of the modes would add constructively giving a large initial pulse.[51] The laser then gives a pulse train with period $T = 2d/c$. The bottom panel of Figure 2.4 shows this for 31 modes with equal amplitudes and phases. The code for making Figure 2.4 is given in Appendix A.4. The process of locking the phases is called

mode-locking and a laser in which the phases are locked is referred to as being mode-locked. While the above description assumed equal amplitudes for each mode, similar results are arrived at for a more realistic Gaussian distribution of mode amplitudes.[50]

There are multiple ways to mode-lock a laser including active and passive methods. One example of an active mode-lock would be to place an amplitude modulator near one end mirror of the cavity to introduce oscillatory loss to the cavity. If the modulator is driven at the frequency $\Delta\omega$ and is only at low loss for a small amount of time, lasing will only occur when the phases are locked creating a mode-locked pulsed laser. As the pulse approaches the modulator, the modulator will switch to low loss allowing the pulse through. After the pulse passes through the modulator, the modulator switches back to high loss preventing non-mode-locked (CW) lasing.[52]

An example of passive mode-locking is Kerr-lens mode-locking. In this technique, CW and pulsed laser modes travel through the cavity with different focal parameters due to self-focusing caused by the Kerr effect. The Kerr effect is a nonlinear optical response in which the refractive index of a material is dependent on the intensity of the light traveling through it.[51] A beam with a Gaussian profile has a higher intensity in its center which will experience, in most materials, a higher index of refraction compared to the low intensity wings of the beam profile. This refractive index gradient along the beam profile is similar to that provided by a convex lens and results in focusing of the beam.[50] This self-focusing results in pulsed mode-locked beams being more tightly focused than CW beams due to their higher peak intensities.

To promote mode-locked operation a hard or soft aperture is used as shown in Figure 2.5. A hard aperture, such as an iris, can physically block out the CW mode, while allowing the tighter focused mode-locked pulse to pass through. In a soft aperture, the pump laser, which provides the optical gain in the kerr medium, is focused such that the smaller mode-locked beam entirely overlaps with the pump, but the larger CW beam only partially overlaps, reducing gain. Both of these approaches encourage pulsed mode-locked operation over CW operation.

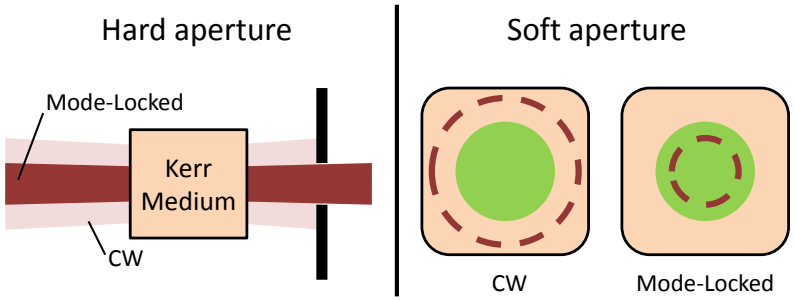

Figure 2.5: Hard and soft apertures used in Kerr-lens-mode-locking. Left: Hard aperture. CW beam (light red) is blocked by the physical aperture, while the mode-locked beam (dark red) passes through. Right: Soft aperture. Cross section diagram of the Kerr medium. CW beam does not fully overlap with the pump (green circle) reducing the gain, while the mode-locked beam fully overlaps increasing gain.

The oscillator used in this work is a Kerr-lens mode-locked oscillator utilizing a soft aperture as shown in Figure 2.6.[53;54] The oscillator is pumped by a Spectra-Physics Millennia Pro which outputs 3.0 W of s-polarized, CW light at 532 nm. The beam is directed through a twisted periscope which adjusts the beam to the desired height and changes the polarization to p-polarized. The beam is then directed and focused by a

532 nm dichroic mirror and a focusing lens into a 4 mm, 0.25% doped, Brewster cut titanium-sapphire (Ti:Sapph) crystal. Emission of the Ti:Sapph traverses the cavity which consists of two focusing cavity mirrors and two end mirrors, one of which is the output coupler. Each pass through the Ti:Sapph gives further stimulated emission (gain). To account for the dispersion created by the cavity, mostly from passing through the Ti:Sapph crystal, the beam is directed through a fused silica prism pair set at Brewster's angle. The distance between the prisms is approximately 53.5 cm.

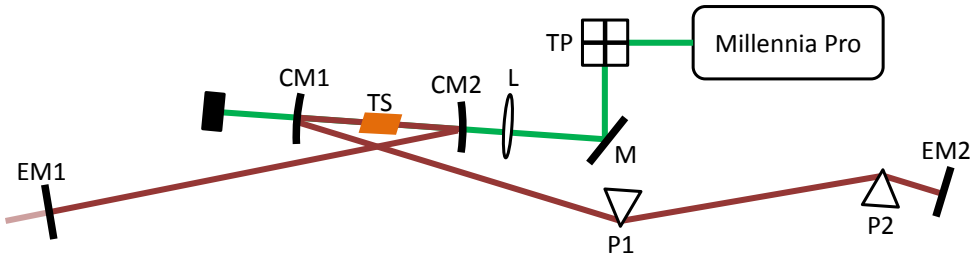

Figure 2.6: Schematic of Ti:Sapphire oscillator. TP: twisted periscope, M: 532 nm dichroic mirror, L: focusing lens, TS: Ti:Sapph crystal, CM1/CM2: focusing cavity mirrors, EM1: end mirror and output coupler, EM2: end mirror; P1/P2: fused silica prism pair.

The focus of the 532 nm pump laser is chosen such that it acts as a soft aperture for Kerr-lens mode-locking. To mode-lock the system, the translation stage prism 2 (P2) is mounted on is rapidly adjusted back and forth. Once mode-locked the laser pulse will continue cycling through the oscillator cavity. Each time the pulse is incident on the output coupler (EM1) a portion is transmitted. Typically, mode-locking increases the output power from 100 mW to 150 mW and the bandwidth from $<$5 nm to $\sim$40

nm centered at 800 nm. The repetition rate ($f = c/2d$ where d is the cavity length) is approximately 85 MHz and the pulse width is between 5 and 10 fs.

2.4.2 Pulse Stretching and Compressing

The output of the oscillator is a pulse train with very high repetition rate and low pulse energies (<2 nJ/pulse). Before selecting and amplifying a pulse, the pulses are stretched in time to prevent damaging optics during the amplification process. After amplification the pulses are recompressed. Further compression is necessary if the wavelength of the beam is adjusted using noncollinear parametric amplification (NOPA).

A laser pulse that travels through a medium will experience group velocity dispersion (GVD) due to different wavelengths of the pulse experiencing different indices of refraction. For a given material, the relationship between wavelength and index of refraction is approximated using the Sellmeier equation.[51] In most materials GVD results in shorter wavelengths lagging behind longer wavelengths giving positive GVD and, what is called, an up-chirped pulse.[51] The output pulses of the oscillator could be stretched by passing them through a large amount of material with high GVD, but this would also introduce aberrations and higher order chirp which is difficult to correct for after amplification. Instead a grating stretcher is used. A simplified schematic is shown in Figure 2.7. The beam is refracted off of a grating and imaged using a pair of focusing optics onto another grating. A mirror is then used to return the beams on the same path with a slight vertical angle change. By controlling the distance the gratings

are from the focusing optics, the path length becomes wavelength dependent creating GVD. If the gratings are moved closer, redder wavelengths travel less distance giving positive GVD (stretcher). If the gratings are separated, redder wavelengths travel more distance giving negative GVD (compressor).

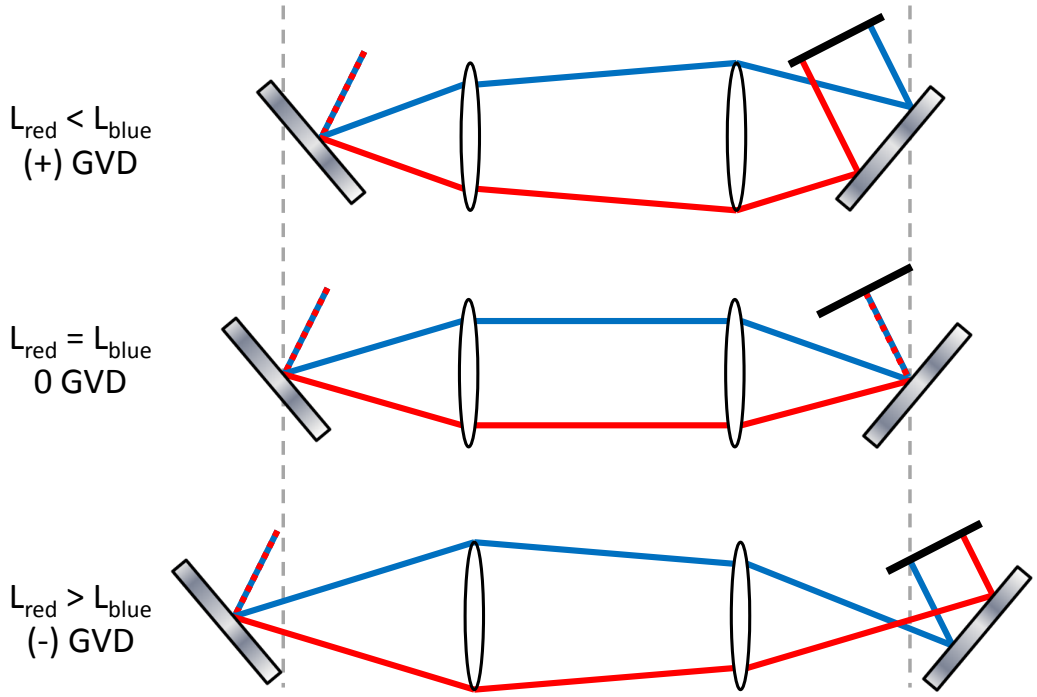

Figure 2.7: Simplified schematic of pulse stretcher/compressor. Gratings are shown by shaded rectangles, lenses by white ovals, and the return mirror by the black lines. Grey dashed lines are to help guide the eye. Redder wavelengths in the incident beam (left side) are diffracted more than bluer wavelengths. When the gratings are placed at the object and image of the lenses both wavelengths travel the same distances and there is zero GVD (middle). When the gratings are pushed closer to the lenses, redder wavelengths travel less distance resulting in positive GVD (stretcher, top). When the gratings are pulled away from the lenses, redder wavelengths travel more distance resulting in negative GVD (compressor, bottom).

The actual stretcher used is a folded version of that shown in Figure 2.7. It uses all reflective optics to prevent higher order chirp and only one grating (1500 grooves/mm) for easier adjustment.[55] After passing through the stretcher the beam is amplified as will be discussed below. After amplification the pulse is compressed by reversing the stretching process. The compression also takes into account GVD introduced during amplification and any GVD that the pulse will experience in the experimental setup. The compressor setup used is a four-pass, double-grating compressor with an efficiency of ∼65%.[56] If the NOPA is used, further compression of the NOPA output is needed. This is done with an analogous four-pass, double-prism compressor.[57]

2.4.3 Regenerative amplification

The output from the stretcher is directed into a Ti:Sapph regenerative amplifier (regen) to increase the pulse energy.[58;59] A schematic of the regen is shown in Figure 2.8. The regen cavity consists of two cavity mirrors coated to reflect 800 nm light and transmit 527 nm light and an end mirror coated to reflect 800 nm light. During alignment the end mirror can be replaced by a 95% output coupler. The gain medium is a 4 mm, 0.25% doped, Brewster cut Ti:Sapph crystal. The pump laser is a pulsed Spectra Physics Empower 15 which outputs 10 W of p-polarized 527 nm light. The pump beam is directed to the crystal by 527 nm dichroics. The beam is focused to a waist of ∼470 µm by first using a telescope to increase the beam size and then a focusing mirror. Pump light not absorbed by the Ti:Sapph is refocused on the crystal by a focusing 527 nm

dichroic mirror. When the output coupler is used the measured power is 1.2 W at 1 kHz repetition rate.

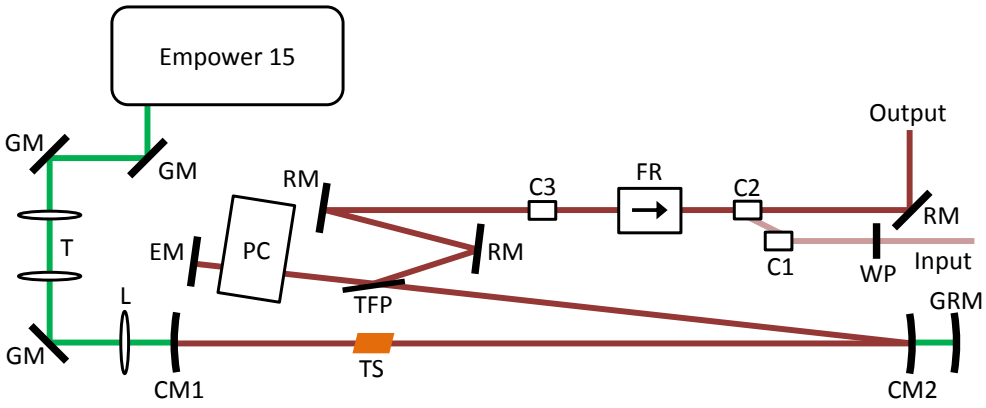

Figure 2.8: Schematic of Ti:Sapph regenerative amplifier. GM: 527 nm dichroic mirrors, T: telescoping lens pair, L: focusing lens, CM1/CM2: focusing cavity mirrors, GRM: 532 nm focusing dichroic mirror, EM: end mirror, PC: Pockels cell, TFP: thin film polarizer, RM: 800 nm dichroic mirrors, C1/C2/C3: polarizing cube beamsplitter, FR: Faraday rotator, WP: half waveplate.

The p-polarized pulse train coming from the stretcher, called the seed, passes through a half waveplate tuned to adjust the beam to be s-polarized. The seed is reflected off of two polarizing cube beamsplitters and passes through a Faraday rotator in the reverse direction so that the polarization is not adjusted. A rotated polarizing cube beamsplitter (C3) is placed such that s-polarized light is transmitted. This cube is used to ensure the polarization of the regen input and output is well-defined. The s-polarized seed is then reflected off of a thin film polarizer placed in the laser cavity. Normally the s-polarized seed would reflect off the end mirror and then reflect off of the thin film

polarizer leaving the regen cavity.

A Pockels cell (Thales Laser MEDOX) is used to trap a pulse in the cavity. When a particular voltage (∼3.5 kV) is applied to the Pockels cell, light that passes through the cell experiences a polarization change of 45°. If this voltage is applied when a seed pulse reflects off the thin film polarizer, the polarization of the seed pulse will rotate by 45°, the seed will reflect off the end mirror, and the polarizatoin will rotate by 45° again. This changes the polarization of the seed from s-polarized to p-polarized. The p-polarized seed transmits through the thin film polarizer. The voltage of the Pockels cell is then set to zero. This locks the seed pulse in the regen cavity, as it will remain p-polarized. Each time the seed pulse passes through the Ti:Sapph it will be amplified. After sufficient amplification, a voltage is applied to the Pockels cell and the polarization of the amplified pulse is changed from p-polarized to s-polarized. The s-polarized amplified pulse reflects off the thin film polarizer and through the Faraday rotator in the forward direction which changes the polarization to p-polarized. The amplified pulse that transmits through the polarizing cube beamsplitter (C2) and is directed to the pulse compressor. The input pulse energy is ∼1 nJ/pulse while the output pulse energy is ∼1 mJ/pulse giving an amplification of 6 orders of magnitude. The amplified pulse repetition rate is controlled by how often a high voltage is applied to the Pockels cell which is set to 1 kHz.

After compression, the output of the laser system is a 1 kHz pulse train with pulse energy of 650 µJ/pulse. The beam is centered at 810 nm with a bandwidth (FWHM)

of 30 nm. The pulse width, as measured by autocorrelation, is 80 fs.

2.5 Pump-Probe Experiments

This section will discuss three-wave mixing, the generation of optical pulses for pump-probe spectroscopy, and the experimental setup used to conduct pump-probe spectroscopy in this work.

2.5.1 Pump Generation

While the 810 nm output of the laser system can be used to excite some molecules, many solar cell materials of interest absorb in the visible portion of the spectrum (400-700 nm). In order to create pump pulses at these colors, second harmonic generation (SHG) and noncollinear parametric amplification (NOPA) can be used. These processes are examples of three-wave mixing which can be discussed at different levels of complexity. This section will present a simplified photon interaction approach which offers an explanation for the conditions required to achieve three-wave mixing,[51] but can not determine efficiencies, thresholds, or saturation which require the use of coupled-wave theory.[60]

Second Harmonic Generation

Imagine two photons copropagating in a material. The two photons could annihilate creating a third photon. Conversely, a single photon could annihilate creating two

photons. For these processes to occur both energy ($E = \hbar\omega$, where ω is the angular frequency of the photon) and momentum ($\mathbf{p} = \hbar\mathbf{k}$, where $\mathbf{k}$ is the wavevector of the photon) must be conserved:

$$\hbar\omega_1 + \hbar\omega_2 = \hbar\omega_3, \qquad \hbar\mathbf{k}_1 + \hbar\mathbf{k}_2 = \hbar\mathbf{k}_3. \tag{2.7}$$

The conservation of energy and momentum lead to frequency-matching and phase-matching conditions:

$$\omega_1 + \omega_2 = \omega_3, \qquad \mathbf{k}_1 + \mathbf{k}_2 = \mathbf{k}_3. \tag{2.8}$$

For collinear photons the matching conditions can be written:

$$\omega_1 + \omega_2 = \omega_3, \qquad \omega_1 n_1 + \omega_2 n_2 = \omega_3 n_3. \tag{2.9}$$

Solving both conditions in Equation 2.9 simultaneously may seem impossible due to the index of refraction being frequency dependent. For example, in SHG photon 1 and 2 have the same frequency $\omega_1 = \omega_2 = \omega$ and experience the same index of refraction, $n_1 = n_2 = n$. The first condition in Equation 2.9 requires that $\omega_3 = 2\omega$. The second condition then requires that $n_3 = n$. That is, the index of refraction in the material for frequency ω must be the same as the index of refraction for frequency 2ω. To overcome this difficulty a birefringent material is used.

In birefringent materials the index of refraction is dependent on the polarization of

incident light. Of particular interest are uniaxial crystals in which light of one polarization, called an ordinary beam, experiences a constant index of refraction $n = n_o$, called the ordinary refractive index. Light of the perpendicular polarization, called an extraordinary beam, has an index of refraction which is dependent on the angle between the wavevector (usually the direction of light propagation) and the optical axis of the crystal:

$$\frac{1}{n^2(\theta,\omega)} = \frac{\cos^2\theta}{n_o^2(\omega)} + \frac{\sin^2\theta}{n_e^2(\omega)} \tag{2.10}$$

where n_e is called the extraordinary refractive index. For a positive uniaxial crystal $n_e > n_o$, and for a negative uniaxial crystal $n_o > n_e$. The indices of refraction for the different polarizations can be pictured graphically as a circle with radius n_o for the ordinary beam and as an ellipse with radii n_o and n_e for the extraordinary beam as shown in Figure 2.9.

In order to achieve SHG $n(\omega) = n(2\omega)$. Generally, $n(\omega) < n(2\omega)$ so index of refraction surfaces have smaller radii for light with frequency ω than for light with frequency 2ω as shown in Figure 2.10. For a negative uniaxial crystal, such as beta barium borate (BBO), the indices of refraction are only equal when the fundamental (ω) is an ordinary beam and the second harmonic (2ω) is an extraordinary beam. This type of three-wave mixing is called Type-I (because the two lower frequency photons have the same polarization) o-o-e (ordinary-ordinary-extraordinary) mixing. For a positive uniaxial crystal the fundamental must be an extraordinary beam and the second harmonic an ordinary

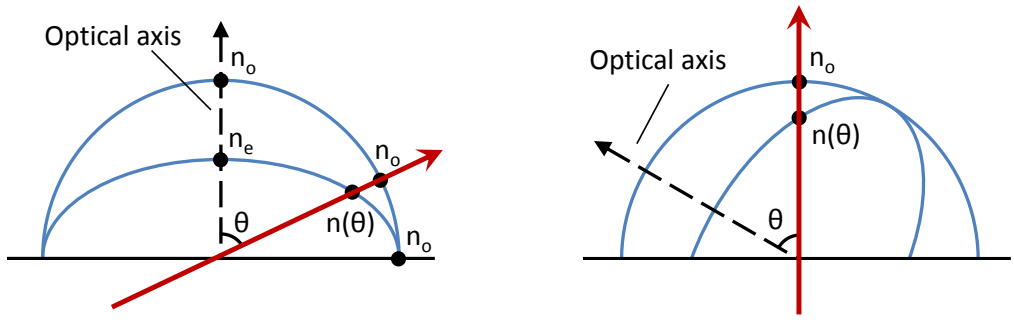

Figure 2.9: Index of refraction surfaces for a negative uniaxial crystal such as beta barium borate (BBO). Index of refraction for the ordinary beam is n_o and the ordinary surface is a circle with radius n_o. Index of refraction for the extraordinary beam is $n(\theta)$ and the extraordinary surface is an ellipse with radii n_o and n_e. A particular $n(\theta)$ can be achieved by cutting the crystal perpendicular to the optical axis and changing the incident angle of the beam (left) or by cutting the crystal to the desired angle and keeping the incident beam normal to the crystal (right).

beam which gives Type-I e-e-o mixing.[60] In either case, the second harmonic is generated with a perpendicular polarization to the fundamental. The final condition for collinear SHG is:

$$\begin{aligned} &\text{Type-I o-o-e SHG:} \qquad n_o(\omega) = n(\theta, 2\omega) \\ &\text{Type-I e-e-o SHG:} \qquad n(\theta, \omega) = n_o(2\omega). \end{aligned} \tag{2.11}$$

Equations 2.10 and 2.11 can be used to determine the required angle to achieve SHG. To double 810 nm light to 405 nm light in a BBO crystal the required angle between the incident light and the optical axis is 29°. As depicted in Figure 2.9, this can be done by adjusting the angle of the incident light or cutting the crystal at the specified

angle.

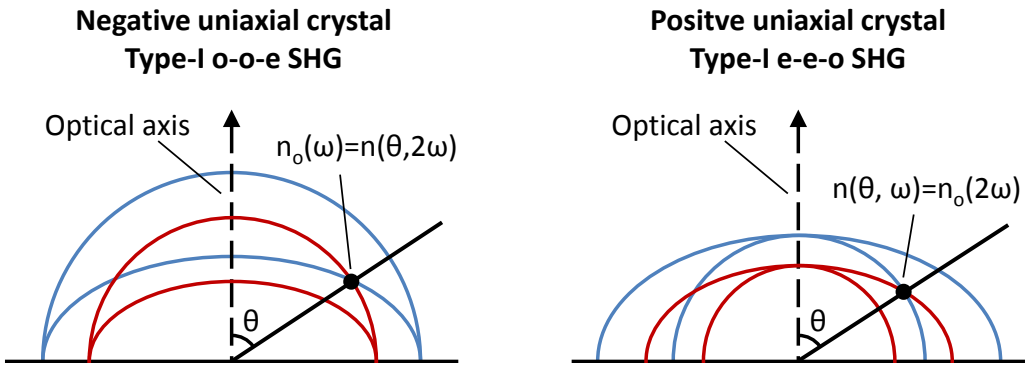

Figure 2.10: Phase matching for SHG in negative (left) and positive (right) uniaxial crystals. Ordinary and extraordinary surfaces for light with frequency ω (2ω) are shown in red (blue). The black dot and line show the angle required to achieve matching indices of refraction.

Noncollinear Parametric Amplification

Moving on to general three-wave mixing and NOPA, the scalar conditions for non-collinear three-wave mixing can be written

$$\begin{aligned} \omega_1 + \omega_2 &= \omega_3 \\ \omega_1 n_1 \sin\theta_1 &= \omega_3 n_3 \sin\theta_3 \\ \omega_1 n_1 \cos\theta_1 + \omega_2 n_2 &= \omega_3 n_3 \cos\theta_3 \end{aligned} \tag{2.12}$$

where θ_1 and θ_3 are the angles beam 1 and 3 make with beam 2 as shown in Figure 2.11. Depending on the type of mixing, each index of refraction could be ordinary (constant)

or extraordinary (angularly dependent).

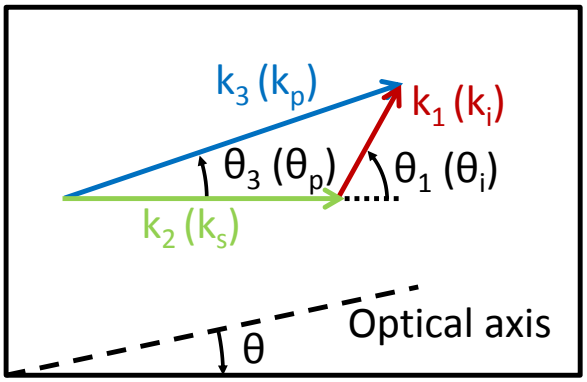

Figure 2.11: Noncollinear three-wave mixing. Labels in parenthesis are for NOPA (p: pump, s: signal, i: idler).

In the visible NOPA used in this work, an intense 405 nm pump beam ($\omega_p = \omega_3$) and a weak visible signal beam ($\omega_s = \omega_2$) are incident on a nonlinear crystal. Three-wave mixing in the crystal amplifies the signal beam and produces an infrared idler beam ($\omega_i = \omega_1$). The NOPA used is set for Type-I mixing in a BBO crystal (negative uniaxial), meaning the idler and signal are ordinary beams and the pump is an extraordinary beam. The pump frequency, signal frequency, and pump angle are chosen. The set of 3 conditions in Equation 2.12 can then be used in addition to Equation 2.10 to determine the 3 unknown quantities: idler frequency, idler angle, and crystal axis angle.[61] Plots of the crystal axis angle as a function of signal wavelength are referred to as phase-matching curves. Care should be taken when interpreting phase-matching curves as the reported angle could be between the crystal axis and the signal or the crystal axis and

the pump. Because it is often desired to have the signal normal to the crystal face, the angle the crystal should be cut at is the angle between the crystal axis and the signal. Finally, the pump angle used above is the angle between the pump and the signal in the crystal. To find the angle between the pump and signal outside the crystal Snell's law must be used.

Phase-matching curves showing the angle between the crystal axis and the signal for Type-I NOPA in BBO pumped at 405 nm are shown in Figure 2.12. Code to calculate the phase-matching angles and create these plots is given in Appendix A.5. For a pump angle (inside the crystal) of 3.7°, phase-matching is achieved for a large bandwidth of signal wavelengths if the crystal is cut at 27.3°. This means that at this pump and crystal angle, multiple colors can be amplified simultaneously allowing for a large bandwidth pulse which can be compressed to under 10 fs.[62]

A schematic of the NOPA used in this work is shown in Figure 2.13. The input p-polarized beam is split into the signal and pump beam using a beamsplitter. The transmitted signal beam is reflected off of a delay stage consisting of a retroreflector on a manual translation stage. It is then attenuated using a waveplate/polarizer and focused in a sapphire crystal to create a white light continuum beam. The white light beam is collimated by a parabolic mirror and directed to a 50 cm spherical mirror which focuses the beam to a BBO crystal cut for efficient Type-I NOPA between visible and 400 nm light (Newlight Photonics). The pump beam reflected off of the beamsplitter is directed through a polarizer and a BBO cut for 800 nm to 400 nm SHG (Newlight

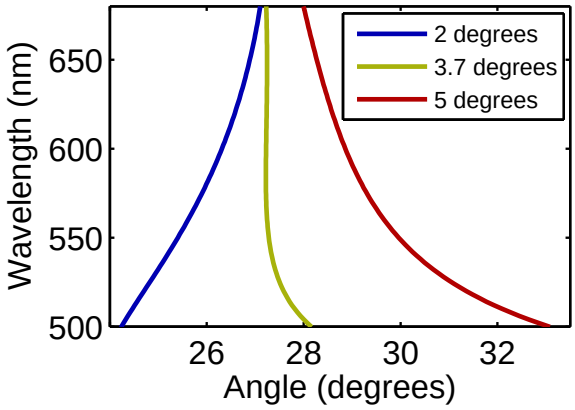

Figure 2.12: Phase-matching curves for Type-I NOPA in BBO with a pump wavelength of 405 nm at different pump angles. The angle reported is the angle between the crystal axis and the signal beam.

Photonics). The BBO is set to create an s-polarized pump beam which is directed through a 75 cm convex lens focusing the pump beam towards the NOPA BBO. The focus of the pump beam is kept slightly after the BBO to prevent crystal damage and increase the signal/pump overlap.

For light amplification to occur the pump and signal beams need to be spatially and temporally overlapped and the NOPA BBO needs to be set to the phase matching angle. The spatial overlap is controlled by the last pump mirror, the temporal overlap is adjusted by moving the retroreflector, and the phase matching angle is tuned by rotating the NOPA crystal. Fused silica windows can be placed in the pump line to increase the temporal width of the pump so that it temporally overlaps with more wavelengths of the chirped white light. This increases the bandwidth of the amplified pulse to as high

as 100 nm FWHM. Conversely, the fused silica windows can be placed in the white light to further chirp it and reduce the wavelengths which temporally overlap with the pump pulse decreasing the bandwidth of the amplified pulse. This is useful for selectively pumping a specific transition of a sample. The output of the NOPA is tunable from 480-700 nm with pulse widths under 60 fs (FWHM) as measured by cross-correlation with the 810 nm laser output. Pulse energies are ∼200 nJ as measured directly after the prism compressor.

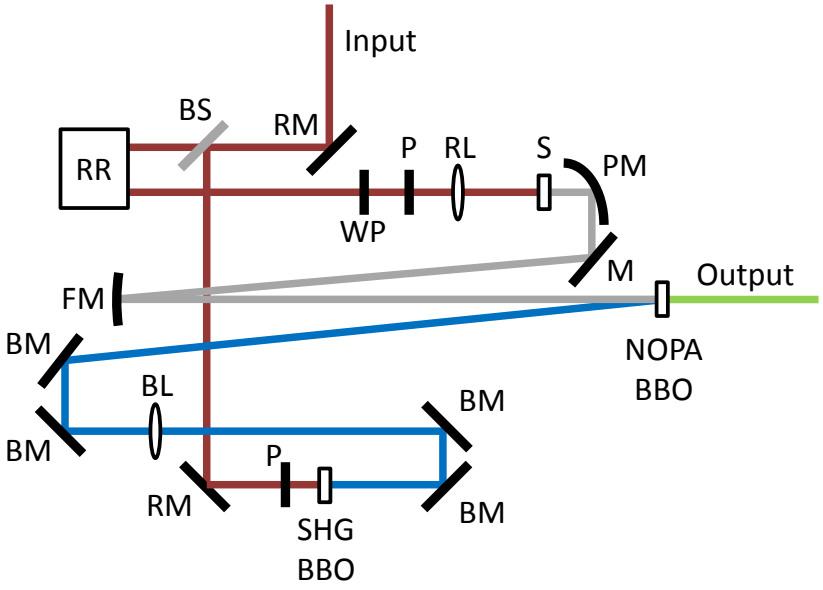

Figure 2.13: Schematic of NOPA. RM: 800 nm dichroic mirror, BS: beamsplitter, RR: retroreflector, WP: half waveplate, P: grid polarizer, RL: 10 cm focusing lens, S: sapphire crystal, PM: 2 inch effective focal length parabolic mirror, M: silver mirror, FM: 50 cm focusing silver mirror, SHG BBO: BBO crystal for 800 nm to 400 nm SHG, BM: 400 nm dichroic mirror, BL: 75 cm focusing lens, NOPA BBO: BBO cut for NOPA between visible and 400 nm light. Red Lines: 810 nm beams, Grey Lines: white light beams, Blue Lines: 405 nm beams, Green Line: amplified visible beam.

2.5.2 Probe Generation

The output of the laser system, its harmonics, or the output of the NOPA could be used to collect single-color pump-probe data. If the NOPA output has sufficient bandwidth it could be used to collect full-frequency pump-probe data. Another approach is to focus a portion of the 810 nm output of the laser system into an optical medium to produce a white light continuum used as the probe beam. As the 810 nm beam is focused in the medium it experiences self-focusing creating a more tightly focused beam. This continues until the electric field of the beam is sufficiently large enough to induce a multitude of nonlinear effects such as self-phase modulation, self-steepening, filamentation, and photo-ionization which result in the creation of a white light continuum.[63;64] Sapphire crystals are one of the most commonly used materials in white light generation giving a spectrum that stretches from 450 nm into the near IR. Calcium fluoride crystals can be used to create a white light continuum reaching wavelengths as short as 380 nm, but the crystals need to be continuously moved to prevent optical damage.[65] Using a white light continuum as a probe beam allows for full-frequency pump-probe spectra to be collected stretching across the visible into the near IR.

2.5.3 Pump-Probe Setup

A schematic of the pump-probe setup is shown in Figure 2.14. The pump beam is modulated at half the laser repetition rate using a chopper wheel (New Focus 3501). Both the pump and the probe beams reflect off automated delay stages consisting of

retroreflectors (PLX, Inc.) on motorized stages (Newport – stages: UTM150PP.1; controller: ESP301). Polarizations of the beams are selected using grid polarizers (Edmund Optics), while the pulse energy transmitted through each polarizer is controlled with a half waveplate. If the pump is generated using SHG (405 nm pump), the BBO crystal is placed after the polarizer in the pump line and all mirrors after the BBO crystal are 400 nm dichroics. In this case, it should be noted the polarizer selects the polarization of the 810 nm beam which is perpendicular to the polarization of the 405 nm pump beam. If the NOPA is used to generate the pump pulse (480-700 nm pump), no further optics are placed in the line and all mirrors are metallic (silver or aluminum). The white light continuum probe is generated by focusing 810 nm light into a sapphire crystal. The continuum is collimated by a parabolic mirror. The pump and probe beams are focused and crossed in the sample by a second parabolic mirror.

After passing through the sample, the pump beam is blocked and the probe beam is collimated by a lens. For single-color experiments, the probe is focused onto a diode (Thorlabs DET210) with a filter attached to only pass the wavelength of interest. Signal is recorded using a lock-in amplifier (Standford Research Systems SR830). For full-frequency experiments, the probe is focused into a monochromator (Princeton Instruments SP2150 with a 150 g/mm grating) and detected using a 256 pixel diode array (Hamamatsu – visible, 450-950 nm: S3901-256Q Si array with a C7884-20 driver; IR, 950-1650 nm: G9213-256S InGaAs array with a C8061-01 driver). The array is read out using a National Instruments data acquisition system (DAQ board: NI

PCI-6132; connector block: NI BNC-2110). A 1 mm cuvette containing 1,1'-diethyl-4,4'-dicarbocyanine iodide (Sigma-Aldrich) in methanol is placed directly before the monochromator entrance slit to absorb residual 810 nm light in the probe beam which can saturate the diode array. Wavelength calibration of full-frequency data is conducted using a series of well-defined pass filters. Temporal dispersion due to white-light chirp is accounted for by collecting cross-phase-modulation between the pump and probe in the neat solvent or bare substrate. Fitting the cross-phase-modulation gives time zero for each wavelength, allowing for the creation of a chirp-curve.[66]

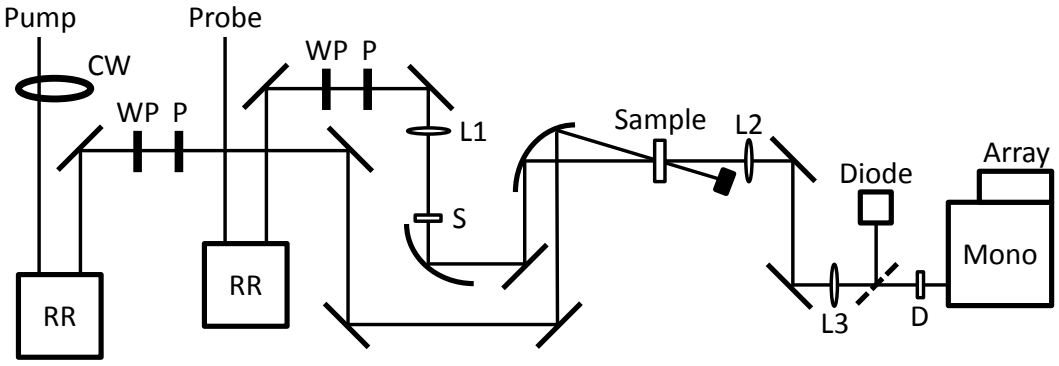

Figure 2.14: Schematic of pump-probe setup. Solid lines are flat mirrors, curved lines are focusing parabolic mirrors, and the dashed line is a flip-up mirror. CW: chopper wheel, RR: retroreflector, WP: half waveplate, P: grid polarizer, L1: 10 cm focusing lens, S: sapphire crystal, L2/L3: 15 cm focusing lens, D: dye cell, Mono: monochromator.

Chapter 3

The Nature of Excitons in P3HT Thin Films with Varying Aggregation

3.1 Introduction

Thin films of π-conjugated polymers are among the most widely used materials in organic photovoltaics (OPVs) with efficiencies reaching 10.7%.[8;67] Poly(3-hexylthiophene) (P3HT) is one such conjugated polymer consisting of conjugated thiophene rings with attached hexyl-chains. Coupling between monomer units can occur as head-tail, head-head, or tail-tail coupling. In regiorandom P3HT (rraP3HT), this coupling is random, while in regioregular P3HT (rrP3HT) only head-tail coupling is present (Figure 3.1).

In solution, rrP3HT and rraP3HT behave similarly, but in the solid state they have very different characteristics. In rrP3HT thin films, π-stacked aggregates can form, resulting in polycrystalline films with both aggregate and amorphous domains, while rraP3HT thin films are amorphous due to steric interactions of the side chains inhibiting π-stacking.[68;69;70] The formation of aggregates results in a redshifted film absorption which is apparent by the color of the films and their absorption spectra as shown in Figure 3.1.

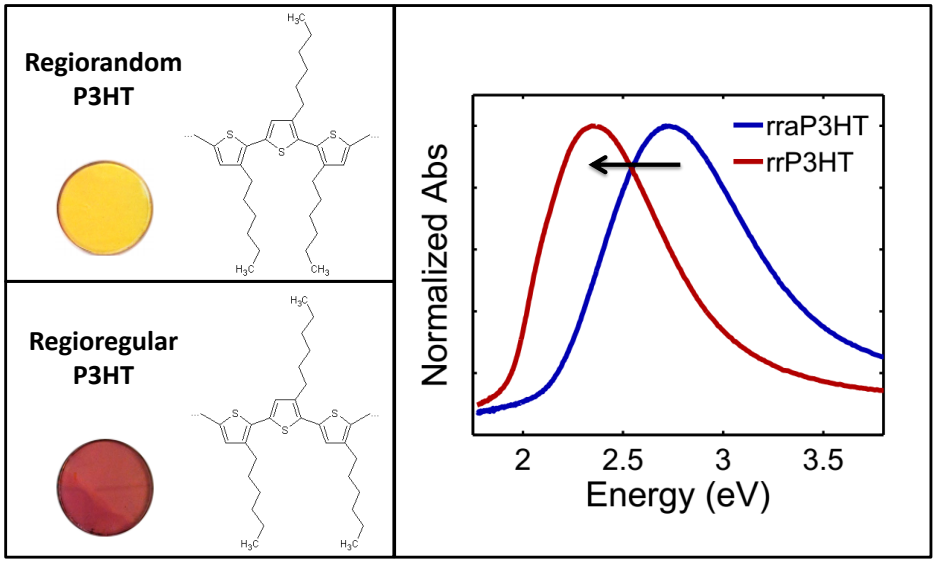

Figure 3.1: Left: structure and photograph of films for rraP3HT and rrP3HT. Right: normalized absorption spectrum for rraP3HT and rrP3HT.

Increasing aggregation has been shown to increase OPV efficiencies, causing rrP3HT to be more commonly used in devices.[71] The characteristics of the starting polymer, the parameters of the thin-film synthesis, and post-processing techniques all have an effect

on the amount of aggregation and, in turn, device efficiency.[72;73;74;75] More aggregation in the films allows for better charge (hole) transport through the π-stacks after exciton dissociation which increases efficiency.[75;76] On the other hand, the effect of π-stacking on the behavior of excitons before dissociation is not well understood. To further optimize OPVs, understanding the nature of excitons in conjugated polymers as a function of aggregation is necessary.

Previously, aggregation has been studied by adding poor solvents to rrP3HT solutions,[77;78] but the unknown extent and type of aggregation in the solutions makes comparisons to thin film P3HT difficult. In the current study, the amount of aggregation of thin films is controlled by spin coating films from solutions containing a mixture of rrP3HT and rraP3HT. We show the amount of aggregation present in a film can be controlled by introducing rraP3HT to a rrP3HT solution before spin coating. By varying the ratio of rrP3HT to rraP3HT the aggregation can range from that of a fully rrP3HT film to an amorphous film. In order to improve the aggregation of a rrP3HT film further, the film can be thermally annealed allowing molecules to sample more configurations, fostering the creation of energetically favorable aggregates.[79]

Exciton dynamics of P3HT thin films have been studied in the past via photoluminescence (PL) decay,[80;81;82] but these measurements probe only a small fraction of excitons present due to the low PL quantum yield (QY) of the films.[83] Low QYs in conjugated polymer thin films have been attributed to excitons trapping to aggregates,[84] implying PL studies are bias to excitons in amorphous or poorly aggregated domains. In

contrast, ultrafast pump-probe spectroscopy measures the change in absorption of the film due to excitation. Every excitation contributes to this change in absorption, and the photophysics of the less-emissive species, which make up the majority of the excitations in rrP3HT films, can be more accurately measured. Previous pump-probe studies have examined exciton behavior in rrP3HT films when fullerene derivatives are added, which act as electron acceptors and reduce the P3HT aggregation.[85;86] The change in exciton decay pathways due to the presence of the fullerenes masks any changes due to altering of the P3HT aggregation. In the current report the structure of the film is adjusted using only P3HT isomers allowing for the effect of aggregation on excitons in P3HT to be examined.

3.2 Experimental Section

3.2.1 Sample Preparation

Solutions of rrP3HT (Reike Metals, M_n=79k) and rraP3HT (Reike Metals, M_n=91k) in chloroform were prepared with a concentration of 7 mg/mL. The solutions were mixed in different volume ratios to form solutions with the desired amount of rrP3HT. Mixed solutions were degassed by bubbling with nitrogen and filtered with a 0.45 µm syringe filter. Directly after degassing and filtering, solutions were spin coated under argon onto 1.5" quartz disks at 1400 revolutions per minute for 4 minutes. Films were stored under vacuum between experiments and all optical measurements were performed the same

day the films were spun. Annealing was conducted under vacuum at 120 °C for 1 hour.

3.2.2 Differential Scanning Calorimetry

Differential scanning calorimetry (DSC) measurements were conducted using a TA Instruments Discovery DSC. Samples were prepared from the same solutions that the thin films were cast from. Small amounts of the solution were drop cast into aluminum Tzero pans and dried in a box with a positive nitrogen pressure. This was repeated until the necessary amount of P3HT was present in the pan (approximately 1-3 mg). Samples were heated from 40 °C to 270 °C, cooled from 270 °C to 0 °C, and then heated again from 0 °C to 270 °C. Reported data is from the cooling sweep and the second heating sweep. Temperature ramps were conducted at a rate of 10 °C/min and all measurements were conducted under nitrogen.

3.2.3 Steady-State Spectroscopy

UV-vis absorption spectra were obtained using a Cary 14 spectrophotometer, while PL spectra were obtained using a SPEX Fluorolog 1680 (Chapter 2). All PL spectra were obtained in front face geometry and excited at 2.5 eV and 3.1 eV. Sample degradation was observed during PL measurements conducted in air. To alleviate this, all PL measurements shown were conducted with the sample chamber under positive nitrogen pressure and no sample degradation was observed. No film degradation was observed during UV-vis measurements. To account for drift in the fluorometer over time, spectra

of the laser dye DCM (Exciton) in methanol were collected with each experiment. Because the DCM standard was in solution, we did not attempt to calculate the absolute QY of the P3HT films, but instead report the relative QYs. Each PL spectra was corrected for the detector response, divided by the film absorption at the excitation energy, and then divided by the ratio of the integrated DCM emission to the DCM absorption at the excitation energy.

3.2.4 Pump-Probe Spectroscopy

Ultrafast pump-probe spectra were obtained using a home-built Ti:Sapph oscillator, regenerative amplifier, stretcher/compressor, and NOPA described in Chapter 2. Laser pulses from the system had 80 fs (fwhm) pulse widths are were produced at a repetition rate of 1 kHz. Experiments were conducted with pump energies of 2.1 eV (600 nm, NOPA output) and 3.1 eV (405 nm, SHG of 810 nm fundamental). The probe pulse was a white-light continuum that ranged from 1.7 to 2.7 eV. The pump polarization was kept at the magic angle (54.7°) relative to the probe to isolate isotropic exciton dynamics. The pump was focused before the sample to produce a larger spot size at the film (400 µm fwhm) to keep the exciton density low and minimize interactions between excitons such as exciton-exciton annihilation. After passing through the sample, the probe beam was directed through a monochromator (Princeton Instruments SP2510i) and detected using a 256 pixel silicon diode array (Hamamatsu) giving a resolution of 2 nm per pixel.

The probe beam was measured for every laser pulse, while the pump beam was modulated at half the laser repetition rate. The change in optical density, ΔOD, induced by the pump was calculated for each pulse pair. Reported ΔOD values were found by averaging 25,000 pulse pairs for each time point. This entire process was then repeated multiple times to ensure that there was no change in the sample due to degradation. All runs were then averaged together to give the final ΔOD spectra. Degradation was observed when the sample was in air or if the sample was left static under laser illumination. All reported spectra were collected with the films rotating at approximately 5 rotations per second in a box with positive nitrogen pressure and showed no signs of degradation. The pump pulse energies were between 10 and 20 nJ depending on the absorption of the film.

3.3 Results and Discussion

3.3.1 Controlling Aggregation

Absorption spectra for as spun P3HT films with varying rrP3HT:rraP3HT ratios are shown in Figure 3.2.a. Because fully rraP3HT films are predominantly amorphous[69] we assign the rraP3HT absorption spectrum to that of amorphous P3HT domains. For the other spectra, the overall absorption is the sum of absorption from aggregate and amorphous domains. Aggregate absorption is redshifted and more structured when

compared to amorphous absorption due to delocalization of the wave function and decreased inhomogeneous broadening, respectively.[87] Because films with higher rrP3HT content have a redshifted and more structured absorption we conclude that increasing the amount of rrP3HT increases aggregation.

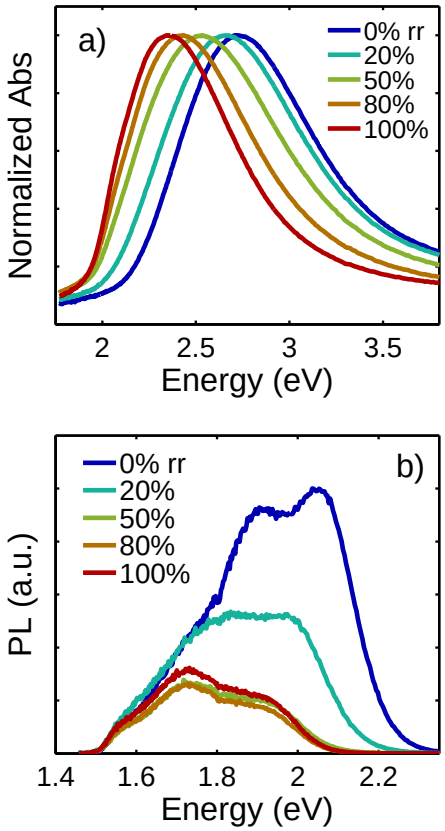

Figure 3.2: Absorption (a) and emission (b) of mixed rrP3HT/rraP3HT thin film. For the emission, the films were excited at 2.5 eV.

DSC was employed to further support this conclusion. The DSC results in Figure 3.3 show that both the melt and melt crystallization peaks narrow and increase in area with

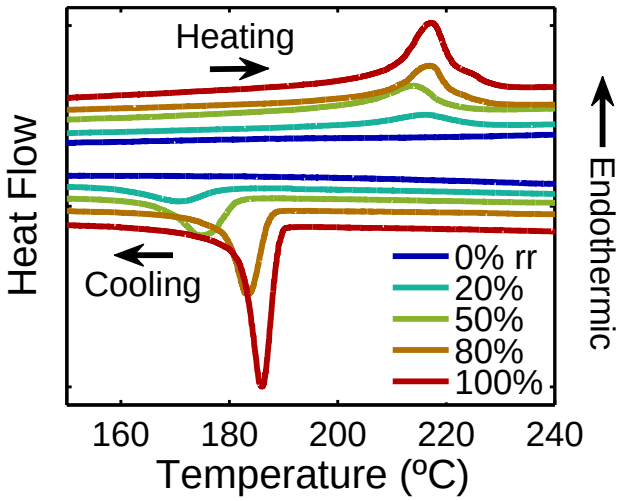

Figure 3.3: DSC traces of mixed rrP3HT/rraP3HT samples. Bottom traces are the cooling sweep and top traces are the second heating sweep. Traces have been translated for clarity.

higher rrP3HT content. No melt or crystallization is observed in the rraP3HT sample signifying an amorphous film, as expected.[69] The narrowing and increase in area of the melt and melt crystallization peaks with higher rrP3HT content represent an increase in overall aggregation, similar to results for rrP3HT:PCBM films of different ratios.[88] The enthalpy of fusion of each sample was found by integrating under the melt peak. Comparing the enthalpy of fusion of the films to that of P3HT aggregates, the percent aggregation can be estimated.[89] An ideal P3HT crystal has an enthalpy of fusion of ΔH_m^∞=99 J/g.[90] Because the aggregated domains in thin films have some disorder, a correction factor to ΔH_m^∞ must be applied to approximate the enthalpy of fusion of the

aggregates which gives $\Delta H_m^a \approx 45$ J/g.[91] The ratio of the measured enthalpy of fusion to that of the aggregates gives the percent aggregation of each film as shown in Figure 3.4 along with the peak value of the absorption spectra. Note that both the absorption peak and the percent aggregation as found by DSC follow a linear trend with added rrP3HT. While the absolute values for the percent aggregation are approximate, it is clear that as more rrP3HT is used more aggregation occurs. This ability to control the amount of aggregation gives us the opportunity to study photophysics of P3HT films as a function of aggregation.

3.3.2 Quenched Fluorescence From Aggregate Domains

The PL for the P3HT films excited at 2.5 eV is shown in Figure 3.2.b. With increased rrP3HT the PL spectra redshift, change shape, and are quenched. Analysis of the PL shape can be used to understand the nature of the emission in the films. According to Kasha's Rule emission occurs from the lowest vibrational level of the first excited state to different vibrational levels of the ground state, giving the P_{0-0}, P_{0-1}, P_{0-2}, etc. features in order of decreasing energy.[41] For intramolecular emission, the relative amplitudes of these features correspond to a Franck-Condon progression.[25]

The rraP3HT emission could be fit to a Franck-Condon progression, as shown in Figure 3.5.a, signifying intramolecular emission, as expected for an amorphous film where there is little intermolecular interaction. The PL of the rrP3HT and mixed rrP3HT:rraP3HT films could not be adequately fit with a Franck-Condon progression

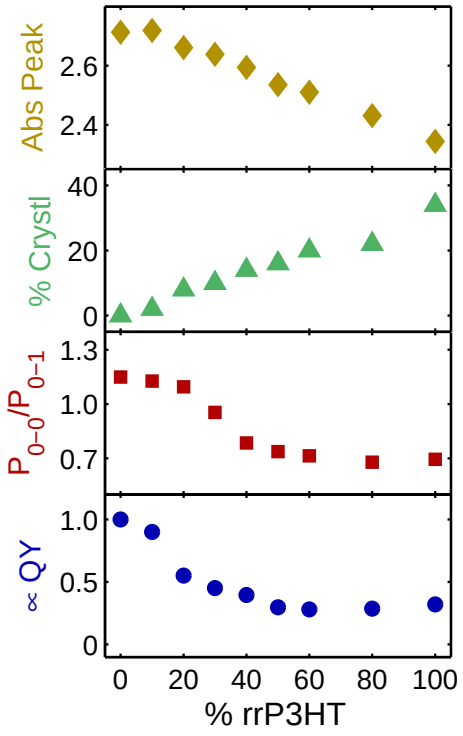

Figure 3.4: Absorption peak (yellow diamonds), % aggregation (green triangles), P_{0-0}/P_{0-1} ratios (red squares), and relative quantum yields (blue circles) as a function of % rrP3HT

as illustrated by the poor fit to the rrP3HT emission in Figure 3.5.a. Instead, the emission from these films was fit using a series of Gaussians with free floating weights to model emission from aggregates where intermolecular interactions cause non-Franck-Condon behavior. A component consisting of the rraP3HT PL spectrum was added to the fit to represent emission from the amorphous domains, but the weight optimized to zero in all cases, implying emission is predominantly from the aggregate domains for the rrP3HT film and the mixed films. The overall fit for the 20% rrP3HT film is shown

in Figure 3.5.b along with the underlying Gaussian lineshapes.

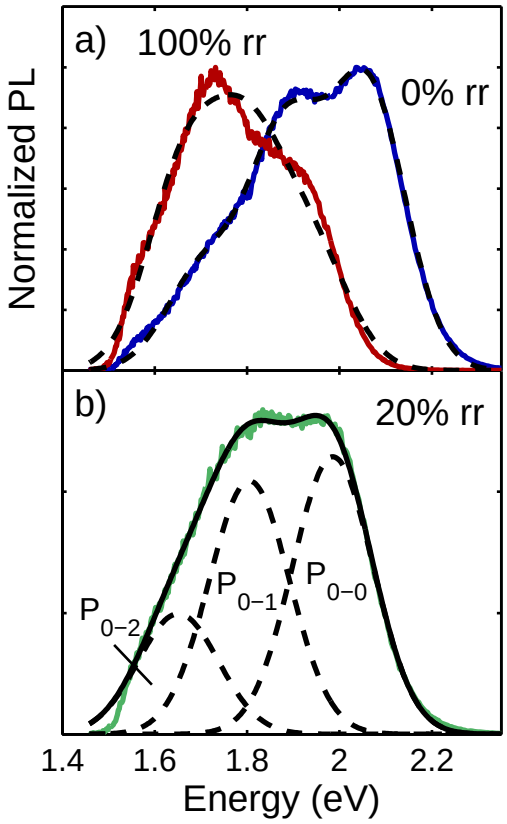

Figure 3.5: (a) Franck-Condon fits (dashed black lines) for PL from films with 0% rrP3HT (blue) and 100% rrP3HT (red). (b) Non-Franck-Condon fit (solid black line) for PL from 20% rrP3HT film (green) using free floating weights for each Gaussian (dashed black lines).

As the percent of rrP3HT increases the P_{0-0} : P_{0-1} ratio decreases as shown in Figure 3.4. The decrease in ratio is consistent with the formation of weakly coupled H-aggregates.[92] In ideal H-aggregates at 0 K there is zero oscillator strength between the lowest vibrational levels of the ground and excited states resulting in the complete

suppression of the P_{0-0} feature.[93] The P_{0-0} feature may not be completely suppressed due to thermal effects or disorder in the aggregates.[92] Because all PL measurements were conducted at room temperature, the observed difference in the P_{0-0} amplitude between samples is concluded to be from disorder in the aggregates. There is a large decrease in P_{0-0} : P_{0-1} ratio between 20-40% rrP3HT after which the ratio decreases more gradually. We conclude that more ordered H-aggregates form with increased rrP3HT content with a large change in order occurring between 20-40%. The decrease in PL QY (Figure 3.4) with increased rrP3HT content is also consistent with the formation of H-aggregates due to the suppressed P_{0-0} peak as well as the suppression of the sideband peaks.[92]

Because of the low QY and shape change of the PL spectra, we propose that emission is predominantly from the more organized domains in films with as little as 20% rrP3HT similar to the conclusion by Clark et al. that PL from fully rrP3HT films is dominated by aggregate emission.[94] Note that the PL excitation energy of 2.5 eV is able to create excitons in the amorphous domains (see rraP3HT absorption spectrum in Figure 3.2.a). To create the majority of the excitons in the amorphous domains we also collected PL from the films with an excitation energy of 3.1 eV and observed similar PL spectra and relative QYs as when excited at 2.5 eV as shown in Figure 3.6. Thus, excitons must transfer from the amorphous domains to the H-aggregate domains before significant PL occurs even in 20% rrP3HT films which have a small amount of aggregation (8% as measured by DSC). In order to determine the timescale of this exciton transfer,

pump-probe spectroscopy was employed and will be discussed in Section 3.3.4.

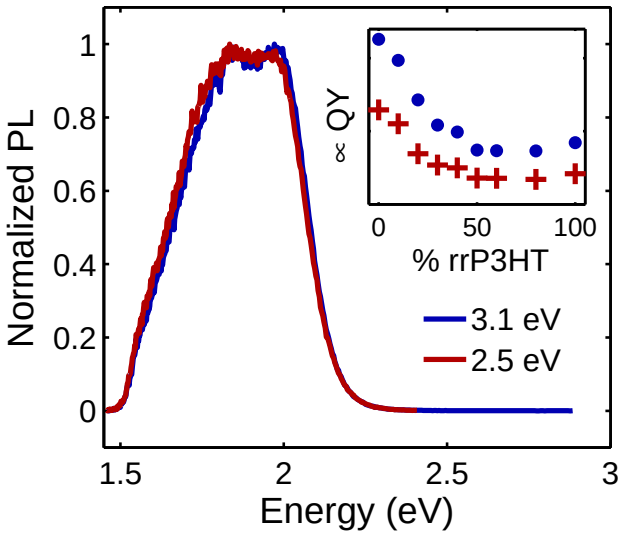

Figure 3.6: Emission of a 20% rrP3HT film excited at 3.1 eV (blue) and 2.5 eV (red). Inset: Relative quantum yields of P3HT films as a function of % rrP3HT when excited at 3.1 eV (blue circles) and 2.5 eV (red crosses).

3.3.3 Annealing to Increase Aggregation

Figure 3.7.a shows absorption and PL of a rrP3HT film as spun and after annealing. The absorption spectrum in the annealed film is more structured due to reduced inhomogeneous broadening caused by more ordered aggregates, while the emission of the annealed film is further quenched due to annealing decreasing site disorder.[92] The increased structure in the absorption spectrum of the annealed film allows for analysis of its shape.

In all the films containing aggregates, the overall absorption spectrum is the sum of

absorption from the aggregate domains and the amorphous domains. The amorphous component should be similar to the rraP3HT absorption spectrum, while the aggregate component can be modeled as a series of broadened peaks: A_{0-0}, A_{0-1}, A_{0-2}, etc. in order of increasing energy. In weakly coupled H-aggregates with a Huang-Rhys factor of approximately 1 the ratio of the 0-0 and 0-1 amplitudes, $R = A_{0-0}/A_{0-1}$, can be related to the excitonic coupling, J, by

$$R \approx \left[\frac{1 - 0.96\, J/\omega_0}{1 + 0.292\, J/\omega_0}\right]^2 \tag{3.1}$$

where ω_0 is the energy of the phonon mode coupled to the electronic transition[95] which is taken to be the energy of the C=C stretch, ω_0=0.18 eV.[87] It should be noted that some reports present the exciton bandwidth, $W = 4\,J$, instead of the excitonic coupling, J.

The annealed absorption spectra was fit using the sum of the rraP3HT absorption spectra and a series of Gaussian peaks to find $R = 0.58 \pm 0.05$ (Figure 3.7.b) giving an excitonic coupling of $J \approx 35$ meV in agreement with previous reports.[96] Fitting parameters are given in Table 3.1. Similar attempts to fit the absorption spectra in Figure 3.2.a did not converge because of the large amount of broadening present which masks the underlying structure. As will be described below, pump-probe spectroscopy gives the opportunity to measure the absorption of the aggregate the exciton occupies as a function of time reducing broadening and allowing the spectra to be analyzed.

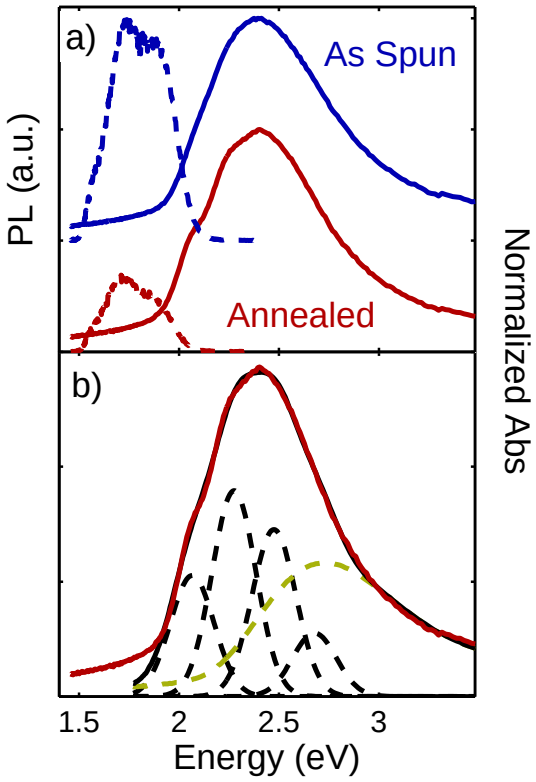

Figure 3.7: (a) Absorption (solid lines) and emission (dashed lines) of as spun (blue) and annealed (red) rrP3HT films. Spectra have been translated for clarity. (b) Fitting of annealed rrP3HT film absorption spectra (solid red line). Total fit (solid black line, coincident with absorption spectra above 1.8 eV) is the sum of Gaussian components (dashed black lines) and rraP3HT absorption (yellow dashed line).

Table 3.1: Fitting parameters for absorption spectrum of annealed rrP3HT film. One global FWHM was fit for all four Gaussians.

Gaussian	Center (eV)	Weight (%)	FWHM (eV)
1	2.07 ± 0.02	0.22 ± 0.02	0.29 ± 0.02
2	2.28 ± 0.02	0.39 ± 0.02	
3	2.49 ± 0.03	0.30 ± 0.03	
4	2.69 ± 0.03	0.10 ± 0.03	

3.3.4 Ultrafast Exciton Localization to Aggregates.

Pump-probe spectra for the fully rraP3HT film pumped at 3.1 eV are shown in in Figure 3.8. A large negative feature dominates the spectra from 1.7-2.7 eV. The lower energy portion of the feature (1.7-2.2 eV) overlaps with the inverted emission of the film, so it is attributed to stimulated emission (SE) from the excited states caused by the probe beam. The higher energy portion of the feature (2.1-2.7 eV) overlaps with the inverted absorption and is attributed to a ground state hole (GSH) resulting from the loss of ground state absorption due to excitation.

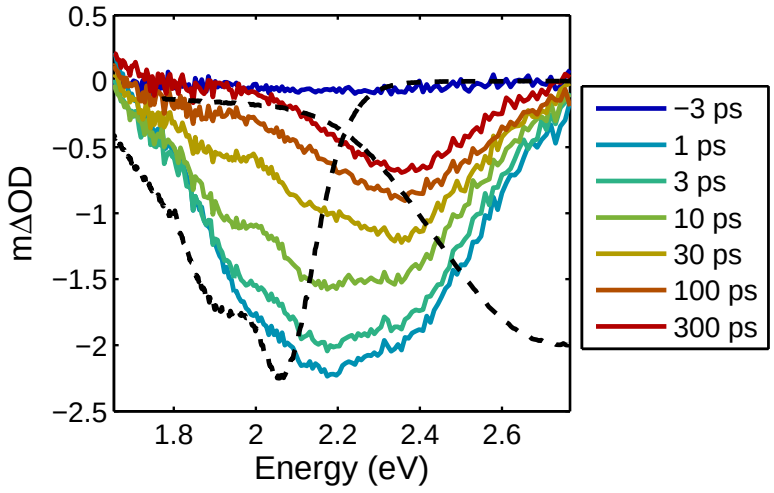

Figure 3.8: Pump-probe spectra for rraP3HT thin film. Dashed black lines depict the inverse of the film emission (lower energy) and absorption (higher energy).

Single color slices for the rraP3HT film are shown in Figure 3.9. The slice at 2.0 eV represents SE, while the slice at 2.4 eV represents the GSH. Both are formed

within the instrument response (∼100 fs) and decay over time with the GSH having an additional long-time component. The SE was fit to a biexponential decay: $A_1 \exp(-t/\tau_1) + A_2 \exp(-t/\tau_2)$, and the GSH was fit to a biexponential decay with a static offset: $A_1 \exp(-t/\tau_1) + A_2 \exp(-t/\tau_2) + A_3$. The fitting parameters are shown in Table 3.2. There are many different types of excited states present in P3HT films including singlet excitons, triplet excitons, and polarons. All of these excited states contribute to the GSH as the ground state is depopulated in all instances. Only singlet excitons have efficient emission, so SE is predominantly from singlet excitons. The two faster decays are present in both SE and GSH, so they are attributed to decay of the singlet. The third component of the GSH is due to the presence of long-lived triplets and polarons.[97]

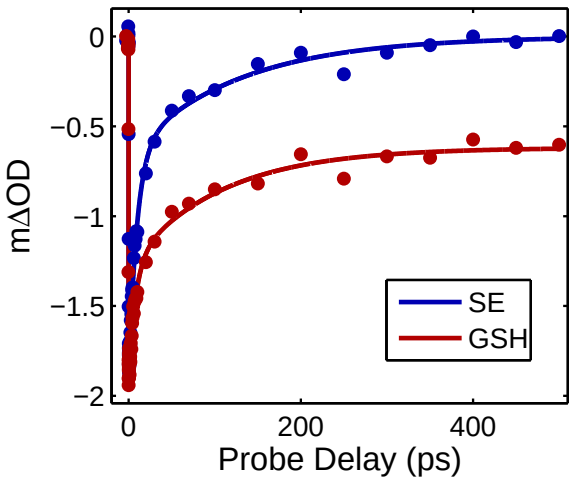

Figure 3.9: Pump-probe single color traces for rraP3HT thin film at 2.0 eV (SE, blue) and 2.4 eV (GSH, red). Fits to the data are shown by solid lines.

Table 3.2: Fitting parameters for rraP3HT film SE and GSH.

Signal	A_1 (%)	τ_1 (ps)	A_2 (%)	τ_2 (ps)	A_3 (%)
SE (2.0 eV)	66	9.5	34	130	–
GSH (2.4 eV)	34	8.0	34	106	32

Pump-probe spectra for the 100% rrP3HT film when pumped at 3.1 eV are shown in Figure 3.10. The large negative feature stretching from 2.0-2.6 eV is assigned to the GSH due to the partial overlap with the absorption spectrum. The smaller negative feature at ∼1.7 eV is due to SE as it overlaps with the film emission. The SE in the rrP3HT film is much weaker compared to the rraP3HT film in agreement with aggregation suppressing emission as shown in Figure 3.4. The GSH and SE decay with time showing no significant shape change and the average time constant of the decay (∼300 ps) is on the same order as those in previous studies.[85;98]

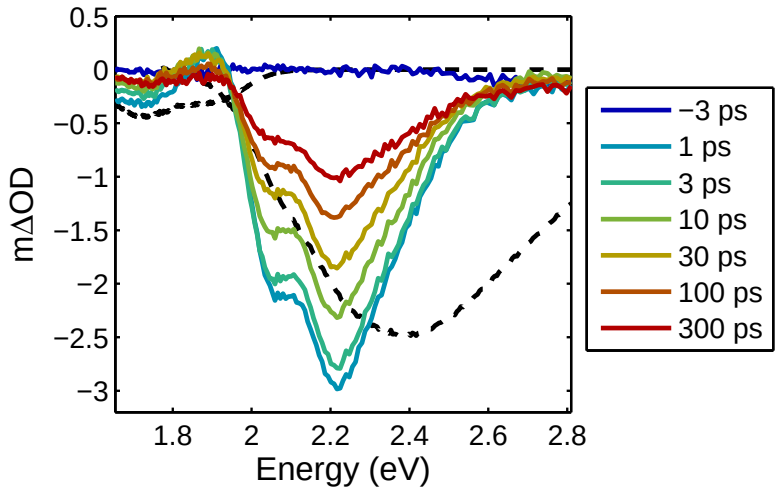

Figure 3.10: Pump-probe spectra for rrP3HT thin film. Dashed black lines depict the inverse of the film absorption and emission.

Results for the mixed rrP3HT:rraP3HT films show similar features and time constants as shown in Figure 3.11. The 20% rrP3HT film has the most SE, while the 50% film has the least, similar to the steady state QY measurements in Section 3.3.2.

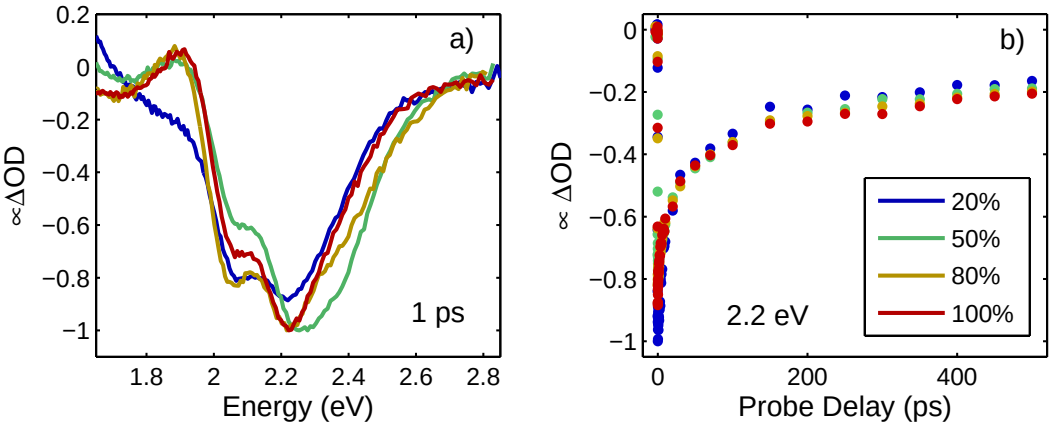

Figure 3.11: Pump-probe results for P3HT thin films with varying % rrP3HT. (a) Normalized pump-probe spectra with pump energy 3.1 eV and delay of 1 ps. (b) Scaled single color traces with pump energy 3.1 eV and probe energy 2.2 eV. Plot colors between panels are consistent.

The GSH comes about due to depopulation of the ground state, and thus has the shape of the absorption spectrum of the domains which are depopulated. That is, at a given delay time only domains that are depopulated will contribute to the GSH. For example, an exciton initially created in a high-energy, amorphous domain which transfers to a low-energy, aggregate domain, would initially give a GSH with the shape of the amorphous ground state absorption spectrum, and, over time, the GSH would shift to the ground state absorption spectrum of the aggregate domain. The GSH gives

the ground state absorption spectrum of the domains the excitons are occupying at a given delay time.

Analysis of the 100% rrP3HT spectrum is presented in Figure 3.12.a. The pump-probe spectrum is the average of the normalized pump-pump probe spectra for nine time delays between 50-500 fs. To ensure no dynamics were lost in this averaging, the normalized spectrum for each of the time delays was analyzed separately and no statistically significant change in the fitting parameters was observed (Figure 3.13.a). The GSH shows structure similar to the absorption spectrum of the annealed rrP3HT film and agrees with theoretical results for the absorption spectrum of P3HT H-aggregates.[94] Because of this agreement, the GSH was modeled with a sum of Gaussians to represent the A_{0-0}, A_{0-1}, A_{0-2}, etc. absorptions. A component consisting of the amorphous absorption spectrum was not necessary to obtain an adequate fit implying that the excitons are exclusively on the aggregated domains.

In Figure 3.12.a the black line shows the ground state absorption spectrum of the film. The GSH overlaps only with the red side of the absorption spectrum representing aggregates, which also indicates that no amorphous domains contribute to the GSH. Fits of the spectrum (Figure 3.12.a, yellow line) consist of a sum of Gaussians to represent the GSH (Figure 3.12.a, dashed red lines) and the film PL spectrum to approximate the SE (Figure 3.12.a, green dashed line). First, the amplitude of the PL was optimized to match the SE. This was then added to the sum of Gaussians to create the total fit. The amplitudes, locations, and width of the Gaussians were then optimized. Because

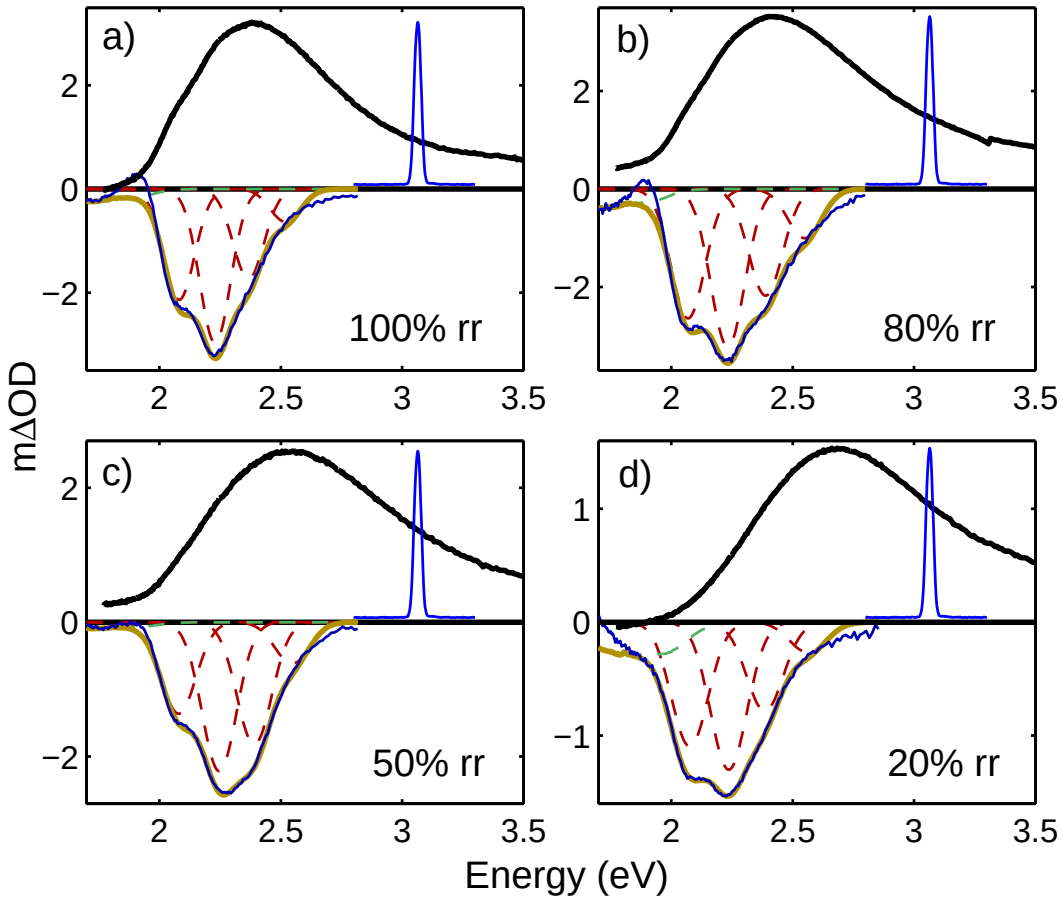

Figure 3.12: Pump-probe analysis of P3HT thin films with varying % rrP3HT: black line shows film absorption spectra, negative blue line shows average pump-probe spectra for 50-500 fs delay time, positive blue line shows pump spectrum, dashed red lines show Gaussian components of fit, dashed green line shows PL component of fit, and yellow line shows overall fit.

the broadening of each absorption feature is assumed to be similar, the Gaussians were all given the same width. The code used to fit this data is given in Appendix A.6.

The fact that the GSH showed no component from the amorphous domains is somewhat surprising, considering that the excitation energy used, 3.1 eV, preferentially creates excitons in the amorphous domains of the films. This is apparent by the spectrum of the pump (Figure 3.12.a, thin blue line) overlapping with the blue side of the absorption spectrum representing the amorphous domains, but not overlapping with the GSH which represents the aggregate domains. Even at 50 fs the GSH showed only aggregate absorption and fitting of the individual time points showed no change in the fitting parameters as a function of time. We conclude that the vast majority of excitons transfer from the amorphous to the aggregate domains in <50 fs.

Similar analysis was carried out for films with 80%, 50%, and 20% rrP3HT as presented in Figure 3.12. Fitting parameters are given in Table 3.3. As with the 100% rrP3HT film, the pump-probe spectra are the average of nine time delays between 50-500 fs. For all films, fitting the time points individually showed no trends with time (Figure 3.13). A structured GSH indicative of excitons residing on aggregate domains is observed by 50 fs even in the 20% film. This means that excitons initially created on the amorphous domains by the pump pulse transfer to the aggregate domains in <50 fs even though there is only ∼8% aggregation in the 20% rrP3HT film in contrast to ∼35% in the fully rrP3HT film. Because there is no further evolution of the GSH with time we see no evidence for exciton transfer after the first 50 fs.

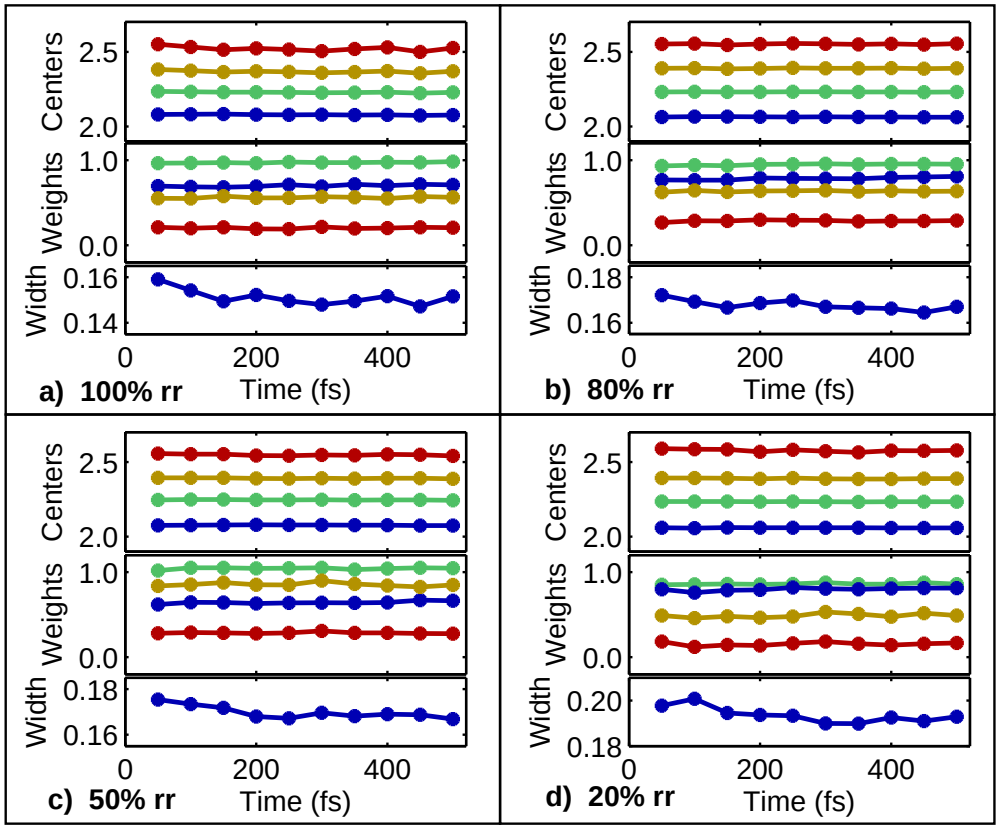

Figure 3.13: Gaussian centers, weights, and widths for GSH fitting as a function of delay time for P3HT thin films with varying % rrP3HT. Colors between centers and weights are consistent. Centers and widths are in eV. Weights are in arbitrary units.

Table 3.3: Fitting parameters for pump-probe analysis of P3HT thin films with varying % rrP3HT. For each film, one global FWHM was fit for all three Gaussians.

	Gaussian	Center (eV)	Weight (a.u.)	FWHM (eV)
100% rrP3HT	1	2.08 ± 0.01	0.29 ± 0.02	0.15 ± 0.01
	2	2.23 ± 0.01	0.40 ± 0.02	
	3	2.37 ± 0.02	0.23 ± 0.02	
	4	2.52 ± 0.02	0.08 ± 0.02	
80% rrP3HT	1	2.07 ± 0.01	0.29 ± 0.02	0.16 ± 0.01
	2	2.23 ± 0.01	0.36 ± 0.02	
	3	2.39 ± 0.01	0.24 ± 0.02	
	4	2.55 ± 0.02	0.11 ± 0.02	
50% rrP3HT	1	2.07 ± 0.01	0.23 ± 0.01	0.17 ± 0.01
	2	2.25 ± 0.01	0.37 ± 0.02	
	3	2.39 ± 0.01	0.30 ± 0.02	
	4	2.55 ± 0.02	0.10 ± 0.02	
20% rrP3HT	1	2.08 ± 0.01	0.32 ± 0.01	0.19 ± 0.01
	2	2.24 ± 0.01	0.38 ± 0.01	
	3	2.39 ± 0.01	0.23 ± 0.02	
	4	2.56 ± 0.02	0.08 ± 0.01	

To verify the measured spectra in Figure 3.12 are from excitons on the aggregate domains, pump-probe experiments were conducted with a pump energy of 2.1 eV. At this energy, the pump directly excites the aggregates as the amorphous rraP3HT film has very little absorption at 2.1 eV. A comparison for the fully rrP3HT film is presented in Figure 3.14. Qualitatively the spectra are very similar, confirming that the GSH measured when pumping at 3.1 eV is due to excitons populating the aggregate domains. We offer two possible explanations for the slight spectral differences in Figure 3.14. First, direct excitation may excite a different population of aggregates than those populated when excitons transfer from amorphous domains. Excitation at 2.1 eV corresponds to the A_{0-0} band which has an amplitude dependent on the excitonic coupling, J, as

described in Section 3.3.3. This excitation preferentially creates excitons in aggregates with low values of J, whereas excitons transferring from the amorphous domains may not have this bias, resulting in a change in the observed vibrational progression. Second, a change in overlapping excited state absorption (ESA) could cause the difference in the spectra. In the visible region, ESA has been attributed to polaron pairs and the formation of polaron pairs is thought to be excitation energy dependent.[97]

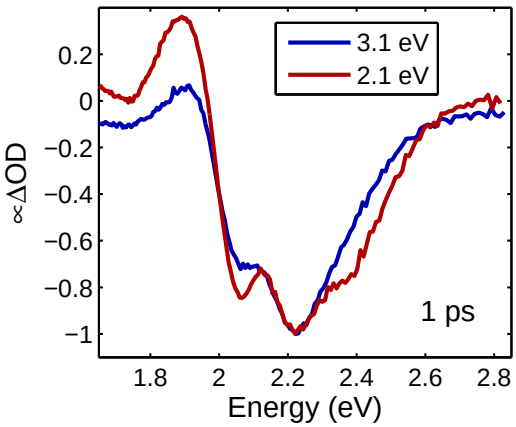

Figure 3.14: Comparison of pump-probe spectra for rrP3HT film with 2.1 eV (red) and 3.1 eV (blue) pump energies.

The surprising sub-50fs transfer from amorphous to aggregated domains could be the result of a variety of mechanisms such as localized excitons diffusing to the aggregate domains, delocalized excitons localizing to the aggregate domains, or long-range energy transfer. Localized excitons traveling down a P3HT chain have a diffusion constant of $D \approx 1\text{x}10^{-3}$ cm^2/s.[17] Using this value as an upper limit for diffusion in the amorphous

regions of the film gives an upper limit on the distance the excitons diffuse in t=50 fs of $L=\sqrt{Dt}\approx$0.1 nm, while the size of domains in rrP3HT thin films are on the order of 20 nm.[99] Thus, diffusion of a localized exciton can not explain the ultrafast transfer from amorphous to aggregate domains even in fully rrP3HT films.

Next, we will look at localization of an initial, delocalized exciton from the amorphous to the aggregate domain. For the molecular weights used in this study (M_n=79k), a single P3HT chain in a rrP3HT film may be part of multiple domains including amorphous and aggregate domains.[100] An initial delocalized exciton may thus sample multiple domains and localize to the lower energy aggregates. While this localization could explain the ultrafast exciton transfer in fully rrP3HT films, extending the reasoning to 20% rrP3HT films which have 4 times less aggregation and, thus, much larger amorphous regions becomes tenuous. Furthermore, rraP3HT molecules present in the 20% rrP3HT films would not incorporate into the aggregate domains, so initial excitons on the rraP3HT molecules would not be able to sample the aggregates. Because of this, we conclude that while the localization of initially delocalized excitons may play a role in the ultrafast transfer of excitons to the aggregates, another mechanism may also be involved.

The final mechanism we will discuss is Förster-like transfer in which electronic coupling results in energy transferring from a donor to an acceptor. In Förster theory the interaction is taken to be bewteen two point dipoles where the characteristic distance of the energy transfer, the Förster radius, is proportional to the donor PL QY as well

as the spectral overlap of the donor PL with the acceptor absorption.[35] For the case of the P3HT films studied here, the donor is a P3HT chromophore in an amorphous domain and the acceptor is a P3HT chromophore in an aggregate domain. Because of the redshifted absorption of the aggregate domains, there is a large spectral overlap between amorphous emission (rraP3HT in Figure 3.2.b) and aggregate absorption (GSH in Figure 3.12). This overlap coupled with the high QY of the amorphous domains could create strong electronic coupling and make energy transfer from the amorphous to the aggregate domains efficient. Conversely, the low QY of the aggregate domains, the small overlap between aggregate emission (rrP3HT in Figure 3.2.b) and aggregate absorption, and the virtually non-existent overlap between the aggregate emission and the amorphous absorption (rraP3HT in Figure 3.2.a) leads to less efficient energy transfer for excitons in the aggregate domains in agreement with the idea of excitons in aggregates being trapped.

Finally, using the amplitudes of the A_{0-0} and A_{0-1} Gaussians from the fits and Equation 3.1, the intramolecular coupling of the aggregate domains the excitons reside on can be calculated for each film. For the 20%, 50%, 80%, and 100% rrP3HT the coupling was found to be $J = 12$, 33, 14, and 23 meV, respectively. Because there could be ESA overlapping the ground state hole these couplings are only approximate, but do agree well with the coupling found for the annealed rrP3HT film as well as couplings found in the literature.[96]

3.4 Conclusions

We have shown that the amount of aggregation in P3HT thin films can be varied by casting films using solutions with different ratios of rrP3HT and rraP3HT. UV-vis and DSC show that as more rrP3HT is used in the films, H-aggregation increases. This allows for the study of excitons as a function of aggregation. Emission in the mixed films is from the aggregated domains even when excitons are preferentially created in the amorphous regions implying excitons transfer from amorphous to aggregate domains before PL can occur. Pump-probe spectroscopy has been used to study the timescale of this exciton transfer event. The pump pulse created excitons on the amorphous domains of the films, but the GSH indicated that the excitons transferred to aggregate domains by 50 fs. This was true for films with as little as 20% rrP3HT and, therefore, a small degree of aggregation. Because no further shape change in the pump-probe spectra was observed, we conclude that excitons transfer to aggregates within 50 fs where they are then trapped as further energy transfer would change the shape of the GSH. One possible explanation for the fast energy transfer from amorphous to aggregate domains is long range Förster-like transfer due to the large spectral overlap between amorphous emission and aggregate absorption. Analysis of the GSH also allowed the approximation of the intermolecular coupling for the mixed films which was inaccessible from the absorption spectra. The values for the intermolecular coupling ranged from 15-33 meV.

Chapter 4

Using a Triblock Copolymer to Model P3HT Aggregation

4.1 Introduction

Conjugated polymers such as poly(3-hexylthiophene) (P3HT) and its derivatives are of interest for use in organic photovoltaic devices due to their large absorption cross section in the solar spectrum and their high hole mobilities[101;102] giving device efficiencies exceeding 10%.[8;67] In Chapter 3 the importance of aggregation in P3HT thin films was investigated and ultrafast exciton localization to aggregates was observed. Because excitons transfer to aggregates quickly, they spend the majority of their lifetime on aggregate domains and, thus, film morphology has a large effect on device efficiency.[76;103] In order to better optimize performance, exciton behavior in aggregates needs to be

better understood. Inherent heterogeneity of conjugated polymer thin films leads to inhomogeneous broadening and makes probing exciton behavior in films difficult. Poor solvents can be added to conjugated polymer solutions to promote aggregation,[77;78] but results have been inconsistent due to solution stability and varying size of aggregates.

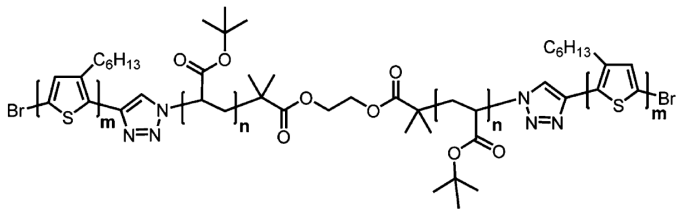

P3HT-*b*-P*t*BA-*b*-P3HT

Figure 4.1: Molecular structure of the triblock copolymer used in this study. The rod-coil-rod copolymer consists of a poly(*tert*-butyl acrylate) chain (the coil segment) with rrP3HT chains attached to each end (the rod segments).

In this chapter, a rod-coil-rod triblock copolymer consisting of the high bandgap polymer poly(*tert*-butyl acrylate) (P*t*BA) with regioregular P3HT (rrP3HT) chains covalently linked to both ends is investigated (Figure 4.1). In a good solvent the triblock behaves as P3HT in solution, while in a poor solvent the triblocks collapse leading to behavior similar to P3HT aggregates. A visible color change is apparent by changing solvents as shown in Figure 4.2. Using this triblock, aggregation can be induced in a stable, reversible, and repeatable manner allowing for spectroscopic studies of excitons on P3HT aggregates.

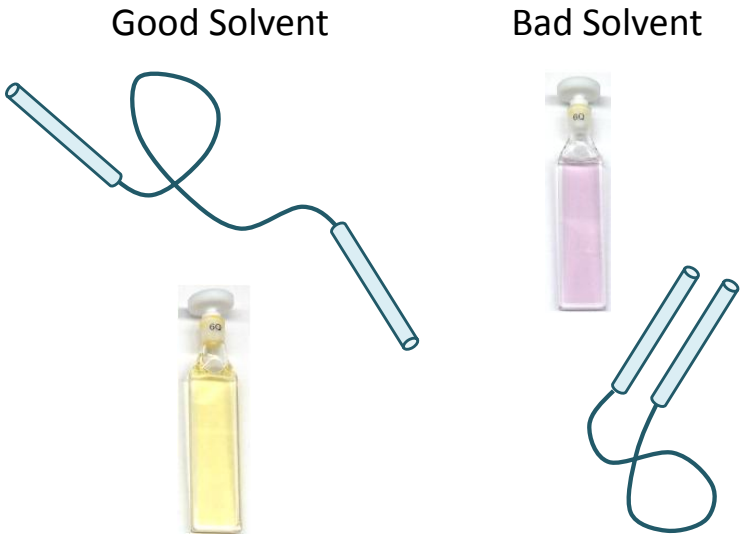

Figure 4.2: Photographs and simplified schematics of triblock in good solvent (toluene) and poor solvent (50/50% methanol/toluene). In the schematics, the cylinders represent the P3HT and the lines represent the PtBA.

4.2 Experimental Section

4.2.1 Sample Preparation

The triblock copolymer was synthesized as previously reported.[104] Solutions of the triblock were prepared in toluene (a good solvent), in 50/50% methanol/toluene (a poor polar solvent), and in 70/30% hexane/toluene (a poor nonpolar solvent). Triblock results are compared to solutions of rrP3HT (Reike Metals, M_n=79k) and regioregular P3HT films prepared as described in Section 3.2.1.

4.2.2 Steady-State Spectroscopy

Absorption and emission spectra were collected using a Cary 14 spectrophotometer and a SPEX Fluorolog 1680, respectively, as described in Chapter 2. Solutions were placed in a 1 mm cuvette for steady state measurements. All PL spectra were collected in front face geometry. Fluorescence quantum yields were determined by comparison to the emission of rrP3HT in solution (Φ_F=0.42).[105]

4.2.3 Pump-Probe Spectroscopy

Pump-probe spectra were obtained using a home-built laser system as described in Chapter 2. Experiments were carried out with pump energies of 2.1 eV, 2.3 eV, and 3.1 eV. A white-light continuum ranging from 1.7 to 2.8 eV was used as the probe pulse. The pump polarization was kept at the magic angle (54.7°) relative to the p-polarized probe pulse to isolate isotropic dynamics. The probe beam was measured for

every laser pulse, while the pump beam was modulated at half the laser repetition rate. By comparing the measured probe beam with and without the pump beam present, the change in optical density, ΔOD, induced by the pump beam was calculated for each pulse pair. For each pump-probe delay, ΔOD values for 15,000 pulse pairs were collected and averaged. This whole process was repeated three times to ensure there was no change in signal due to sample degradation. All three time scans were averaged to give the final ΔOD spectra. Solution samples were continuously pumped through a flow cell, while films were continuously rotated in a box with positive nitrogen pressure to ensure a fresh sample for each laser pulse. Absorption spectra taken before and after laser illumination showed no change due to photobleaching of the sample. Pump pulse energies were between 9-15 nJ.

4.3 Results and Discussion

4.3.1 Inducing Aggregation by Changing Solvents

Absorption and emission spectra for the triblock in toluene (a good solvent) and in 50/50% methanol/toluene (a poor solvent) are shown in Figure 4.3. In the good solvent, the absorption and emission spectra of the triblock match very well with those of a dilute rrP3HT solution. No spectral signatures from the PtBA are observed as expected for a high bandgap material. We conclude that the triblock is extended in the good solvent and that there is very little interaction between the P3HT chains.

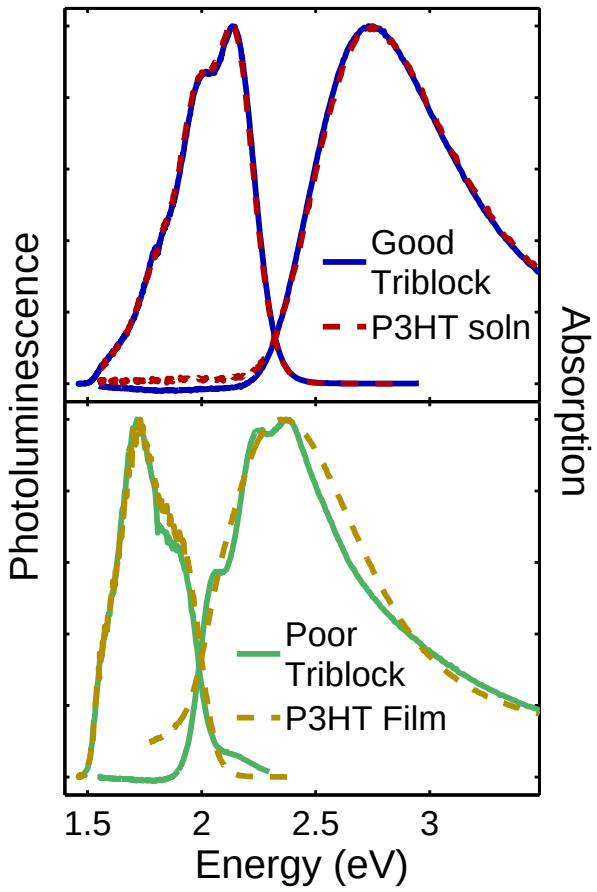

Figure 4.3: Top: Normalized absorption and emission of the triblock in toluene, a good solvent, (solid blue lines) compared to rrP3HT in solution (dashed red lines). Emission excitation was 3.1 eV. Bottom: Normalized absorption and emission of the triblock in 50/50% methanol/toluene, a poor solvent, (solid green lines) compared to a rrP3HT film (dashed yellow lines). Emission excitation was 2.3 eV for the triblock and 3.1 eV for the rrP3HT film.

In the poor solvent the absorption spectrum redshifts and becomes more structured similar to the redshift observed in rrP3HT films (Chapter 3) and P3HT solutions in poor solvents.[106;107;108] These spectral changes have been associated with increased interchain interaction due to the formation of aggregates.[68;69;70] It can similarly be concluded that P3HT aggregates are forming in the triblock sample upon addition of a poor solvent. In comparison to P3HT solutions in poor solvents, the triblock solution is much more stable with absolute absorption showing little change over 10 months.[104] This increased stability is vital for spectroscopic experiments and is attributed to the high solubility of P*t*BA in methanol.[109]

The triblock absorption in poor solvent is similar to that of a rrP3HT film, but more structured. The masking of the structure in films is the result of inhomogeneous broadening which can be reduced by annealing as discussed in Section 3.3.3. The high degree of structure in the triblock is concluded to be from a similar reduction in inhomogeneous broadening. The absorption spectrum can be fit to a series of Gaussians with a shared spectral width to represent the aggregate absorption and a component consisting of the triblock in good solvent to represent any non-aggregated P3HT absorption (Figure 4.4 and Table 4.1). Each Gaussian represents a different vibrational transition in the aggregate as discussed in Section 1.3.1 and by Spano et al.[92;94] The ratio of the A_{0-0} to A_{0-1} peaks was used to estimate the excitonic coupling of the triblock aggregate to be $\sim$30 meV in agreement with values obtained for P3HT films in Chapter 3 and in the literature.[95;96]

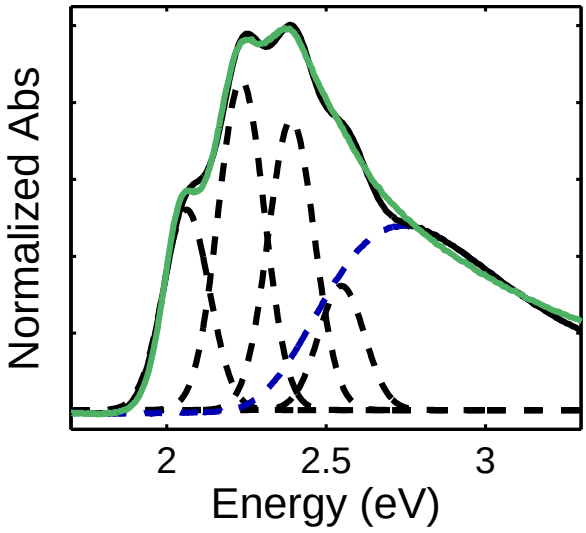

Figure 4.4: Fitting the absorption spectrum (solid green line) of the triblock in 50/50% methanol/toluene, a poor solvent. Total fit (solid black line) is the sum of Gaussian components (dashed black lines) and the absorption spectrum (dashed blue line) of the triblock in toluene, a good solvent.

Table 4.1: Fitting parameters for absorption spectrum of the triblock in 50/50% methanol/toluene, a poor polar solvent. One global FWHM was fit for all four Gaussians.

Gaussian	Center (eV)	Weight (a.u.)	FWHM (eV)
1	2.06 ± 0.01	0.21 ± 0.01	0.17 ± 0.01
2	2.23 ± 0.01	0.35 ± 0.02	
3	2.39 ± 0.01	0.31 ± 0.02	
4	2.55 ± 0.01	0.13 ± 0.02	

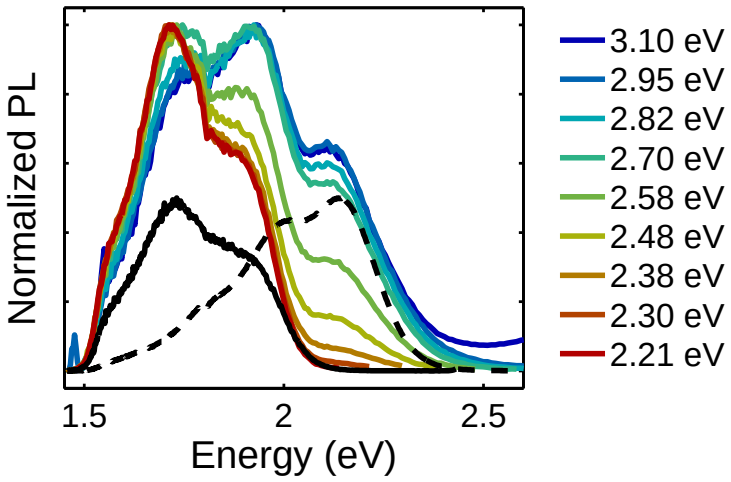

Figure 4.5: Excitation dependent emission spectra of the triblock in 50/50% methanol/toluene, a poor solvent. The black lines show the emission spectra of a P3HT film (solid) and solution (dashed).

The emission of the triblock in poor solvent is shown in Figure 4.3 when excited at 2.3 eV. Excitation of non-aggregated P3HT is minimal at this energy (see top panel of Figure 4.3) and the majority of excitons will be created in P3HT aggregates. The emission of these aggregates is in good agreement with rrP3HT film emission. In films the emission is independent of the excitation energy (Section 3.3.2) as excitons quickly transfer to aggregates before significant emission occurs no matter what domains are excited. This is in stark contrast to the triblock in poor solvent. As shown in Figure 4.5 the emission spectrum of the triblock is highly dependent on the excitation energy. When exciting at higher energies excitons are created on aggregate and non-aggregate P3HT. Emission appears to be a combination of aggregate emission (Figure 4.5, solid

black line) and non-aggregate emission (Figure 4.5, dashed black line). This means that some excitons radiatively decay from non-aggregate P3HT instead of quickly transferring to the aggregate P3HT. This can allow for selective excitation of different types of P3HT to be studied.

4.3.2 Exciton Dynamics

Figure 4.6 shows pump-probe spectra for the triblock in good solvent compared to pump-probe spectra for a solution of rrP3HT. In both cases the excitation energy was 3.1 eV. The spectra are very similar showing a ground state hole (GSH) which overlaps with the absorption spectra, stimulated emission (SE) which overlaps with the fluorescence spectra, and a spectrally-broad excited state absorption (ESA). Initially created singlet excitons can decay to the ground state or undergo intersystem crossing to a long-lived triplet state.[110] Only singlet excitons contribute to SE as the emission cross section of the triplet state is very low. This results in the SE decaying more quickly than the GSH and ESA, giving the apparent growth of the ESA peak at 2.35 eV. Finally, the triblock and P3HT signals decay on similar time scales as shown in Figure 4.7. This data is further evidence that the triblock in good solvent behaves as P3HT in solution.

Figure 4.8 shows pump-probe spectra for the triblock in 50/50% methanol/toluene, a poor polar solvent, when excited at different energies. In all cases there is a prominent GSH that partially overlaps with the absorption spectrum of the triblock. At lower energies ESA dominates giving a positive feature. The shape of the positive feature

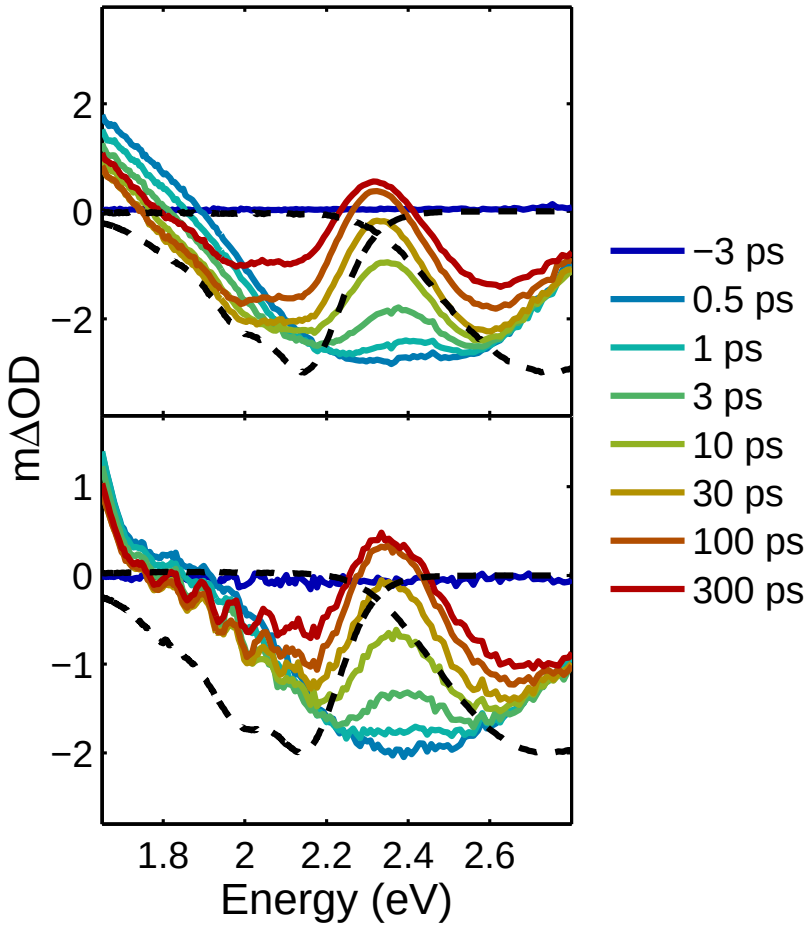

Figure 4.6: Pump-probe spectra for the triblock in a good solvent (top) compared to spectra for a P3HT solution (bottom). Both samples were excited at 3.1 eV. Dashed lines represent emission and absorption spectra for each sample.

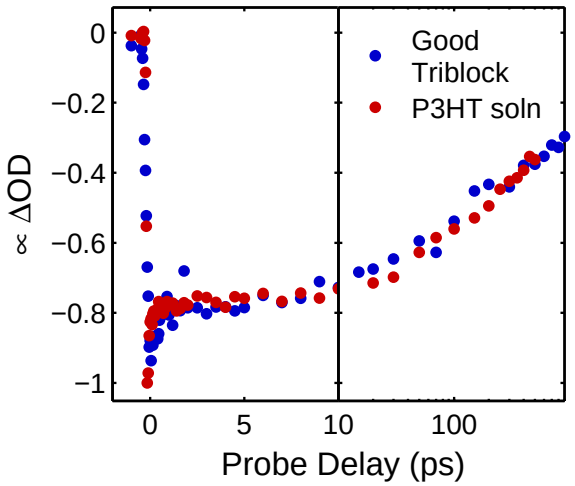

Figure 4.7: Pump-probe single color traces for the triblock in a good solvent (blue) and a P3HT solution (red) at 2.6 eV when excited at 3.1 eV. The time axis is linear to 10 ps and logarithmic after.

appears to be dependent on excitation energy, but this change in shape may be due to overlapping SE. Because the PL of the triblock in poor solvent is dependent on excitation energy (Figure 4.5 and solid black lines in Figure 4.8), the shape of SE is expected to change with excitation energy. The structure present in the positive feature resembles the PL spectrum of the triblock resulting in the peak at ∼1.9 eV when exciting at lower energies.

The GSH is also dependent on the excitation energy. When excited at 3.1 eV there appears to be less structure in the GSH compared to lower energy excitation. This is in agreement with steady state PL results showing emission from both aggregate and non-aggregate P3HT when the triblock is excited at 3.1 eV. There is no appreciable

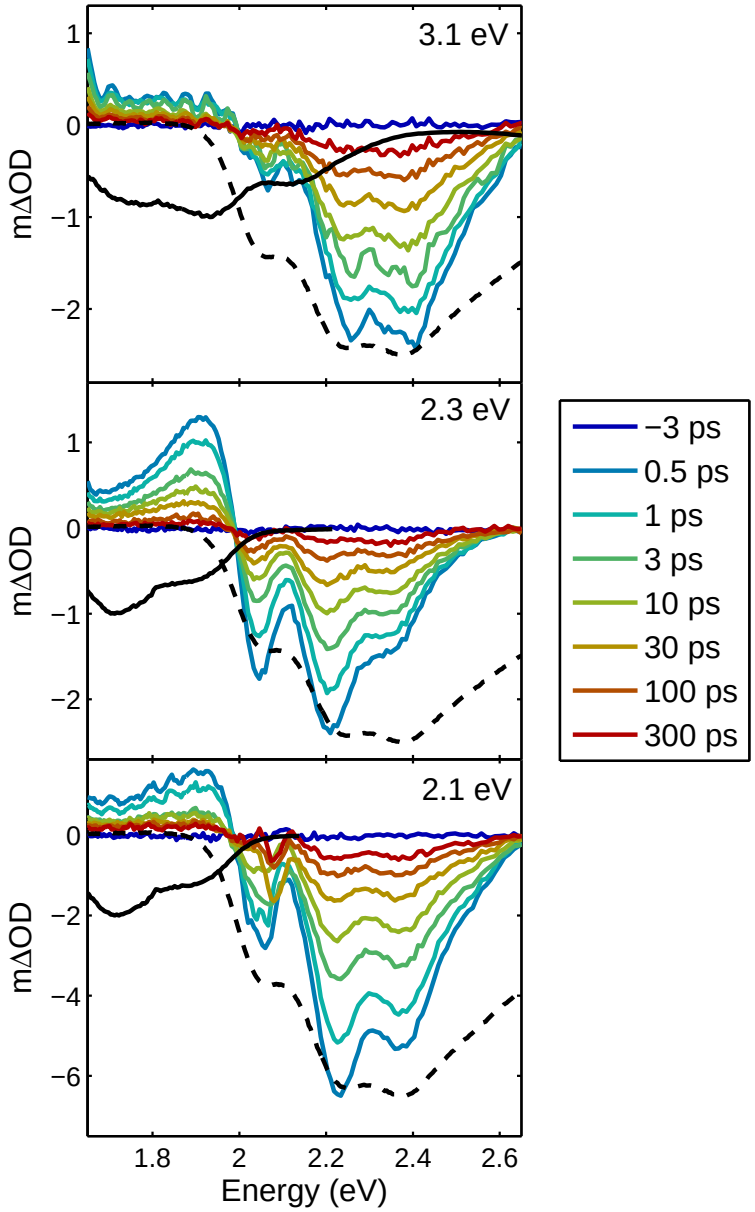

Figure 4.8: Pump-probe spectra for the triblock in a poor polar solvent pumped at 3.1 eV (top), 2.3 eV (middle), and 2.1 eV (bottom). Solid black lines show steady state emission spectra at each excitation energy, while dashed black lines show the absorption spectrum.

evolution of the pump-probe spectrum when exciting at 3.1 eV as shown in Figure 4.9. We conclude that higher energy excitation results in excitons initially created on aggregated and non-aggregated P3HT. Some excitons may transfer within the instrument response (∼100 fs) similar to observations in rrP3HT films (Chapter 3), but other excitons are trapped on the non-aggregate P3HT resulting in the higher energy PL and less structured GSH.

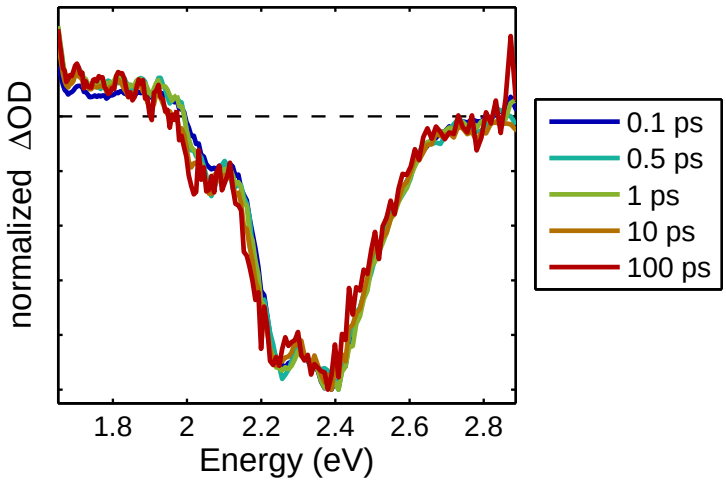

Figure 4.9: Normalized pump-probe spectra for the triblock in a poor polar solvent excited at 3.1 eV.

When exciting at lower energies (2.1 and 2.3 eV) a more structured ground state hole is observed signifying the majority of excitons are on aggregated P3HT. Triblock PL, when excited at these energies, matched rrP3HT emission which is predominantly from aggregates.[94] It is concluded that aggregates are directly excited at these energies and, because the spectral shapes do not evolve over time, the excitons remain on aggregates

throughout their lifetime.

The vibrational progression of the GSH appears to be different for excitation at 2.1 and 2.3 eV. Initially, the spectra were fit to a series of Gaussians representing the different transitions in the aggregate absorption spectrum as shown in Figure 4.10.[92] Two models were applied to fit the data with the fitting parameters shown in Table 4.2. In Model 1 the fitting parameters were a shared Gaussian width, the center of the 0-0 energy transition (E_{0-0}), the energy spacing between the Gaussians (ΔE), and the amplitudes of the Gaussians (A_{0-0}, A_{0-1}, etc.). This model was not able to adequately fit the data due to apparent non-uniform spacing between the vibrational transitions. This non-uniformity in the vibrational progression is a signature of H-aggregation where the energetic spacing between the 0-0 and 0-1 peaks dilates.[111] To account for this, the fitting parameters in Model 2 were a shared Gaussian width, the center of the 0-0 energy transition (E_{0-0}), the center of the 0-1 energy transition (E_{0-1}), the spacing between subsequent transitions (ΔE), and the amplitudes of the Gaussians. Model 2 gave more adequate fits, although the uncertainty in the amplitude of the 0-0 transition is high due to overlap with the ESA. Due to this uncertainty, it was not possible to calculate the exciton coupling, J, using the ratio of the 0-0 and 0-1 amplitudes as in Chapter 3.

In order to find J the GSH was refit using a modified Franck-Condon model which

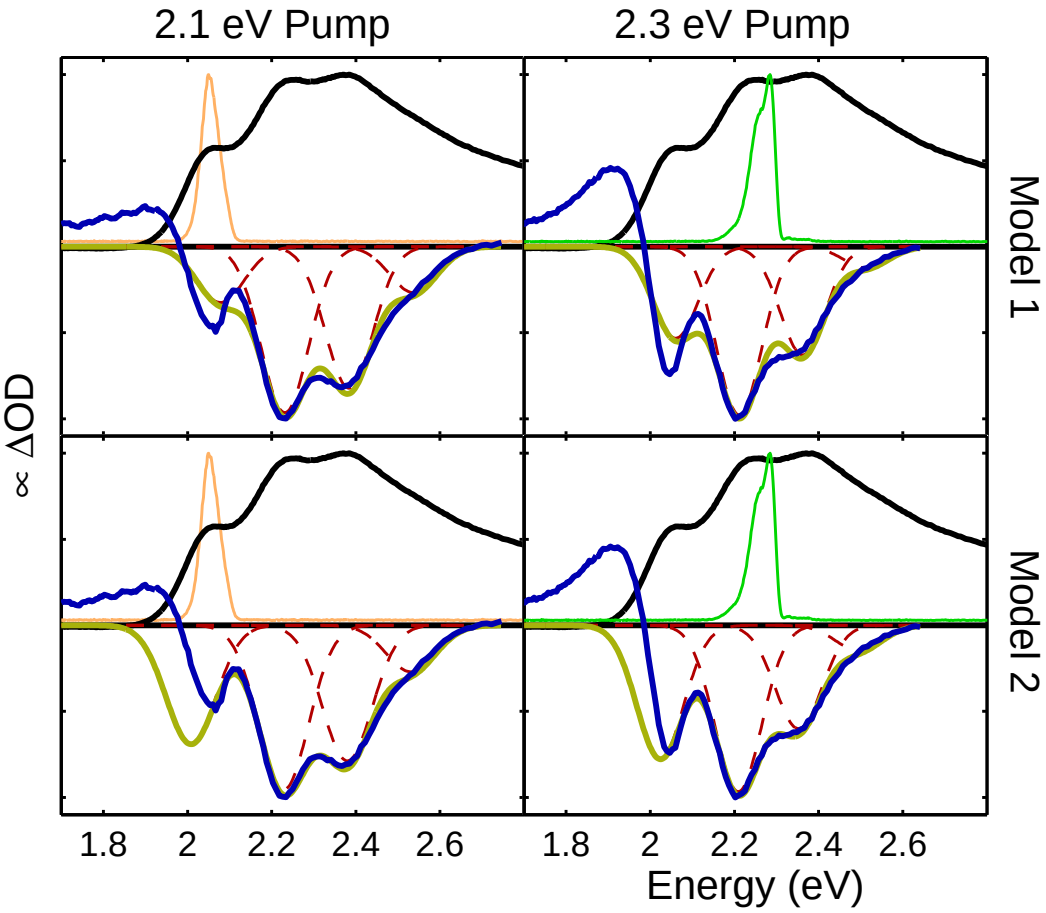

Figure 4.10: Analysis of pump-probe spectra for the triblock in a poor polar solvent excited at 2.1 eV (left plots) and 2.3 eV (right plots). Two different models (Model 1: top, Model 2: bottom) are presented as discussed in the text. Black lines show absorption spectrum of the triblock; orange and green lines show the spectra for the 2.1 and 2.3 eV excitation pulses, respectively; red dashed lines represent the individual Gaussian components of the fit; yellow lines show the overall fit to the data; and the blue lines are the average of the pump-probe spectra from 50-500 fs.

Table 4.2: Fitting parameters for ground state hole of the triblock in 50/50% methanol/toluene, a poor polar solvent, using Models 1 and 2. Energies are in eV and amplitudes are in arbitrary units. Uncertainties are the 95% confidence intervals returned by the fitting routine.

Pump	2.1 eV	2.1 eV	2.3 eV	2.3 eV
Model	1	2	1	2
E_{0-0}	2.08 ± 0.01	2.01 ± 0.02	2.06 ± 0.01	2.02 ± 0.02
E_{0-1}	–	2.23 ± 0.02	–	2.21 ± 0.01
ΔE	0.15 ± 0.01	0.15 ± 0.01	0.15 ± 0.01	0.14 ± 0.01
FWHM	0.13 ± 0.01	0.14 ± 0.01	0.13 ± 0.01	0.13 ± 0.01
A_{0-0}	0.14 ± 0.03	0.26 ± 0.08	0.24 ± 0.03	0.31 ± 0.07
A_{0-1}	0.41 ± 0.03	0.35 ± 0.02	0.43 ± 0.03	0.39 ± 0.02
A_{0-2}	0.35 ± 0.03	0.29 ± 0.02	0.28 ± 0.03	0.24 ± 0.02
A_{0-3}	0.11 ± 0.02	0.10 ± 0.01	0.05 ± 0.02	0.05 ± 0.01

accounts for aggregation of the sample.[111;112] The amplitude of the 0-n transition is

$$A_{0-n} = \frac{\lambda^{2n} e^{-\lambda^2}}{n!} \left[1 - \frac{2J}{\omega_0} e^{-\lambda^2} \sum_{\substack{m \geq 0 \\ m \neq n}} \frac{\lambda^{2m}}{m!(m-n)} \right]^2 \tag{4.1}$$

where λ^2 is the Huang-Rhys factor and ω_0 is the energy of the vibration coupled to the electronic transition taken to be the energy of the vinyl stretch (0.18 eV). The term in the square brackets is the correction due to aggregation and the factor of 2 in the $2J/\omega_0$ is necessary for large π-stacks where the majority of chains interact with two neighbors (one on each side).[112] For a dimer, there is only one nearest neighbor interaction and the factor of 2 should be omitted. Using equation 4.1 to find the amplitudes (referred to as Model 3) provided an adequate fit with one less fitting parameter than Model 2 as shown in Figure 4.11. Fitting parameters included a shared Gaussian width, E_{0-0}, E_{0-1}, and ΔE as in Model 2. Fitting parameters controlling the amplitudes were λ^2,

J, and an overall scaling factor, A. The optimized fitting parameters are given in Table 4.3.

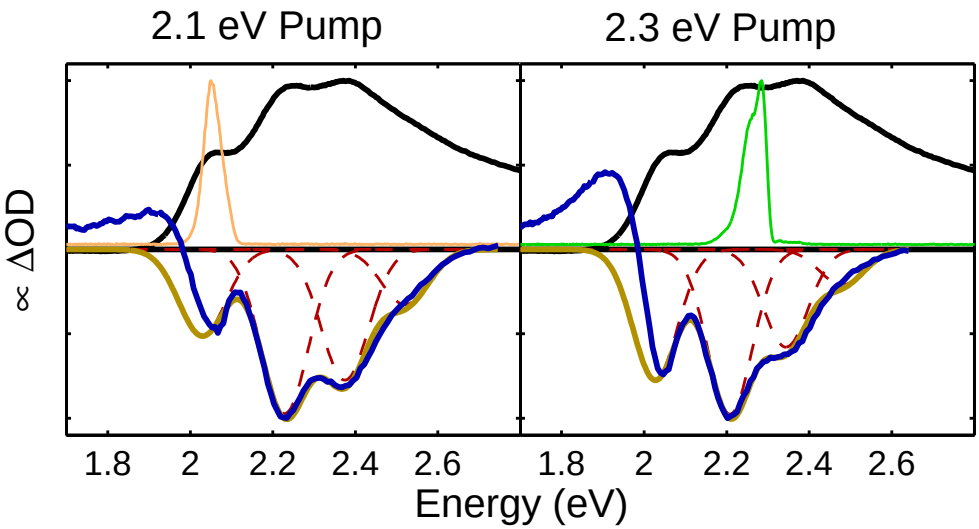

Figure 4.11: Analysis of pump-probe spectra for the triblock in a poor polar solvent excited at 2.1 (left) and 2.3 eV (right) using Model 3 as discussed in the text. Black lines show absorption spectrum of the triblock; orange and green lines show the spectra for the 2.1 and 2.3 eV excitation pulses, respectively; red dashed lines represent the individual Gaussian components of the fit; yellow lines show the overall fit to the data; and the blue lines are the average of the pump-probe spectra from 50-500 fs.

The Huang-Rhys factors found by the fitting procedure are in close agreement with previous studies on P3HT[94], while the values for the exciton coupling are similar to those for rrP3HT films found in Chapter 3. Furthermore, different pump energies preferentially excite P3HT aggregates with a certain exciton coupling, J. Pumping at 2.1 eV excites aggregates with a higher coupling compared to pumping at 2.3 eV. Future experiments using two-dimensional electronic spectroscopy will examine the dependence

Table 4.3: Fitting parameters for ground state hole of the triblock in 50/50% methanol/toluene, a poor polar solvent using Model 3. The reported J values assume large aggregates (the factor of 2 in Equation 4.1 is present). Uncertainties are the 95% confidence intervals returned by the fitting routine.

Pump	2.1 eV	2.3 eV
E_{0-0} (eV)	2.03 ± 0.02	2.03 ± 0.02
E_{0-1} (eV)	2.23 ± 0.01	2.21 ± 0.01
ΔE (eV)	0.15 ± 0.01	0.14 ± 0.01
FWHM (eV)	0.13 ± 0.01	0.13 ± 0.01
A (a.u.)	2.6 ± 0.2	2.6 ± 0.2
λ^2	1.2 ± 0.1	1.1 ± 0.1
J (meV)	34 ± 11	15 ± 10

of exciton coupling on pump energy giving further insight into how excitons evolve in P3HT aggregates.

4.3.3 Solvent Polarity

By changing the solvent used to foster aggregation, the polarity of the aggregate's surroundings can be controlled which is not possible for thin film samples. This can help to determine the nature of the exciton. Figure 4.12 shows the absorption spectra for the triblock in a poor polar solvent (50/50% methanol/toluene) and a poor nonpolar solvent (70/30% hexane/toluene). Both show a structured, redshifted absorption indicative of aggregation, but the vibrational progression is different. The coupling, J, in the polar solvent was determined to be ∼30 meV in Section 4.3.1. Similar fitting gives a coupling of ∼20 meV in the nonpolar solvent (Figure 4.12, Table 4.4).

The emission spectra for the triblock in polar and nonpolar solvents are shown in Figure 4.13. The fluorescence quantum yield (QY) is suppressed in the polar solvent

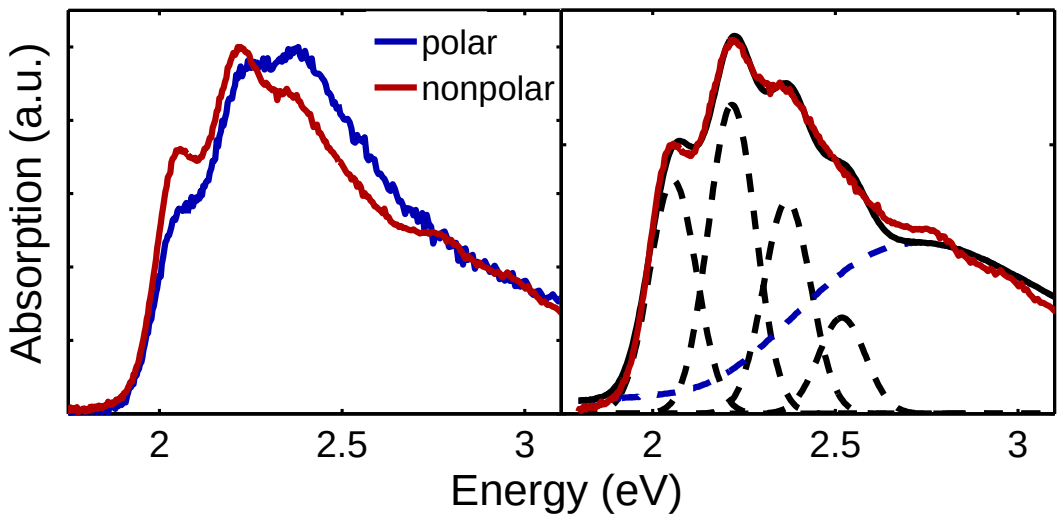

Figure 4.12: Top: Absorption spectra for the triblock in 50/50% methanol/toluene (a poor polar solvent) and in 70/30% hexane/toluene (a poor nonpolar solvent). Bottom: Fit of the absorption spectrum (red line) of the triblock in 70/30% hexane/toluene. Total fit (solid black line) is the sum of Gaussians components (dashed black lines) and the absorption spectrum (dashed blue line) of the triblock in toluene, a good solvent.

Table 4.4: Fitting parameters for absorption spectrum of the triblock in 70/30% hexane/toluene, a poor nonpolar solvent. One global FWHM was fit for all four Gaussians.

Gaussian	Center (eV)	Weight (a.u.)	FWHM (eV)
1	2.05 ± 0.01	0.27 ± 0.01	0.15 ± 0.01
2	2.22 ± 0.01	0.36 ± 0.01	
3	2.37 ± 0.01	0.25 ± 0.01	
4	2.52 ± 0.01	0.11 ± 0.01	

by a factor of 10 when compared to the emission in the nonpolar solvent. The lower quantum yield could be due to the polar solvent stabilizing non-emissive charge-transfer states or due to a change in the exciton coupling, J, which plays a large role on the emission efficiency of aggregates.[92;104] Analysis of the absorption spectra show that J is smaller in the nonpolar solvent which could account for the emission quenching, but this does not rule out that stabilization of a charge-transfer state also plays a role.

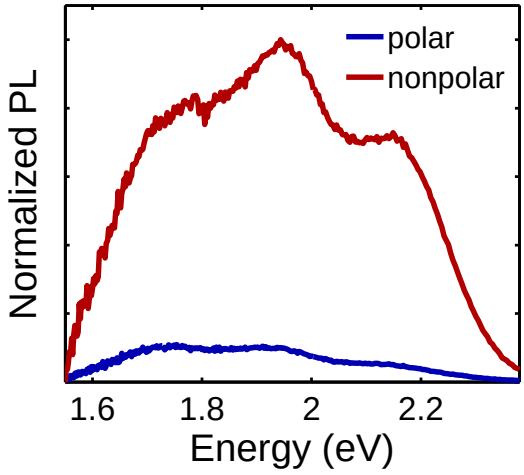

Figure 4.13: Emission spectra for the triblock in 50/50% methanol/toluene (a poor polar solvent) and in 70/30% hexane/toluene (a poor nonpolar solvent). The spectra are normalized to their fluorescence quantum yields.

To help determine the source of the emission quenching, pump-probe spectroscopy was employed. Pump-probe spectra for the triblock in nonpolar solvent are shown in Figure 4.14. The spectra have similar features to pump-probe results for the polar solvent (Figure 4.8) with a different vibrational progression. The amplitude of the 0-0

transition is similar to the amplitude of the 0-1 transition indicating a small exciton coupling, J, assuming a Huang-Rhys factor on the order of 1.[92] This was confirmed by fitting with Model 3, giving $J = 24 \pm 3$ meV (Figure 4.15 and Table 4.5). The change in Huang-Rhys factor of the triblock between solvents is attributed to a change in molecule conformation.[113;114]

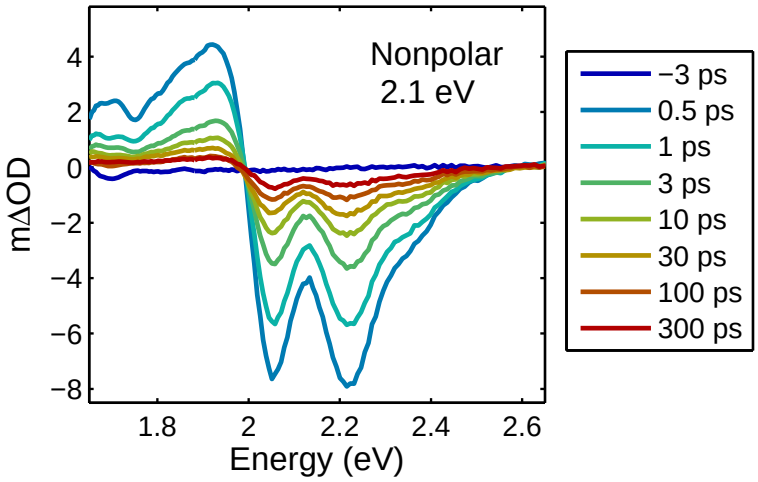

Figure 4.14: Pump-probe spectra for the triblock in a poor nonpolar solvent pumped at 2.1 eV.

Figure 4.16 shows pump-probe single-color traces for the aggregated triblock in polar and nonpolar solvents. The traces were taken from the GSH at 2.2 eV. The dynamics were fit to a sum of exponential decays and the fitting parameters were in close agreement as shown in Table 4.6. If the polar solvent was stabilizing a charge-transfer state an increased lifetime is expected. We see no evidence of a change in the exciton lifetime due to changing solvents and, therefore, conclude that the excitons

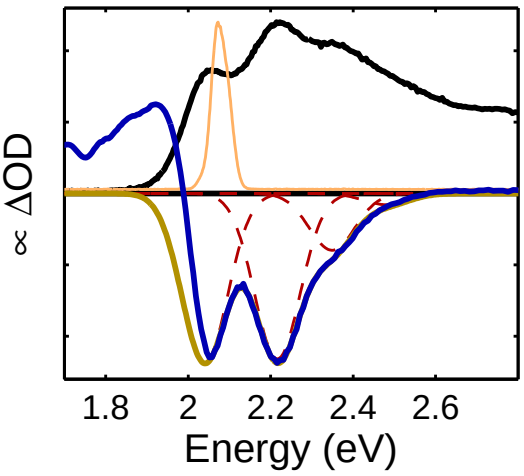

Figure 4.15: Analysis of pump-probe spectra for the triblock in a poor nonpolar solvent excited at 2.1 eV using Model 3 as discussed in the text. The black line shows absorption spectrum of the triblock; the orange line shows the spectrum for the 2.1 eV excitation pulse; red dashed lines represent the individual Gaussian components of the fit; the yellow line shows the overall fit to the data; and the blue line is the average of the pump-probe spectra from 50-500 fs.

Table 4.5: Fitting parameters for GSH of the triblock in 70/30% hexane/toluene, a poor nonpolar solvent using Model 3. The reported J values assume large aggregates (the factor of 2 in Equation 4.1 is present). Uncertainties are the 95% confidence intervals returned by the fitting routine.

Pump	2.1 eV
E_{0-0} (eV)	2.04 ± 0.01
E_{0-1} (eV)	2.21 ± 0.01
ΔE (eV)	0.13 ± 0.01
FWHM (eV)	0.13 ± 0.01
A (a.u.)	2.8 ± 0.1
λ^2	0.6 ± 0.1
J (meV)	24 ± 3

have little charge-transfer character. The quenching of emission in the polar solvent is attributed to a change in exciton coupling.

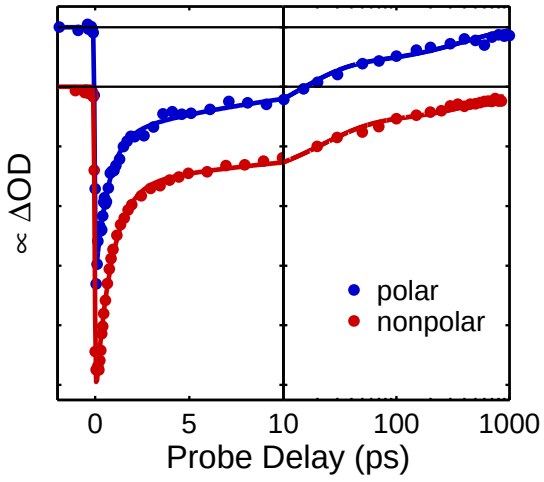

Figure 4.16: Pump-probe single color traces for the triblock in a poor polar solvent (blue) and a poor nonpolar solvent (red) at 2.2 eV when excited at 2.1 eV. Traces have been translated for clarity. Horizontal black lines show the baseline for each trace. The time axis is linear to 10 ps and logarithmic after.

Table 4.6: Fitting parameters for GSH recovery of the triblock in poor solvents.

Solvent	A_1 (%)	τ_1 (ps)	A_2 (%)	τ_2 (ps)	A_3 (%)	τ_3 (ps)
polar	58 ± 2	0.8 ± 0.1	29 ± 1	19 ± 4	13 ± 1	600 ± 130
nonpolar	65 ± 2	0.7 ± 0.1	22 ± 1	16 ± 3	13 ± 1	600 ± 80

4.4 Conclusions

The triblock copolymer presented has been used to mimic aggregation in P3HT. Steady-state and ultrafast spectroscopy confirm that the triblock performs as P3HT in solution

when in a good solvent. Upon addition of a poor solvent the absorption spectrum red-shifts and becomes more structured indicating aggregation. Pump-probe spectroscopy confirmed the presence of aggregates. Unlike in films, excitation at different pump energies resulted in different pump-probe results. At high energies, which preferentially excite non-aggregated P3HT, little structure was observed in the GSH signifying excitons do not undergo ultrafast transfer to aggregates as in rrP3HT films. At energies which excite the aggregates we see differences in the GSH indicative of aggregates with different exciton couplings. Future two-dimensional electronic spectroscopy experiments will investigate interactions between aggregates and the influence of pump energy on exciton behavior.

Aggregation was induced using polar and nonpolar solvents. This allowed for the study of aggregates as a function of the environment polarity. Emission quenching was observed for polar solvents. An associated change in the exciton coupling was measured in the absorption and pump-probe spectra, although a change in exciton lifetime was not observed. Because the same lifetime was observed for both solvents, the emission quenching is unlikely to be caused by a stabilized charge-transfer exciton in the polar solvent. Instead, we attribute the loss of emission to increased exciton coupling in the polar solvent and conclude that excitons in P3HT aggregates have little charge-transfer character.

Chapter 5

Excited State Dynamics in CZTS Nanocrystals

5.1 Introduction

Currently, thin film solar cell technology is dominated by $CuIn_xGa_{(1-x)}Se_2$ (CIGS) and CdTe[11] due to their high efficiencies (20.4% and 19.6%, respectively)[8] and low production costs, yet the lack of available indium and tellurium may limit overall capacity of CIGS and CdTe.[115] One alternative material composed exclusively of earth-abundant elements is Cu_2ZnSnS_4 (CZTS), and photovoltaic devices made from CZTS thin films

and nanocrystals (NCs) have begun to emerge. In fact, power conversion efficiencies as high as 11% have been reported.[116] Naturally, the excited state dynamics in CZTS NCs are of interest because of their current use in device construction.[117;118;119;120;121] A better understanding of the photophysics and excited state dynamics will assist in further optimization.

So far, time-resolved Photoluminescence has primarily been used to study the excited state dynamics, giving PL lifetimes on the order of 10 ns.[116;122] Photoluminescence (PL) from S-poor single crystals of CZTS is orders of magnitude higher than that from stoichiometric single crystals and, for this reason, PL in CZTS has been attributed to non-stoichiometric domains.[123] Consequently, in time-resolved PL studies on devices, domains with differing stoichiometry contribute different lifetimes, which complicates analysis and alters observed lifetimes. In contrast, optically clear solutions of size controlled CZTS NCs provide a homogeneous platform for time resolved spectroscopic studies of excited states in stoichiometric CZTS. However, due to large surface-area-to-volume ratios, surface effects can have a larger impact on excited state dynamics in NCs than in bulk systems. In this chapter we discuss measurements of the ultrafast dynamics of the majority-component, non-emissive excited states in CZTS NCs with sizes that span the onset of quantum confinement.

5.2 Experimental Section

5.2.1 Sample Preparation

CZTS NCs were synthesized and characterized as described elsewhere in detail.[120] Briefly, NCs were synthesized from metal diethyldithiocarbamate complexes that thermally decompose into their corresponding sulfides at different temperatures. The presence of oleylamine lowers the decomposition temperature of the complexes, enabling the formation of phase-pure CZTS NCs. The complexes were stoichiometrically mixed and held at a temperature below the lowest natural decomposition temperature but above the highest decomposition temperature in the presence of oleylamine. When the oleylamine was added, all complexes decomposed simultaneously leading to nucleation and NC growth. The size of NCs was controlled by varying the temperature and the amount of oleylamine added. Two samples were synthesized with average diameters of 2 nm and 5 nm as measured by Scherrer analysis of x-ray diffraction peaks (Figure 5.2 inset). The stoichiometry of the NCs was confirmed using energy dispersive x-ray spectroscopy. As-synthesized NCs were capped with oleylamine and oleic acid ligands. After synthesis NCs were dispersed in toluene with excess oleic acid, which ensures adequate oleate coverage on the surface to improve the stability of NC dispersions.

5.2.2 Spectroscopic Studies

Ultrafast pump-probe spectra were collected using a home-built laser system described in detail in Chapter 2, which produced pulses with 80 fs (FWHM) pulse widths at a repetition rate of 1 kHz. The pump beam had an energy of 3.1 eV and a waist of 100 µm (FWHM), while the probe was a white light continuum that extended from 1.5 to 2.7 eV. The pump polarization was kept at the magic angle (54.7 degree) relative to the probe to isolate isotropic excited state dynamics.

The probe spectrum was measured for every laser pulse, the pump was modulated at half the laser repetition rate, and the change in optical density induced by the pump, ΔOD, was collected for every pulse pair. Reported ΔODs were averaged over at least 250,000 pulse pairs at each value of pump-probe time delay. Dependence of the ΔOD signal on the pump power was measured, and the response was found to be linear for pulse energies between 60 and 600 nJ as shown in Figure 5.1. No change in spectral shape or dynamics were found in this pulse energy range. All data analyzed was taken with pulse energies between 110-125 nJ. CZTS NC dispersions with optical densities of 0.25 at the pump energy were continuously pumped through a 1 mm flow cell during data collection to ensure a fresh sample for each laser pulse. Absorption spectra measured on a Cary 14 spectrophotometer before and after laser exposure demonstrated no change due to photobleaching of the sample. Full-frequency data were corrected for temporal dispersion in the probe as described previously.[66]

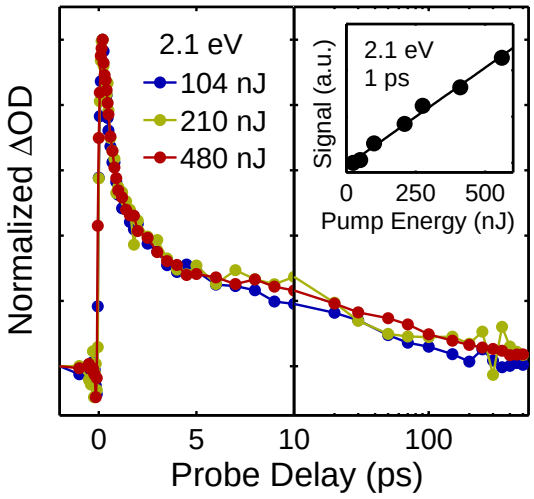

Figure 5.1: Normalized single-color traces for a CZTS NC sample at three different pump powers when probing at 2.1 eV. Inset: Pump-probe signal as a function of pump power when probing at 2.1 eV with a pump-probe delay time of 1 ps.

5.3 Results and Discussion

5.3.1 Quantum Confinement

Figure 5.2 shows the absorption spectra of 2 nm and 5 nm diameter CZTS NCs dispersed in toluene. The absorption spectrum of the 2 nm NCs is shifted to higher energy and has an added feature at ∼2.0 eV as compared to the 5 nm NC absorption spectrum. The results are consistent with previously reported absorption spectra and the reported Bohr radius for CZTS NCs of 2.5-3.3 nm.[120] This indicates that the 2 nm NCs are quantum confined and are subsequently referred to as quantum dots (QDs). No photoluminescence was observed between 1.2-3.1 eV when exciting at 3.1 eV, placing an upper limit on the PL quantum yield in this region of 0.001. This result is in agreement

with PL studies on stoichiometric CZTS single crystals.[123]

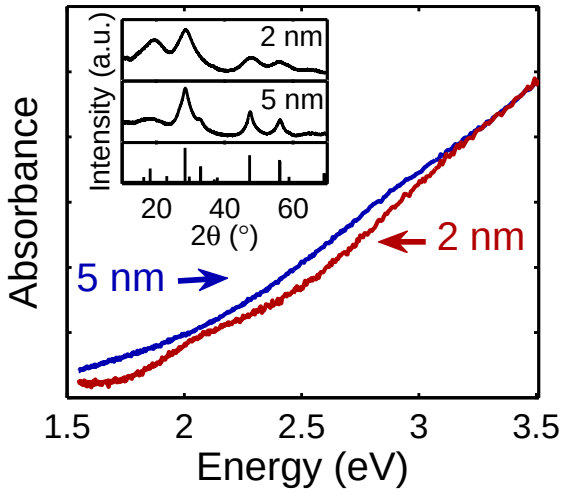

Figure 5.2: Room temperature absorption spectra for 5 nm and 2 nm CZTS NCs in toluene with oleic acid. Inset: X-ray diffraction from 2 nm (top panel) and 5 nm (middle panel) CZTS NCs. The reference pattern for CZTS Kesterite structure is shown in the bottom panel (ICDD-ref 04-005-0388).

5.3.2 Dilation of Density of States upon Confinement

Pump-probe spectra for the 2 nm QDs and 5 nm NCs are shown as a function of time delay in Figure 5.3. Pump-probe spectra are the sum of electron excited state absorption (ESA) and a ground state hole (GSH). Electron ESA is an added absorption resulting in a positive contribution to the total spectra, while the GSH is a loss of ground state absorption resulting in a negative contribution shaped like the steady state absorption spectra of the excited species (Figure 5.2). Because the ΔOD is positive at all energies in our spectra, the electron ESA dominates throughout the energy range probed. The

maxima in the 2 nm QD and 5 nm NC pump-probe spectra at ∼2.4 eV and ∼2.2 eV, respectively, and the subsequent decrease in ΔOD at higher probe energies is due to the GSH contribution. At higher energies, the ground state absorption is stronger, which increases the influence of the GSH and causes a decrease in the total ΔOD. There was no evidence for contributions from stimulated emission, consistent with the absence of measurable PL.

In the 2 nm QDs, two ESA features were observed with a gap between them at 2.0 eV (Figure 5.3). This gap was in agreement with the theoretical density of states (DOS) in which the conduction band consists of two separated bands.[124;125;126] Hereafter these low and high energy conduction bands are referred to as the first and second conduction bands, respectively. The predicted bimodal DOS is illustrated schematically by the light blue line in Figure 5.4. The low energy feature in Figure 5.3 was assigned to intraband electron ESA in the first conduction band (Figure 5.4, red arrow), and the high energy feature was assigned to interband electron ESA from the first conduction band to the second conduction band (Figure 5.4, green arrow). The gap at 2 eV reflected the decrease in density of states between these conduction bands. The pump energy (3.1 eV) was insufficient to directly access the second conduction band from the valence band states.

The 5 nm NC spectra (Figure 5.3) shows similar ESA features, but the gap between the ESA features is shifted from 2.0 eV to 1.7 eV. The gap shifting to lower energy in the 5 nm NCs is consistent with separation of the energy states due to quantum confinement in the 2 nm QDs. Confinement increases the bandgap and dilates the DOS in energy. In

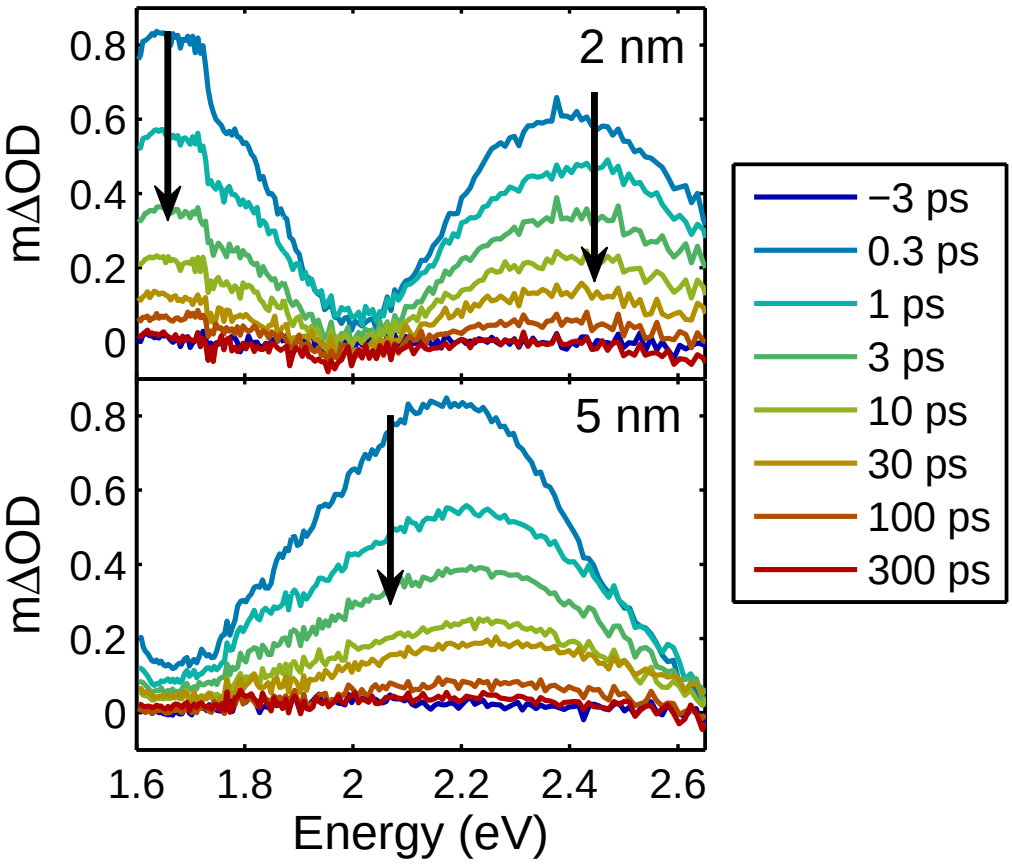

Figure 5.3: Pump-probe spectra for oleate covered 2 nm CZTS QDs (top) and 5 nm CZTS NCs (bottom) dispersed in toluene.

the 2 nm QDs, the first and second conduction bands shift and separate when compared to the 5 nm NCs causing the associated shifts in the pump-probe spectra. We note that the bimodal structure in the DOS is not observable in the ground state absorption spectrum, Figure 5.2, due to the dense valence band.[125]

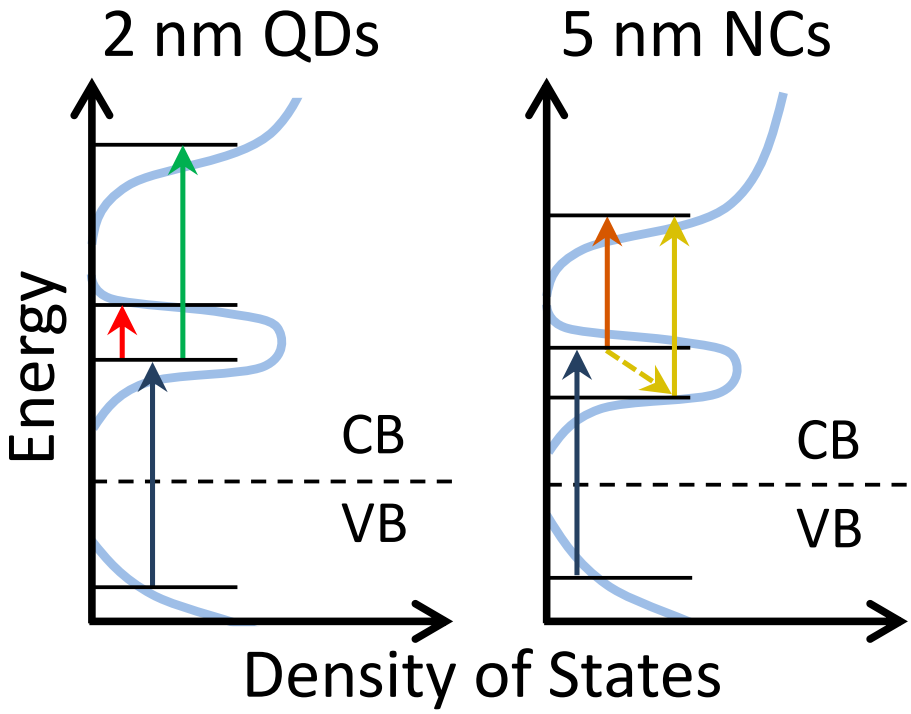

Figure 5.4: Schematic representation of the density of states[124;126] (light blue curves) and energy transitions (arrows) for 2 nm QDs and 5 nm NCs. Dashed black lines are approximate Fermi levels; CB denotes conduction band; VB denotes valence band. Blue arrows denote pump pulse excitation. In the diagram for 2 nm QDs: Red arrow denotes intraband ESA; green arrow denotes interband ESA. In the diagram for 5 nm NCs: Orange arrow denotes short time interband ESA; dashed yellow arrow denotes electron cooling; yellow arrow denotes late time (higher energy) interband ESA. Energy axis not to scale.

5.3.3 Excited State Dynamics

In the 5 nm NCs, the high energy feature in the pump-probe spectra blueshifts with increasing pump-probe delay time. We associate this shift with electrons cooling in the first conduction band. Photoexcitation results in some electrons initially populating states high in the first conduction band. With time, the electrons cool toward the conduction band edge where more energy is required to excite them to the second band as depicted in Figure 5.4. This cooling manifests in the spectra as a blueshift in the peak of the interband transition. Figure 5.5 shows the interband peak energy as a function of time. The shift for the 5 nm NCs was fitted to an exponential rise with a time constant of 1.1±0.3 ps. In other semiconductor NCs, cooling time scales on this order have been attributed to an Auger mechanism where excess electron energy is transferred to the hole, where it is then dissipated by scattering from phonons.[127] While this cooling time is a factor of ∼2 greater than that for CdTe[128] and CdSe[129] NCs, it is still much shorter than the time scale associated with hot electron transfer, which occurs on a 10 ps time scale.[127] There was no measurable peak shift for the 2 nm QD sample. This reflects the fact that the electrons in the 2 nm QDs are excited closer to the conduction band edge as a result of the wider bandgap (Figure 5.4). Consequently, the influence of intraband electron cooling on spectral diffusion is reduced.

Time dependence of the interband electron ESA features were fitted to a sum of two exponential decays subsequently convoluted over the instrument response (Figure 5.6). Spectral energy ranges for the fitting, time constants, and amplitudes for each

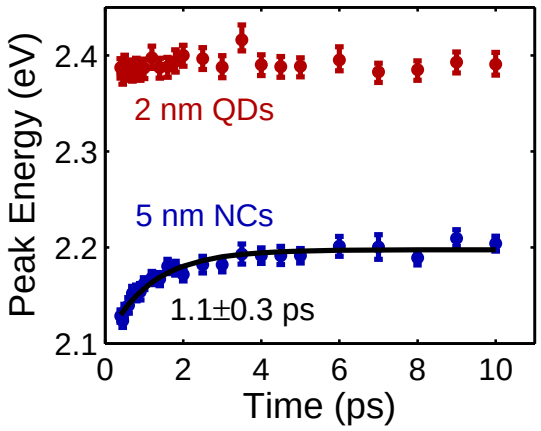

Figure 5.5: Peak shift of pump-probe spectra for 2 nm QDs (red) and 5 nm NCs (blue). Peak energies were measured by fitting the high energy portion of each spectrum to a quadratic. Error bars represent the one standard deviation confidence interval to the peak fit. Black line is an exponential fit to the 5 nm NC data.

sample are listed in Table 5.1. The entire ΔOD spectrum decayed to zero on these time scales, indicating that there was no remaining ESA or GSH after these decays. If trapping of the electrons, for example at the surface, was present, the ESA of the electrons in the conduction band would decay, but the GSH would persist. Correlated loss of signal at all probe energies indicates that the electrons returned to the original ground state on these time scales and therefore we assign these time constants to charge recombination. The average recombination times were calculated and are reported in Table 5.1. Average recombination times between the 2 nm QDs and the 5 nm NCs could not be distinguished from each other within the confidence limits of the fits. The fact

that the average recombination time is independent of NC size and, therefore, surface-area-to-volume ratio, is consistent with our conclusion that the electron recombines to the original ground state rather than being trapped at the surface. From the average lifetime and upper bound on the quantum yield, we assign a lower limit of 20 ns to the radiative lifetime and conclude that charge recombination is dominated by non-radiative relaxation with a lifetime of ∼20 ps.

The observed average recombination time of ∼20 ps is more than two orders of magnitude shorter than time constants reported for CdTe NCs[128;130] and is likely to be on of the factors leading to the lower (sub-1%) efficiencies for devices made with neat CZTS nanocrystals.[121] Increases in CZTS device efficiencies have been observed with adjustments to the stoichiometry and replacement of sulfur with selenium.[122;116;131] In these cases fluorescence has been observed, although the nature of the fluorescent excited states remains largely unexplored. The results presented here demonstrate that fluorescence is likely from excited states at non-stoichometric sites. Given the short measured charge recombination time in CZTS, the process of trapping to non-stoichiometric sites must be relatively efficient. Future studies to understand the nature of fluorescent excited states in non-stoichiometric CZTS are required to better understand these dynamics and how they influence device efficiency.

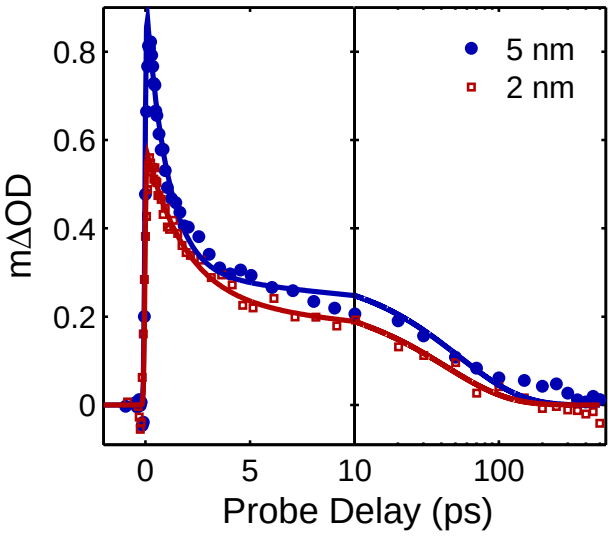

Figure 5.6: Pump-probe single color traces for 5 nm CZTS NCs for the probe range 2.0-2.4 eV (blue circles) and 2 nm CZTS QDs for the probe range 2.2-2.6 eV (red squares). Solid lines are biexponential fits to the data. The time axis is linear to 10 ps and logarithmic after.

Table 5.1: Spectral windows, time constants, and normalized amplitudes for biexponential ($A_1 e^{-t/\tau_1} + A_2 e^{-t/\tau_2}$) fits of CZTS pump-probe data. Reported uncertainties are the one standard deviation confidence intervals on the fitting parameters.

	energy range (eV)	τ_1 (ps)	A_1	τ_2 (ps)	A_2	τ_{avg} (ps)
5 nm NCs	2.0–2.4	1.0 ± 0.2	0.68	53 ± 7	0.32	18 ± 3
2 nm QDs	2.2–2.6	1.9 ± 0.2	0.59	43 ± 6	0.41	19 ± 3

5.4 Conclusions

In summary, ultrafast dynamics of CZTS NCs spanning the threshold for quantum confinement have been measured for the first time. Excited state absorption spectra are consistent with theoretical predictions for the density of states showing two energetically separated conduction bands. In smaller NCs, we observe that the two conduction bands increase their separation due to quantum confinement. Interband electron cooling in the 5 nm NCs occurs with a timescale of 1.1±0.3 ps. While this rate is slower than those for systems such as CdTe, it is still too fast for efficient hot electron transfer. The average charge recombination time is ∼20 ps and, within experimental error, is the same for both the 2 nm QD and 5 nm NC samples. Efficient nonradiative relaxation of the electron to the ground state may limit efficiencies in CZTS photovoltaics. The influence of stoichiometry on the charge carrier dynamics offers the potential to extend the lifetime, and perhaps optimize charge carrier behavior in different applications. The details of these systems are the subject of ongoing work.

Chapter 6

Exciton Fusion in PtOEP Thin Films

Portions of this chapter are adapted with permission from The Journal of Chemical Physics, 139(10):101102. Copyright 2013 AIP Publishing LLC.

6.1 Introduction

Porphyrins have been extensively studied due to their potential use in organic light emitting diodes (OLEDs) and organic photovoltaics (OPVs).[132;133;134;135] In particular, dye sensitized solar cells (DSSCs) using metalloporphyrins as the light harvesting component have reached efficiencies above 10%, making them competitive with benchmark

ruthenium-based dyes that are more expensive, less abundant, and environmentally unsafe.[136;137;138] These high efficiencies have been attributed to efficient absorption in the visible spectrum, as well as long-lived excited states.[139] Further optimization routes include creating arrays of porphyrin molecules to enhance light absorption (OPVs) or emission (OLEDs), but exciton-exciton annihilation limits these efficiency gains.[140;141]

In exciton-exciton annihilation, energy is transferred between two excitons leaving one in a less energetic state and the other in a more energetic state. Typically, this results in one exciton decaying to the ground state, while the other is excited to a higher lying state from which it quickly undergoes internal conversion to the original state. Typical annihilation is depicted for two singlet excitons in Equation 6.1 and Figure 6.1. The result of this process is the net loss of an exciton.

$$S_1 + S_1 \rightarrow S_0 + S_n \rightarrow S_0 + S_1 \tag{6.1}$$

Annihilation is of particular interest in platinum octaethylporphyrin (PtOEP) thin films. The presence of platinum increases the spin-orbit coupling due to the heavy-atom effect,[142;143] resulting in intersystem crossing to the lowest lying triplet state (T_1) in <200 fs.[144;145] This rapid preparation of triplets directly after excitation, coupled with a long triplet lifetime on the order of 100 µs,[146] has made PtOEP useful as a phosphor and triplet sensitizer.[147;148] The long triplet lifetime also allows for triplet-triplet annihilation (TTA) which limits device efficiency at high exciton densities.[149;150] Unlike the scheme presented in Equation 6.1 and Figure 6.1, in PtOEP thin films energy can

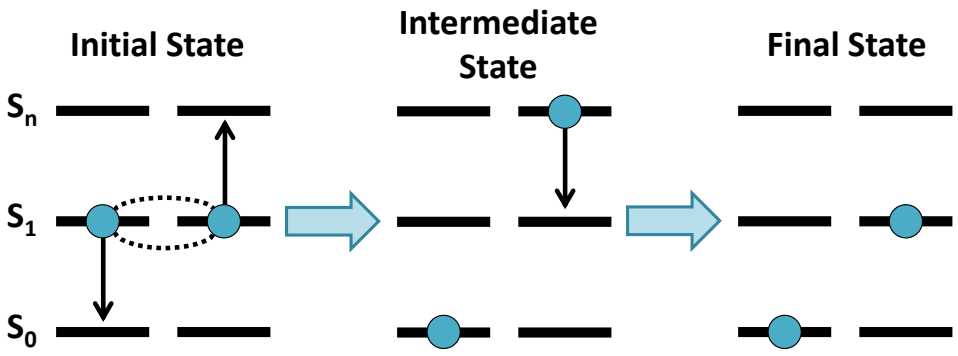

Figure 6.1: Schematic of exciton-exciton annihilation. Two S_1 excitons interact. One decays to S_0 and the other is further excited to S_n. The S_n exciton then undergoes internal conversion back to S_1.

be harvested from the intermediate step prior to internal conversion. This phenomenon has been used for photon upconversion in PtOEP doped polymer matrices.[151;152;153] Low energy photons are absorbed by the PtOEP, creating excitons which can undergo TTA. Excitons left in the high energy state after TTA transfer to the polymer matrix, where they radiatively decay emitting high energy photons (Figure 6.2).

The ability to transfer energy after TTA in PtOEP is not only interesting from a device perspective, but also from a mechanistic perspective. Because energy transfer is efficient, the unknown high energy state occupied after TTA must have a relatively long lifetime. That is, the exciton must not quickly decay by internal conversion. This could give the opportunity to measure the dynamics of TTA in PtOEP and better understand the mechanism behind annihilation in porphyrins. This chapter will present spectral signatures of the initial triplet state in PtOEP as well as the state occupied after TTA.

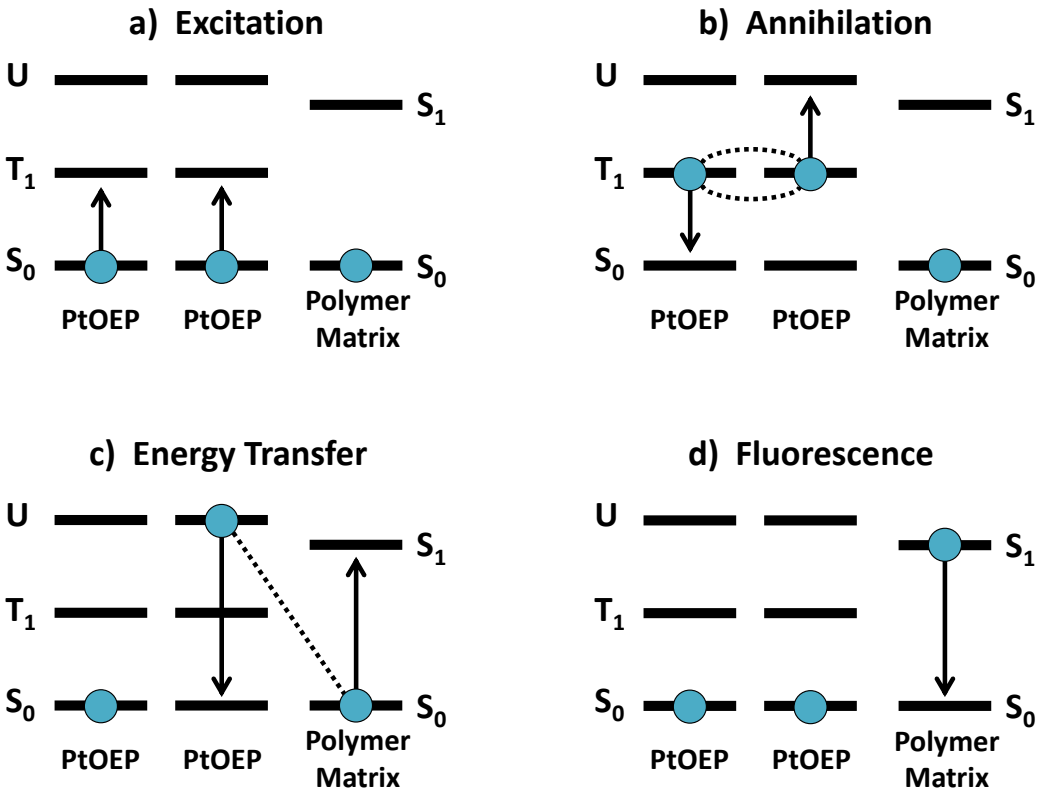

Figure 6.2: Schematic of exciton-exciton annihilation leading to fluorescence upconversion in a PtOEP doped polymer matrix. a) Low energy photons are absorbed by the PtOEP molecules creating singlet excitons which undergo fast intersystem crossing and internal conversion to T_1. b) Two T_1 excitons undergo TTA with one returning to the ground state and the other being excited to an unknown state, U. c) Energy is transferred from PtOEP to the polymer matrix. d) The exciton on the polymer matrix decays emitting high energy photons.

The shape of these signatures is used to assign the unknown high energy state, while the dynamics are analyzed using kinetic and energy transfer models.

6.2 Experimental Section

6.2.1 Sample Preparation

PtOEP was purchased and used as received from Frontier Scientific. PtOEP thin films were vapor deposited onto quartz disks by thermal deposition under high vacuum (10^{-7} TORR) at a rate of 0.2 nm/sec. Final film thickness was 60 nm as determined by ellipsometry.

6.2.2 Steady-State Spectroscopy

Absorption measurements were made using a Cary 14 spectrophotometer as described in Chapter 2. A background absorption scan of the bare quartz substrate was taken before each absorption measurement.

6.2.3 Pump-Probe Spectroscopy

Pump-probe measurements were conducted using the home-built Ti:Sapphire laser system described in Chapter 2, which produced 80 fs pulses at a 1 kHz repetition rate. The pump pulses had a photon energy of 3.1 eV and a waist ($1/e^2$) of 107 µm. The pump was modulated at half the laser repetition rate (500 Hz). The probe beam was a white light continuum that ranged from 1.6 to 2.7 eV. The pump polarization was kept at the

magic angle (54.7°) relative to the probe to isolate isotropic excited state dynamics.

PtOEP films were placed at the focus of the beams and rotated at a speed of 5 revolutions per second. The rotating films were contained in a box purged with nitrogen gas to prevent sample degradation. No bleaching of the films was observed due to laser illumination.

Power dependent traces were collected by detecting the transmitted probe beam with a photodiode (Thorlabs DET210). Interference filters (Thorlabs, 10 nm FWHM) were used to select specific probe energies to measure. The signal from the photodiode was measured using lock-in detection (SRS-810) at the pump frequency (500 Hz). The reported pump laser fluences were measured during the data collection by splitting a small portion of the excitation light before the sample and detecting it with a separate photodiode. A calibration curve was determined to convert the voltage measured by the photodiode to pump power as measured by a power meter (Coherent LM-2-VIS, Fieldmaster GS). The pump power was attenuated using a half-wave plate followed by a polarizer. To adjust the pump power the half-wave plate was slowly rotated while the signal on both diodes were measured. Finally, the incident power was converted to fluence using the pump waist measured above. Time dependent traces were collected in a similar manner, except that the pump fluence was set before the data collection and the pump-probe delay time was adjusted during the experiment.

6.3 Results and Discussion

6.3.1 Spectral Signature of TTA Products in PtOEP Thin Films

The absorption spectrum of a PtOEP film is shown in Figure 6.3. The feature at ∼2.3 eV is from $S_1 \leftarrow S_0$ absorption and is often referred to as Q band absorption, while the feature at ∼3.3 eV is $S_2 \leftarrow S_0$ absorption and referred to as B band absorption. Previous studies[144] have shown similar pump-probe spectra when pumping S_1 and S_2 suggesting initially created S_2 excitons quickly undergo internal conversion to S_1. Furthermore, S_1 excitons were shown to undergo intersystem crossing to T_1 in ∼160 fs. In the pump-probe experiments presented in this chapter, the excitons initially created in S_2 are assumed to quickly transfer to T_1.

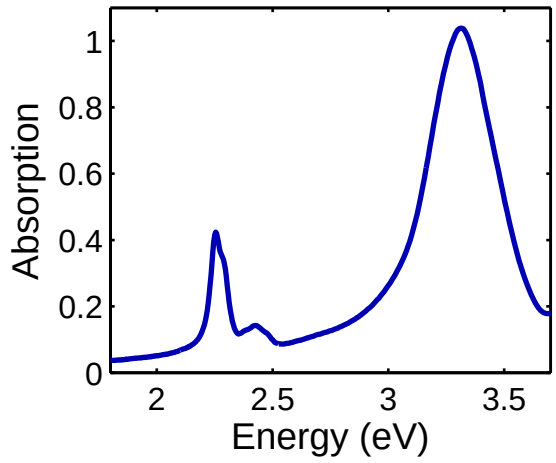

Figure 6.3: Absorption spectrum of a PtOEP thin film.

Pump-probe spectra for a PtOEP film pumped at 3.1 eV with a fluence of 3.3 x

10^{15} photons/cm^2 (ph/cm^2) are shown in Figure 6.4. At early times the spectra consist of a negative ground state hole (GSH) overlapping a broad transient absorption. This spectral shape is attributed to the presence of triplet excitons, T_1 after fast intersystem crossing but before significant TTA. At longer delay times, there is a time-dependent loss of triplet signal, most evident for probe energies above 2.40 eV, and a correlated rise in absorption at 2.20 eV. In dilute solutions of PtOEP under similar conditions no time-dependent evolution of the ΔOD spectrum was measured, implying that the observed dynamics are not the result of multi-photon absorption in individual molecules.[144]

The bottom panel of Figure 6.4 presents the dependence of the pump-probe spectrum on pump fluence at a delay time of 500 ps. As the pump fluence was increased, the relative contribution of the new feature at 2.20 eV increased at the expense of the broad absorption from T_1. The new feature has a differential shape centered at a slightly lower energy than the original Q-band absorption maximum. This spectral shape is similar to that observed in nickel porphyrins which has been attributed to energy transfer from the porphyrin ring to a metal-centered $^3(d,d)$ state.[154;155] In nickel porphyrins the $^3(d,d)$ state is located just below the S_1 state in energy, providing direct access to $^3(d,d)$ in $\sim$1 ps following single photon excitation. Localization of the exciton to the metal causes the absorption spectrum to red shift. This added absorption overlaps with the ground state hole to give the differential shape observed.

A fit to the pump probe spectrum for a delay time of 500 ps is shown in Figure 6.5. The fit is made up of components consisting of T_1 and $^3(d,d)$ signatures. An early time

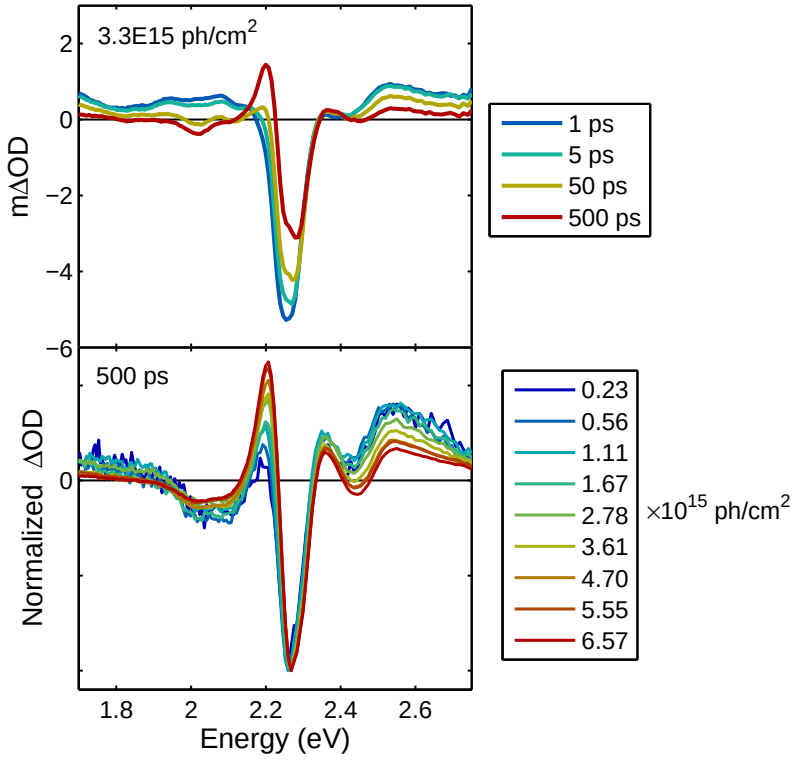

Figure 6.4: Pump-probe spectra for a PtOEP thin film pumped at 3.1 eV. Top: Pump-probe spectra as a function of delay time with a pump fluence of 3.3 x 10^{15} ph/cm^2. Bottom: Pump-probe spectra for as a function of fluence with a delay time of 500 ps. All spectra were scaled to have the same value at 2.25 eV.

pump-probe spectrum was used to model the T_1 spectral shape. The $^3(d,d)$ state was modeled as the sum of a redshifted PtOEP absorption spectrum, representing the added absorption, and a negated PtOEP absorption spectrum, representing the ground state hole. A linear combination of the T_1 and $^3(d,d)$ features was used to fit the spectrum as described by Equation 6.2.

$$\begin{aligned} \Delta OD &= A\ (\Delta OD)_{T_1} + B\ (\Delta OD)_{(d,d)} \\ &= A\ \Delta OD_{300\,\mathrm{fs}} + B\ [\mathrm{abs}(E-\delta) - \mathrm{abs}(E)] \end{aligned} \tag{6.2}$$

The weighting factors, A and B, and the energy offset, δ, were optimized giving $A = 1.53$, $B = 2.15$, and $\delta = 0.045eV$ for the 500 ps delay pump-probe spectrum.

Because of the good agreement between the pump-probe spectrum and the fitting model, we conclude that the changes in the pump-probe spectra are due to loss of T_1 and formation of $^3(d,d)$. Unlike in nickel porphyrins, the $^3(d,d)$ state is energetically inaccessible from S_1 and T_1 in porphyrins with heavier metal atoms such as platinum.[156] Because the formation of the $^3(d,d)$ state is dependent on pump fluence (Figure 6.4), we propose that the $^3(d,d)$ state is a product of TTA. With no spectral evidence of intermediate species, we consider direct fusion of two triplets to produce the excited metal-centered state as presented in Figure 6.6,

$$T_1 + T_1 \xrightarrow{k_{\mathrm{TTF}}} D^* + S_0. \tag{6.3}$$

where the $^3(d,d)$ state has been labeled D^*. Competing unimolecular decay of T_1 was

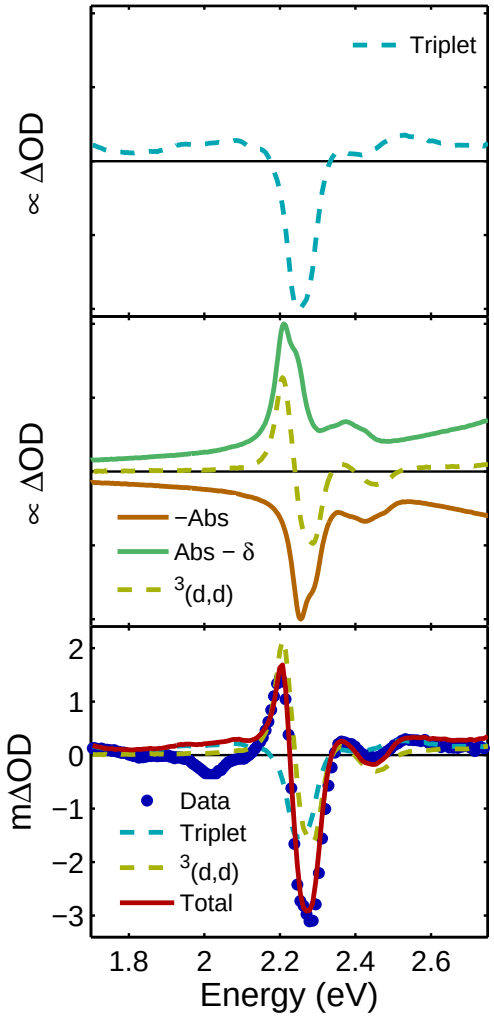

Figure 6.5: Fitting pump-probe spectra for a PtOEP thin film. Top: Early time pump-probe spectrum used to represent the triplet signature (teal). Middle: Simulated spectral signature of the $^3(d,d)$ state (yellow) made up of the sum of the negative ground state absorption spectrum (orange) and a redshifted ground state absorption spectrum (green). Bottom: Pump-probe data at a 500 ps delay time (blue) along with the fit to data (red) made up of the triplet signature (teal) and the $^3(d,d)$ signature (yellow).

considered negligible on the time scale of the experiment.[144] Decay of the $^3(d,d)$ state was also ignored. Although the lifetime of the $^3(d,d)$ state could not be determined, the signal from the $^3(d,d)$ state persists at a time delay of 11 ns conservatively indicating a lifetime of >1 ns (Figure 6.7).

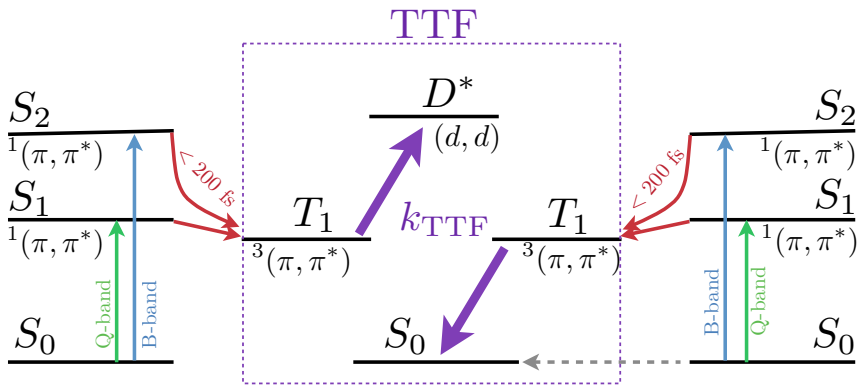

Figure 6.6: Diagram of triplet-triplet annihilation in PtOEP thin films that leads to upconversion of the initial ring states into a metal-centered state.

6.3.2 Kinetic Modeling

The previous section illustrated a spectral signature of TTA products in PtOEP thin films. Modeling these features as a function of pump power and pump-probe delay time gives insight into the mechanism of TTA in PtOEP. In this section, TTA will be modeled using second order kinetics. The rate expression for Equation 6.3 can be written

$$-\frac{1}{2}\frac{d[T_1]}{dt} = \frac{d[D^*]}{dt} = k_{\mathrm{TTF}}[T_1]^2. \tag{6.4}$$

Integrating Equation 6.4 with the initial condition $[D^*]_0 = 0$ gives $[D^*]$ and $[T_1]$ as a

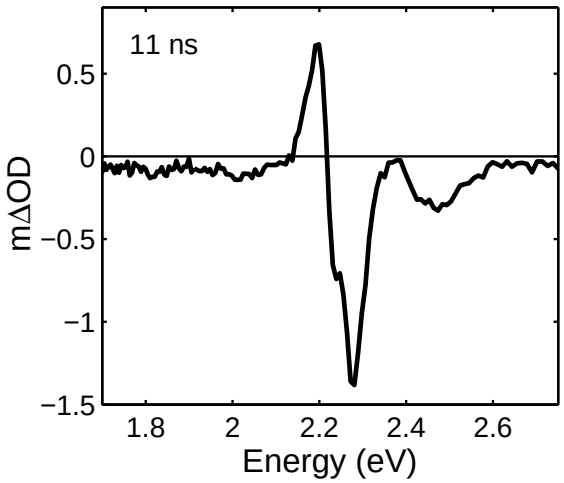

Figure 6.7: Pump-probe spectrum for a PtOEP thin film with a delay time of 11 ns. Due to changes in pump fluence, pump-probe crossing, and pump focal parameters the absolute ΔOD measured is not comparable to those in Figure 6.4.

function of time and initial triplet concentration, $[T_1]_0$:

$$[D^*] = \frac{[T_1]_0^2 k_{\mathrm{TTF}} t}{1 + 2[T_1]_0 k_{\mathrm{TTF}} t}, \tag{6.5}$$

$$[T_1] = -\frac{[T_1]_0}{1 + 2[T_1]_0 k_{\mathrm{TTF}} t}. \tag{6.6}$$

The initial triplet concentration is related to the incident pump fluence by Equation 6.7 (units indicated in brackets, abs ph stands for absorbed photons and inc ph stands for incident photons).

$$[T_1]_0 \left[\frac{\text{abs ph}}{\text{cm}^3}\right] = F \left[\frac{\text{inc ph}}{\text{cm}^2}\right] \times A \left[\text{cm}^2\right] \times 0.2645 \left[\frac{\text{abs ph}}{\text{inc ph}}\right] \times \frac{1}{A \cdot l} \left[\frac{1}{\text{cm}^3}\right] \tag{6.7}$$

The fluence is multiplied by the spot size, A, to find the number of incident photons. By measuring the power before and after the sample, and taking into account reflections at interfaces using Snell's Law, the ratio of absorbed photons to incident photons was found to be 0.2645. Finally, assuming constant absorption throughout the film and that each absorbed photon creates a triplet exciton, the initial triplet concentration is found by dividing the photons absorbed by the volume the pump passes through, $A \cdot l$ where l is the film thickness. For a film thickness of 60 nm Equation 6.7 simplifies to Equation 6.8.

$$[T_1]_0 = \left(44083\,\mathrm{cm}^{-1}\right) \cdot F \tag{6.8}$$

Figure 6.8 presents the dependence of ΔOD on the pump fluence at 3 probe energies for a time delay of 10 ps. At a given probe energy, E, the ΔOD was expressed as a linear combination of contributions from $[T_1]$ and $[D^*]$ as expressed in Equations 6.5 and 6.6,

$$\Delta OD_E = \alpha_{T_1,E}[T_1] + \alpha_{D^*,E}[D^*]. \tag{6.9}$$

The ground state, $[S_0]$, is not considered because it does not contribute to the ΔOD spectrum. The relative weighting factors, $\alpha_{x,E}$, account for the total contributions to the ΔOD from each species comprising transient absorption (positive ΔOD) and ground state bleach (negative ΔOD). The contribution from the $^3(d,d)$ state at 2.58 eV is approximated to be zero, $\alpha_{D^*,E=2.58\ \mathrm{eV}} = 0$, based on the cancellation between

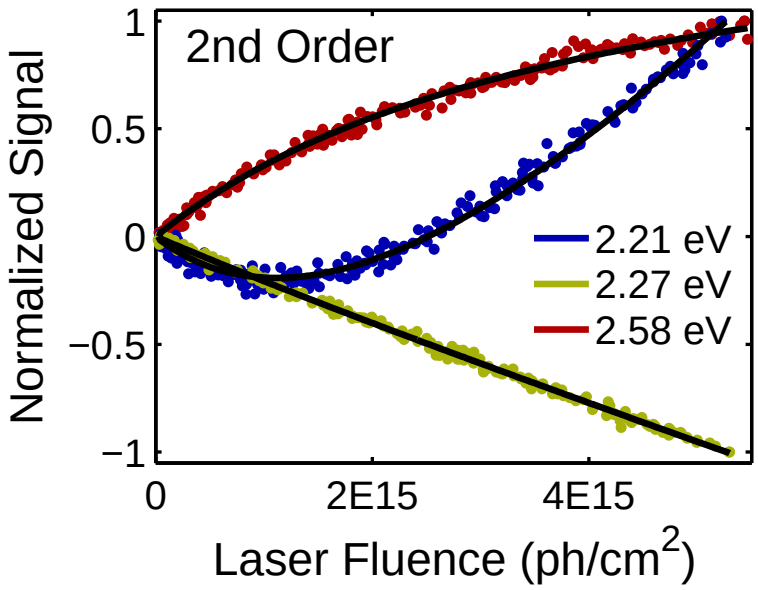

Figure 6.8: Kinetic modeling of power dependent pump-probe traces at a delay of 10 ps. The points represent the data and the lines are the fits as described in the text.

Table 6.1: Fitting parameters for power dependent pump-probe traces of a PtOEP thin film. The errors are the 95% confidence intervals in the nonlinear fitting when all variables are simultaneously optimized.

k_{TTF}	$(2.7 \pm 0.2) \times 10^{-10}$ cm$^3 \cdot$ s^{-1}
$\alpha_{T_1, E=2.21\ \mathrm{eV}}$	$-(8.9 \pm 0.3) \times 10^{-21}$
$\alpha_{D^*, E=2.21\ \mathrm{eV}}$	$(2.9 \pm 0.2) \times 10^{-20}$
$\alpha_{T_1, E=2.27\ \mathrm{eV}}$	$-(5.2 \pm 0.2) \times 10^{-21}$
$\alpha_{D^*, E=2.27\ \mathrm{eV}}$	$-(7.2 \pm 0.4) \times 10^{-21}$
$\alpha_{T_1, E=2.58\ \mathrm{eV}}$	$(9.3 \pm 0.3) \times 10^{-21}$

the transient absorption and ground state bleach shown in Figure 6.5. The data at all 3 probe energies were simultaneously fitted using Equations 6.5, 6.6, and 6.9 as shown in Appendix A.7. The fitting parameters are given in Table 6.1.

The agreement between the data and the model demonstrates that TTA is consistent with the second order mechanism proposed proposed in Equation 6.3. Using time integrated emission to measure loss of triplet phosphorescence, Mezyk *et al.* reported a TTA rate coefficient of $(8\pm3)\times10^{-12}$ $\mathrm{cm}^3\cdot\mathrm{s}^{-1}$.[157] This is nearly two orders of magnitude lower than the TTA rate coefficient reported here. The difference may originate from the time dependence of the rate coefficient when the rate is not transport limited. The value of k_{TTF} reported here was determined at a time delay of 10 ps and is therefore more indicative of an initial rate.

Figure 6.9 shows time dependent pump-probe traces at different pump fluences with a probe energy of 2.58 eV. They were globally fit in the same manner as the power dependent traces above. The quality of the fits is poor indicating that a constant second order rate coefficient is insufficient to model the TTA as a function of time. Second order dynamics have been used to model diffusion of particles which instantly coagulate if two particles become closer than a critical distance.[29] This situation is equivalent to TTA where excitons diffuse through the film and instantaneously annihilate if they become close enough to each other.[158] Thus, second order dynamics are only valid if individual exciton hops and the dynamics of the energy transfer mechanism can be neglected. Because of the poor fits in Figure 6.9 we conclude this is not the case for PtOEP

thin films and more sophisticated models which take into account energy transfer are necessary.

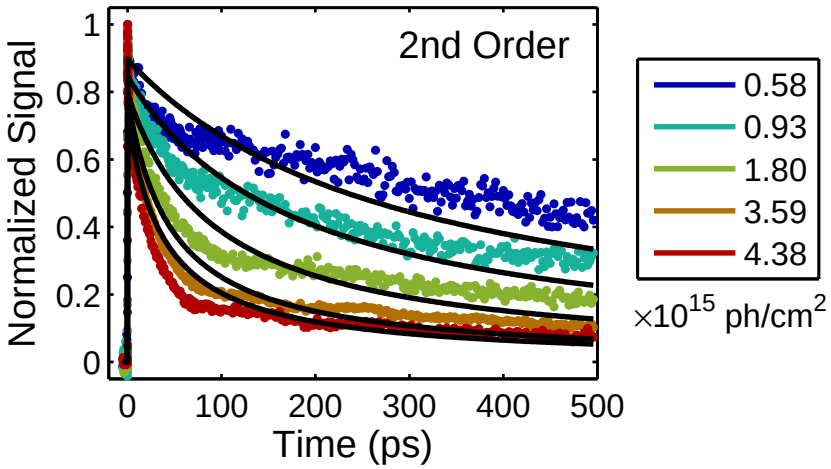

Figure 6.9: Kinetic modeling of time dependent pump-probe traces at different pump fluences with a probe energy of 2.58 eV. The points represent the data and the lines are the fits as described in the text.

6.3.3 Energy Transfer Modeling

In the previous section, it was shown that a second order kinetic model could not adequately capture the dynamics of TTA in PtOEP thin films. The second order model assumes excitons take many random steps through the film and annihilate instantaneously if two excitons move within a critical distance of each other. In the current section, annihilation will be modeled as a long-range energy transfer event with no exciton diffusion present. The rate coefficient for standard Förster and Dexter energy

transfer are given in Equations 6.10 and 6.11, respectively:

$$k_F = \frac{1}{\tau}\left(\frac{R_F}{r}\right)^6, \tag{6.10}$$

$$k_D = \kappa e^{-2r/L}. \tag{6.11}$$

The constants τ, R_F, κ, and L are described in Section 1.3.2. It should be noted these rate coefficients are for energy transfer from a donor to an acceptor, not for annihilation. In order to model pump-probe data, the rate coefficients are used to obtain the ratio of excitons remaining after time t, $\phi(t) = n(t)/n_0$, where $n(t)$ is the exciton concentration at time t and n_0 is the initial exciton concentration. Once $\phi(t)$ has been found, the solution will be recast to take into account annihilation.

A general equation to convert an energy transfer rate coefficient that depends on the donor-acceptor distance, $k(r)$, to the ratio of excited donors as a function of time, $\phi(t)$, is described by Inokuti and Hirayama by Equation 6.12:

$$\phi(t) = \exp\left(-\frac{t}{\tau}\right) \lim_{\substack{N,V\to\infty \\ N/V=c}} \left\{\frac{4\pi}{V}\int_0^{R_V} \exp\left[-k(r)t\right] r^2 \mathrm{d}r\right\}^N \tag{6.12}$$

where τ is the natural lifetime of the donor and N is the number of acceptors in a volume $V = 4\pi R_V^3/3$ giving an acceptor concentration, c.[159] Note that the limit is taken such that N and V (and, subsequently, R_V) go to infinity in a manner such that the acceptor concentration, c, is held constant. Substituting in the Dexter rate coefficient (Equation

6.11) gives:

$$\phi(t) = \exp\left(-\frac{t}{\tau}\right) \lim_{\substack{N,V\to\infty \\ N/V=c}} \left\{ \frac{4\pi}{V} \int_0^{R_V} \exp\left[-\kappa t e^{-2r/L}\right] r^2 \mathrm{d}r \right\}^N . \tag{6.13}$$

The simplification of Equation 6.13, which is similar to that carried out by Inokuti and Hirayama,[159] will be briefly shown. To solve the integral in Equation 6.13, the substitutions $z = \kappa t$ and $y = \exp[-2r/L]$ are used:

$$\frac{4\pi}{V} \int_0^{R_V} \exp\left[-\kappa t e^{-2r/L}\right] r^2 \mathrm{d}r = \frac{3L^3}{8R_V^3} \int_{Y_V}^1 e^{-zy} (\ln y)^2 y^{-1} \mathrm{d}y \tag{6.14}$$

where $Y_V = \exp[-2R_V/L]$. Using integration by parts ($u = e^{-zy}$, $\mathrm{d}v = (\ln y)^2 y^{-1}\mathrm{d}y$) Equation 6.14 simplifies to:

$$\frac{3L^3}{8R_V^3} \left\{ -\frac{e^{-zY_V}}{3} (\ln Y_V)^3 + \frac{z}{3} \int_{Y_V}^1 e^{-zy} (\ln y)^3 \mathrm{d}y \right\}. \tag{6.15}$$

Because the limit will be taken such that $R_V \to \infty$, $Y_V = \exp[-2R_V/L]$ is assumed to be small. Thus, $e^{-zY_V} \to 1$ and the limits of integration in Equation 6.15 can be taken to be from 0 to 1. Substituting back into Equation 6.13 the ratio of excited donors is:

$$\phi(t) = \exp\left(-\frac{t}{\tau}\right) \lim_{\substack{N,V\to\infty \\ N/V=c}} \left\{ 1 - \frac{L^3}{8R_V^3} g(\kappa t) \right\}^N \tag{6.16}$$

where

$$g(x) = -x \int_0^1 e^{-xy} (\ln y)^3 \mathrm{d}y. \tag{6.17}$$

To take the limit, the natural log of the argument is taken and R_V^{-3} is replaced with $(4\pi c)/(3N)$ so that the limit is only over N:

$$\lim_{\substack{N,V\to\infty \\ N/V=c}} N \ln\left(1 - \frac{L^3}{8R_V^3} g(\kappa t)\right) = \lim_{N\to\infty} N \ln\left(1 - \frac{1}{N}\frac{\pi L^3 c}{6} g(\kappa t)\right). \tag{6.18}$$

This limit is of the form given in Equation 6.19 with $\alpha = (\pi L^3 c/6) g(\kappa t)$, which is solved using l'Hôpital's rule:

$$\lim_{N\to\infty} \frac{\ln\left(1 - \frac{\alpha}{N}\right)}{\frac{1}{N}} \overset{l'h}{=} \lim_{N\to\infty} \frac{\frac{1}{1-\frac{\alpha}{N}}\frac{\alpha}{N^2}}{-\frac{1}{N^2}} = -\lim_{N\to\infty} \frac{\alpha}{1-\frac{\alpha}{N}} = -\alpha. \tag{6.19}$$

Combining Equations 6.16, 6.18, and 6.19 gives:

$$\phi(t) = \exp\left(-\frac{t}{\tau}\right) \exp\left(-\frac{\pi L^3 c}{6} g(\kappa t)\right) \tag{6.20}$$

with $g(x)$ defined by Equation 6.17. To reiterate, Equation 6.20 is the ratio of initially excited donors that are still excited after a time t when the donors can only decay naturally or by Dexter energy transfer.

To recast Equation 6.20 for use in annihilation, a procedure prescribed by Engel *et al.* is employed.[158] To begin, a rate equation is written and simplified:

$$n(t) = n_0\phi(t) \implies \frac{dn(t)}{dt} = n_0\frac{d\phi(t)}{dt} = n_0\phi(t)\left(-\frac{1}{\tau} - \frac{\pi L^3 c}{6}\frac{d}{dt} g(\kappa t)\right). \tag{6.21}$$

We now make two observations. First, $n_0\phi(t) = n(t)$. Second, c is the concentration

of acceptor molecules which induce decay of the excited donors described by the concentration, $n(t)$. In annihilation, there are no acceptors which cause excited states to decay. Instead, the decay of excited states is induced by other excited states, so the concentration c is replaced by the concentration of excited states, $n(t)$. Using these two substitutions the annihilation rate equation is found to be:

$$\frac{dn(t)}{dt} = -\frac{n}{\tau} - \frac{\pi L^3}{6}\left[\frac{d}{dt}g(\kappa t)\right] n(t)^2. \tag{6.22}$$

For the PtOEP films studied here, τ is much larger than the time scale of the experiment so the first term goes to zero. This is equivalent to saying that during our experiment very few of the PtOEP excited states decay naturally due to their long lifetimes (∼100 µs). Finally, the excited state in the PtOEP thin films is T_1, so the concentration of excited states $n(t)$ is replaced with $[T_1]$ and the initial excited state concentration n_0 is replaced with $[T_1]_0$. The final Dexter TTA rate equation for PtOEP thin films is given by Equation 6.23

$$\frac{d[T_1]}{dt} = -\frac{\pi L^3}{6}\left[\frac{d}{dt}g(\kappa t)\right] [T_1]^2. \tag{6.23}$$

Integrating the rate equation gives the triplet concentration as a function of time and the initial triplet concentration:

$$[T_1] = \frac{[T_1]_0}{1 + [T_1]_0 \frac{\pi L^3}{6} g(\kappa t)}. \tag{6.24}$$

For TTA described by $T_1 + T_1 \longrightarrow D^* + S_0$, half of the triplets decay to S_0 and half are excited to D^*. This can be used to find the concentration of the metal-centered state D^* where D_0^* is the initial concentration of metal-centered excited states which is taken to be zero:

$$[D^*] = [D^*]_0 + \frac{[T_1]_0 - [T_1]}{2} = \frac{[T_1]_0^2 \frac{\pi L^3}{12} g(\kappa t)}{1 + [T_1]_0 \frac{\pi L^3}{6} g(\kappa t)}. \tag{6.25}$$

Equations 6.24 and 6.25 can be used in conjunction with Equation 6.9 to model pump-probe data as Dexter energy transfer TTA, just as Equations 6.6 and 6.5 were used to model second order kinetic (diffusion-limited) TTA.

To get the analogous concentrations for Förster energy transfer TTA, Equation 6.10 is substituted into Equation 6.12:

$$\phi(t) = \exp\left(-\frac{t}{\tau}\right) \lim_{\substack{N,V\to\infty \\ N/V=c}} \left\{ \frac{4\pi}{V} \int_0^{R_V} \exp\left[-\frac{t}{\tau}\left(\frac{R_F}{r}\right)^6\right] r^2 \mathrm{d}r \right\}^N. \tag{6.26}$$

Using the substitution $Z = t/\tau \cdot (R_F/r)^6$ Equation 6.26 can be written:

$$\phi(t) = \exp\left(-\frac{t}{\tau}\right) \lim_{\substack{N,V\to\infty \\ N/V=c}} \left\{ \frac{\sqrt{Z_V}}{2} \int_{Z_V}^{\infty} Z^{-3/2} e^{-Z} \mathrm{d}Z \right\}^N \tag{6.27}$$

where $Z_V = t/\tau \cdot (R_F/R_V)^6$. The integral in Equation 6.27 was simplified using Maple:

$$\int_{Z_V}^{\infty} Z^{-3/2} e^{-Z} \mathrm{d}Z = 2\left[Z_V^{-1/2} e^{-Z_V} + \sqrt{\pi}\,\mathrm{erf}\left(\sqrt{Z_V}\right) - \sqrt{\pi}\right] \tag{6.28}$$

where erf(x) is the error function which, for small x, can be approximated:

$$\operatorname{erf}(x) = \frac{2}{\sqrt{\pi}} \int_0^x \exp\left[-t^2\right] \mathrm{d}t \approx \frac{2}{\sqrt{\pi}} x. \tag{6.29}$$

In the limit of large V and R_V, Z_V is small and the approximation in Equation 6.29 is valid. Combining Equations 6.27, 6.28, and 6.29 gives:

$$\phi(t) = \exp\left(-\frac{t}{\tau}\right) \lim_{\substack{N,V\to\infty \\ N/V=c}} \left\{e^{-Z_V} + 2Z_V - \sqrt{Z_V \pi}\right\}^N. \tag{6.30}$$

To find the limit, the natural log of the argument is taken and the substitution

$$N = \frac{4\pi R_F^3 c}{3} \sqrt{\frac{t}{\tau}} \frac{1}{\sqrt{Z_V}}$$

is used so that the limit is only over Z_V:

$$\lim_{\substack{N,V\to\infty \\ N/V=c}} N \ln\left[e^{-Z_V} + 2Z_V - \sqrt{Z_V \pi}\right] = \frac{4\pi R_F^3 c}{3} \sqrt{\frac{t}{\tau}} \lim_{Z_V \to 0} \frac{\ln\left[e^{-Z_V} + 2Z_V - \sqrt{Z_V \pi}\right]}{\sqrt{Z_V}}. \tag{6.31}$$

The limit in Equation 6.31 is of the form given in Equation 6.32 with $x = \sqrt{Z_V}$, which is solved using l'Hôpital's rule:

$$\lim_{x\to 0} \frac{\ln\left[e^{-x^2} + 2x^2 - \sqrt{\pi} x\right]}{x} \overset{l'h}{=} \lim_{x\to 0} \frac{(-2x)e^{-x^2} + 4x - \sqrt{\pi}}{e^{-x^2} + 2x^2 - \sqrt{\pi} x} = -\sqrt{\pi}. \tag{6.32}$$

Using Equations 6.30, 6.31, and 6.32 the ratio of excited donors is:

$$\phi(t) = \exp\left(-\frac{t}{\tau}\right)\exp\left(-\frac{4\pi R_F^3 c}{3}\sqrt{\frac{\pi t}{\tau}}\right). \tag{6.33}$$

Similar to the Dexter transfer discussion above, Equation 6.33 is only applicable for initially excited donors which can decay naturally or through Förster energy transfer to acceptors.

To recast from energy transfer to TTA, the rate equation for Equation 6.33 is simplified:

$$n(t) = n_0\phi(t) \implies \frac{dn(t)}{dt} = n_0\frac{d\phi(t)}{dt} = n_0\phi(t)\left(-\frac{1}{\tau} - \frac{2\pi^{3/2}R_F^3}{3}\sqrt{\frac{1}{\tau t}}c\right). \tag{6.34}$$

Making the substitutions $n_0\phi(t) = n$ and $c = n$, the rate equation for Förster energy transfer TTA is found. For the particular case of PtOEP TTA, $n = [T_1]$ and the triplet lifetime, τ, is long compared to the time-scale of the experiment allowing for the first term in the right hand side of Equation 6.34 to be neglected. This gives the final rate equation for Förster energy transfer TTA in PtOEP:

$$\frac{d[T_1]}{dt} = -\frac{2\pi^{3/2}R_F^3}{3}\sqrt{\frac{1}{\tau t}}\,[T_1]^2. \tag{6.35}$$

Integrating Equation 6.35 gives the triplet concentration as a function of time:

$$[T_1] = \frac{[T_1]_0}{1 + [T_1]_0\frac{4\pi^{3/2}R_F^3}{3}\sqrt{\frac{t}{\tau}}}. \tag{6.36}$$

Using the fact that half of the triplets lost go to the metal-centered state, the concentration $[D^*]$ is found to be:

$$[D^*] = \frac{[T_1]_0^2 \frac{2\pi^{3/2} R_F^3}{3} \sqrt{\frac{t}{\tau}}}{1 + [T_1]_0 \frac{4\pi^{3/2} R_F^3}{3} \sqrt{\frac{t}{\tau}}}. \tag{6.37}$$

Equations 6.36 and 6.37 can be used to model pump-probe data as Förster energy transfer TTA.

Figure 6.10 shows global fits to power and time dependent pump-probe traces for Dexter and Förster energy transfer TTA. All 8 data sets (3 power dependent and 5 time dependent) were fit simultaneously for each model. Code for the fitting models are given in Appendix A.8. The global fitting parameters are given in Table 6.2. The Dexter model returns a better fit to the data than the Förster model. Furthermore, the optimized effective Bohr radius $L = 0.70$ nm is $\sim$60% of the PtOEP molecular size (1.2 nm) which is consistent with theoretical predictions.[33] The optimized Förster radius of 15 nm is large compared to typical Förster radii of 1-10 nm. For weakly luminescent excited states, such as the PtOEP triplets studied here, a Förster radius this large would not be expected.

6.4 Conclusions

The pump-probe spectra presented in this chapter reveal the spectral signature of the TTA product in PtOEP thin films. Analysis of the spectral shape indicates the TTA product is a metal-centered $^3(d,d)$ state. The signature of the $^3(d,d)$ state persists for

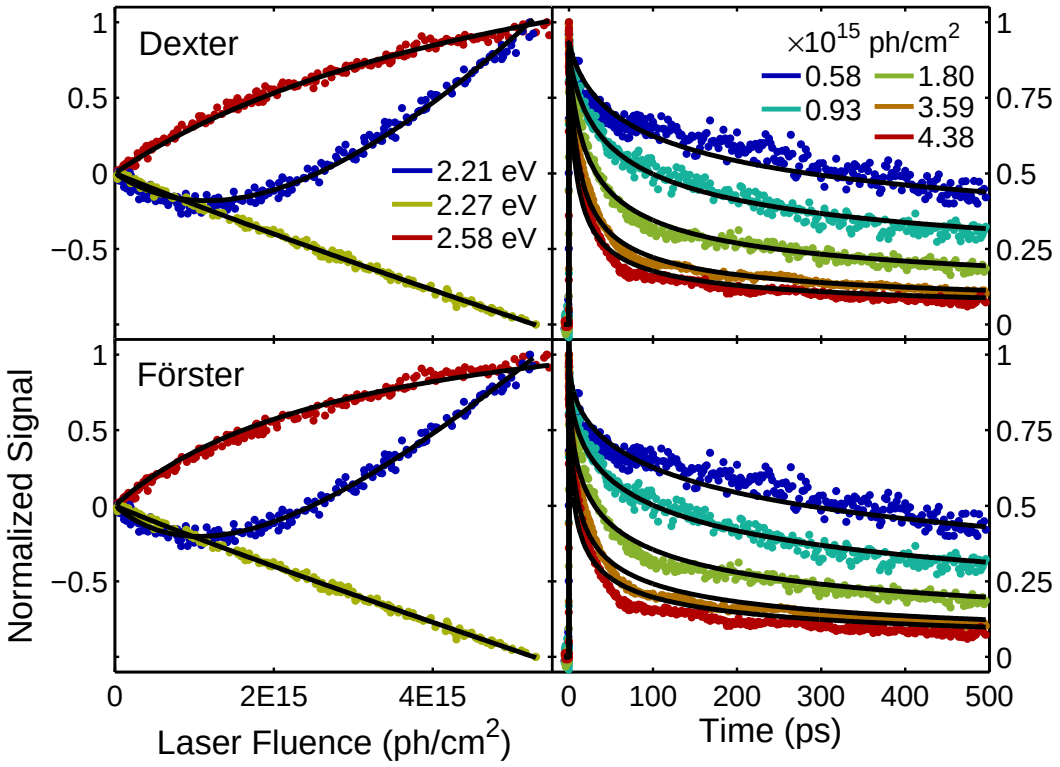

Figure 6.10: Dexter (top) and Förster (bottom) energy transfer modeling of power (left) and time (right) dependent pump-probe traces. The points represent the data and the lines represent the fits.

Table 6.2: Global fitting parameters of power and time dependent pump-probe traces of a PtOEP thin film. To find the Förster radius, a triplet lifetime of $\tau = 95$ µs was used.[149]

			Dexter	Förster
Global Parameters		L (nm)	0.70	–
		κ (s^{-1})	4.4×10^{11}	–
		R_F (nm)	–	15
	Fluence (10^{15} ph/cm^2)			
Time Dependent	0.58	α_{T_1}	3.7×10^{-20}	3.9×10^{-20}
	0.93	α_{T_1}	2.2×10^{-20}	2.4×10^{-20}
	1.80	α_{T_1}	1.1×10^{-20}	1.3×10^{-20}
	3.59	α_{T_1}	5.7×10^{-21}	7.2×10^{-21}
	4.38	α_{T_1}	4.4×10^{-21}	5.6×10^{-21}
	Probe Energy (eV)			
Power Dependent	2.21	α_{T_1}	-7.8×10^{-21}	-1.1×10^{-20}
		α_{D^*}	3.6×10^{-20}	2.5×10^{-21}
	2.27	α_{T_1}	-4.8×10^{-21}	-4.9×10^{-21}
		α_{D^*}	-7.4×10^{-21}	-7.9×10^{-21}
	2.58	α_{T_1}	8.1×10^{-21}	1.1×10^{-20}

more than 11 ns indicating that TTA in PtOEP thin films results in a long-lived state. Delayed fluorescence upconversion observed in PtOEP conjugated polymer composite films by Keivanidis *et al.* demonstrates the potential to harvest energy stored in the $^3(d,d)$ state after TTA.[151;152;153] Fitting the power dependence of the TTA at 10 ps using second order kinetics gave a rate coefficient of $(2.7 \pm 0.2) \times 10^{-10}$ cm$^3 \cdot$ s^{-1}. Second order kinetic fitting to the time dependent TTA traces resulted in poor fits. Förster and Dexter energy transfer models were fit to the power and time dependent pump-probe results, with the Dexter results better matching the pump-probe data. Furthermore, the Förster radius returned by the fitting routine ($R_F = 15$ nm) is larger than expected for triplet excitons. Thus, the mechanism of triplet-triplet annihilation in PtOEP thin films is assigned to Dexter energy transfer with an effective Bohr radius of $L = 0.70$ nm. We have elucidated a new mechanism for upconversion of visible photons stored as molecular potential energy. The upconverted energy is stored in a long-lived state and can be used to drive further chemistry.

References

[1] U.S. Energy Information Administration. International Energy Outlook 2013. 2013.

[2] C.A. Wolden, J. Kurtin, J.B. Baxter, I. Repins, S.E. Shaheen, J.T. Torvik, A.A. Rockett, V.M. Fthenakis, and E.S. Aydil. Photovoltaic manufacturing: Present status, future prospects, and research needs. *Journal of Vacuum Science & Technology A: Vacuum, Surfaces, and Films*, 29(3):030801, 2011.

[3] N.S. Lewis and D.G. Nocera. Powering the planet: Chemical challenges in solar energy utilization. *Proceedings of the National Academny of Sciences*, 103(43):15729–15735, 2006.

[4] M.I. Hoffert, K. Caldeira, A.K. Jain, and E.F. Haites. Energy implications of future stabilization of atmospheric CO2 content. *Nature*, 395:881–884, 1998.

[5] M.I. Hoffert, K. Caldeira, G. Benford, D.R. Criswell, C. Green, H. Herzog, A.K. Jain, H.S. Kheshgi, K.S. Lackner, J.S. Lewis, H.D. Lightfoot, W. Manheimer, J.C. Mankins, M.E. Mauel, L.J. Perkins, M.E. Schlesinger, T. Volk, and T.M.L. Wigley.

Advanced technology paths to global climate stability: energy for a greenhouse planet. *Science*, 298(5595):981–987, 2002.

[6] N.S. Lewis. Powering the Planet. *MRS Bulletin*, 32:808, 2007.

[7] J. Kalowekamo and E. Baker. Estimating the manufacturing cost of purely organic solar cells. *Solar Energy*, 83(8):1224–1231, 2009.

[8] M.A. Green, K. Emery, Y. Hishikawa, W. Warta, and E.D. Dunlop. Solar cell efficiency tables (version 42). *Progress in Photovoltaics: Research & Applications*, 21:827–837, 2013.

[9] W. Shockley and H.J. Queisser. Detailed Balance Limit of Efficiency of p-n Junction Solar Cells. *Journal of Applied Physics*, 32(3):510–519, 1961.

[10] National Renewable Energy Laboratory. *Best Research-Cell Efficiencies, NREL*. Accessed 2-18-2014, www.nrel.gov/ncpv/, 2014.

[11] A. Jager-Waldau. Progress in chalcopyrite compound semiconductor research for photovoltaic applications and transfer of results into actual solar cell production. *Solar Energy Materials and Solar Cells*, 95(6):1509–1517, 2011.

[12] R.G. Gordon. Criteria for choosing transparent conductors. *MRS bulletin*, pages 52–57, 2000.

[13] C. Kittel. *Introduction to Solid State Physics*. John Wiley and Sons, Inc., 1986.

[14] M.D. Archer and J.R. Bolton. Requirements for ideal performance of photochemical and photovoltaic solar energy converters. *Journal of Physical Chemistry*, 94(21):8028–8036, 1990.

[15] B.A. Gregg and M.C. Hanna. Comparing organic to inorganic photovoltaic cells: Theory, experiment, and simulation. *Journal of Applied Physics*, 93(6):3605, 2003.

[16] D.J. Griffiths. *Introduction to Quantum Mechanics, 2nd Edition*. Pearson Prentice Hall, 2005.

[17] A.T. Healy, B.W. Boudouris, C.D. Frisbie, M.A. Hillmyer, and D.A. Blank. Intramolecular Exciton Diffusion in Poly(3-hexylthiophene). *The Journal of Physical Chemistry Letters*, 4:3445–3449, 2013.

[18] W.A. Luhman and R.J. Holmes. Enhanced exciton diffusion in an organic photovoltaic cell by energy transfer using a phosphorescent sensitizer. *Applied Physics Letters*, 94(15):153304, 2009.

[19] R.R. Lunt, N.C. Giebink, A.A. Belak, J.B. Benziger, and S.R. Forrest. Exciton diffusion lengths of organic semiconductor thin films measured by spectrally resolved photoluminescence quenching. *Journal of Applied Physics*, 105(5):053711, 2009.

[20] P. Peumans, A. Yakimov, and S.R. Forrest. Small molecular weight organic thin-film photodetectors and solar cells. *Journal of Applied Physics*, 93(7):3693, 2003.

[21] G. Yu, J. Gao, J.C. Hummelen, F. Wudl, and A.J. Heeger. Polymer photovoltaic cells: enhanced efficiencies via a network of internal donor-acceptor heterojunctions. *Science*, 270(5243):1789–1791, 1995.

[22] P. Peumans, S. Uchida, and S.R. Forrest. Efficient bulk heterojunction photovoltaic cells using small-molecular-weight organic thin films. *Nature*,

425(6954):158–62, 2003.

[23] D.A. McQuarrie and J.D. Simon. *Physical Chemistry: A Molecular Approach.* University Science Books, 1997.

[24] D.C. Harris and M.D. Bertolucci. *Symmetry and Spectroscopy: An Introduction to Vibrational and Electronic Spectroscopy.* Dover Publications, Inc., 1978.

[25] J.R. Henderson, M. Muramoto, and R.A. Willett. Harmonic FranckCondon Overlap Integrals Including Displacement of Normal Coordinates. *The Journal of Chemical Physics*, 41(2):580, 1964.

[26] S. Karabunarliev, M. Baumgarten, E.R. Bittner, and K. Mullen. Rigorous Franck-Condon absorption and emission spectra of conjugated oligomers from quantum chemistry. *The Journal of Chemical Physics*, 113(24):11372, 2000.

[27] S.T. Thornton and A. Rex. *Modern Physics for Scientists and Engineers.* Thomson Learning, Inc., 2002.

[28] W.T. Silfvast. *Laser Fundamentals.* Cambridge University Press, 1996.

[29] S. Chandrasekhar. Stochastic problems in physics and astronomy. *Reviews of Modern Physics*, 15, 1943.

[30] D.G. Zill. *A First Course in Differential Equations with Modeling Applications.* Brooks Cole Thomson Learning, 2005.

[31] M.K. Keane. *A Very Applied First Course in Partial Differential Equations.* Prentice Hall, 2002.

[32] C. Cohen-Tannoudji, B. Diu, and F. Laloë. *Quantum Mechanics.* John Wiley and

Sons, 2005.

[33] D.L. Dexter. A Theory of Sensitized Luminescence in Solids. *The Journal of Chemical Physics*, 21(5):836, 1953.

[34] A. Olaya-Castro and G. Scholes. Energy transfer from Forster-Dexter theory to quantum coherent light-harvesting. *International Reviews in Physical Chemistry*, 30(1):49–77, 2011.

[35] Th. Förster. 10th Spiers Memorial Lecture. Transfer mechanisms of electronic excitation. *Discussions of the Faraday Society*, 27:7–17, 1959.

[36] Th. Förster. Experimentelle und theoretische Untersuchung des zwischenmolekularen Übergangs von Elektronenanregungsenergie. *Zeitschrift Fur Naturforschung*, 4a:321–327, 1949.

[37] Th. Förster. Zwischenmolekulare Energiewanderung und Fluoreszenz. *Annalen der Physik*, 437(1-2):55–75, 1948.

[38] E.V. Mielczarek, E.S. Greenbaum, and R.S. Knox. *Biological Physics*. Intermolecular Energy Migration and Fluorescence, 148–160. Springer, 1993.

[39] V.M. Agranovich and A.A. Maradudin. *Electronic Excitation Energy Transfer in Condensed Matter*. North-Holland Publishing Company, 1982.

[40] G.D. Scholes and K.P. Ghiggino. Electronic Interactions and Interchromophore Excitation Transfer. *The Journal of Physical Chemistry*, 98(17):4580–4590, 1994.

[41] M. Kasha. Characterization of electronic transitions in complex molecules. *Discussions of the Faraday Society*, 9:14–19, 1950.

[42] J.I. Steinfeld, J.S. Francisco, and W.L. Hase. *Chemical Kinetics and Dynamics Second Edition*. Prentice Hall, 1999.

[43] J.R. Lakowicz. *Principles of Fluorescence Spectroscopy*. Springer, 2006.

[44] D.W. Allen. Holmium oxide glass wavelength standards. *Journal of Research of the National Institute of Standards and Technology*, 112(6):303, 2007.

[45] J.A. Gardecki and M. Maroncelli. Set of Secondary Emission Standards for Calibration of the Spectral Responsivity in Emission Spectroscopy. *Applied Spectroscopy*, 52(9):1179–1189, 1998.

[46] W.H. Melhuish. Absolute spectrofluorometry. *Journal of Research of the National Bureau of Standards*, 76A(6):547–560, 1972.

[47] J. Mooney and P. Kambhampati. Get the Basics Right: Jacobian Conversion of Wavelength and Energy Scales for Quantitative Analysis of Emission Spectra. *The Journal of Physical Chemistry Letters*, 4:3316–3318, 2013.

[48] J.M. Drake, M.L. Lesiecki, and D.M. Camaioni. Photophysics and cis-trans isomerization of DCM. *Chemical Physics Letters*, 113(6):530–534, 1985.

[49] N.P. Wells, B.W. Boudouris, M.A. Hillmyer, and D.A. Blank. Intramolecular Exciton Relaxation and Migration Dynamics in Poly(3-hexylthiophene). *Journal of Physical Chemistry C*, 111(42):15404–15414, 2007.

[50] O. Svelto. *Principle of Lasers Fifth Edition*. Springer, 1998.

[51] B.E.A. Saleh and M.C. Teich. *Fundamentals of Photonics Second Edition*. John Wiley & Sons, Inc., 2007.

[52] H.A. Haus. Mode-locking of lasers. *IEEE Journal of Selected Topics in Quantum Electronics*, 6(6):1173–1185, 2000.

[53] W.P. Boeij. *Ultrafast solvation dynamics explored by nonlinear optical spectroscopy*. PhD thesis, University of Groningen, 1997.

[54] G. Cerullo, S. De Silvestri, V. Magni, and L. Pallaro. Resonators for Kerr-lens mode-locked femtosecond Ti:sapphire lasers. *Optics Letters*, 19(11):807–9, 1994.

[55] J. Zhou, C.P. Huang, M.M. Murnane, and H.C. Kapteyn. Amplification of 26-fs, 2-TW pulses near the gain-narrowing limit in Ti:sapphire. *Optics Letters*, 20(1):64–6, 1995.

[56] J. Zhou, C.P. Huang, C. Shi, M.M. Murnane, and H.C. Kapteyn. Generation of 21-fs millijoule-energy pulses by use of Ti:sapphire. *Optics Letters*, 19(2):126, 1994.

[57] E. Riedle, M. Beutter, S. Lochbrunner, J. Piel, S. Schenkl, S. Spörlein, and W. Zinth. Generation of 10 to 50 fs pulses tunable through all of the visible and the NIR. *Applied Physics B*, 71(3):457–465, 2014.

[58] F. Salin, J. Squier, G. Mourou, and G. Vaillancourt. Multikilohertz Ti:Al_2O_3 amplifier for high-power femtosecond pulses. *Optics Letters*, 16(24):1964–1966, 1991.

[59] J.V. Rudd, G. Korn, S. Kane, J. Squier, G. Mourou, and P. Bado. Chirped-pulse amplification of 55-fs pulses at a 1-kHz repetition rate in a Ti:Al_2O_3 regenerative amplifier. *Optics Letters*, 18(23):2044, 1993.

[60] R.W. Boyd. *Nonlinear Optics*. Elsevier, Inc., 2008.

[61] G. Cerullo and S. De Silvestri. Ultrafast optical parametric amplifiers. *Review of Scientific Instruments*, 74(1):1, 2003.

[62] P.J.M. Johnson, V.I. Prokhorenko, and R.J.D. Miller. Enhanced bandwidth non-collinear optical parametric amplification with a narrowband anamorphic pump. *Optics Letters*, 36(11):2170–2, 2011.

[63] A. Couairon and A. Mysyrowicz. Femtosecond filamentation in transparent media. *Physics Reports*, 441(2-4):47–189, 2007.

[64] S.L. Chin. *Femtosecond Laser Filamentation*. Springer, 2010.

[65] P.J.M. Johnson, V.I. Prokhorenko, and R.J.D. Miller. Stable UV to IR supercontinuum generation in calcium fluoride with conserved circular polarization states. *Optics Express*, 17(24):21488–96, 2009.

[66] A.S. Huss, T. Pappenfus, J. Bohnsack, M. Burand, K.R. Mann, and D.A. Blank. The influence of internal charge transfer on nonradiative decay in substituted terthiophenes. *The Journal of Physical Chemistry A*, 113(38):10202–10, 2009.

[67] C.J. Brabec, S. Gowrisanker, J.J.M. Halls, D. Laird, S. Jia, and S.P. Williams. Polymer-fullerene bulk-heterojunction solar cells. *Advanced Materials*, 22(34):3839–3856, 2010.

[68] S. Hugger, R. Thomann, T. Heinzel, and T. Thurn-Albrecht. Semicrystalline morphology in thin films of poly(3-hexylthiophene). *Colloid & Polymer Science*, 282(8):932–938, 2004.

[69] T.-A. Chen, X. Wu, and R.D. Rieke. Regiocontrolled synthesis of poly(3-alkylthiophenes) mediated by Rieke zinc: their characterization and solid-state properties. *Journal of the American Chemical Society*, 117:233–244, 1995.

[70] Z. Hu, T. Adachi, Y.-G. Lee, R.T. Haws, B. Hanson, R.J. Ono, C.W. Bielawski, V. Ganesan, P.J. Rossky, and D.A. Vanden Bout. Effect of the side-chain-distribution density on the single-conjugated-polymer-chain conformation. *ChemPhysChem*, 14(18):4143–4148, 2013.

[71] Y. Kim, S.A. Choulis, J. Nelson, D.D.C. Bradley, S. Cook, and J.R. Durrant. Device annealing effect in organic solar cells with blends of regioregular poly(3-hexylthiophene) and soluble fullerene. *Applied Physics Letters*, 86(6):063502, 2005.

[72] P. Schilinsky, U. Asawapirom, U. Scherf, M. Biele, and C.J. Brabec. Influence of the Molecular Weight of Poly(3-hexylthiophene) on the Performance of Bulk Heterojunction Solar Cells. *Chemistry of Materials*, 17(8):2175–2180, 2005.

[73] J.-F. Chang, B. Sun, D.W. Breiby, M.M. Nielsen, T.I. Sölling, M. Giles, I. McCulloch, and H. Sirringhaus. Enhanced Mobility of Poly(3-hexylthiophene) Transistors by Spin-Coating from High-Boiling-Point Solvents. *Chemistry of Materials*, 16(23):4772–4776, 2004.

[74] J.-M. Verilhac, G. LeBlevennec, D. Djurado, F. Rieutord, M. Chouiki, J.-P.

Travers, and A. Pron. Effect of macromolecular parameters and processing conditions on supramolecular organisation, morphology and electrical transport properties in thin layers of regioregular poly(3-hexylthiophene). *Synthetic Metals*, 156(11-13):815–823, 2006.

[75] P. Vanlaeke, A. Swinnen, I. Haeldermans, G. Vanhoyland, T. Aernouts, D. Cheyns, C. Deibel, J. D'Haen, P. Heremans, J. Poortmans, and J.V. Manca. P3HT/PCBM bulk heterojunction solar cells: Relation between morphology and electro-optical characteristics. *Solar Energy Materials and Solar Cells*, 90(14):2150–2158, 2006.

[76] C. Groves, O.G. Reid, and D.S. Ginger. Heterogeneity in polymer solar cells: local morphology and performance in organic photovoltaics studied with scanning probe microscopy. *Accounts of Chemical Research*, 43(5):612–20, 2010.

[77] N. Kiriy, E. Jähne, H.-J. Adler, M. Schneider, A. Kiriy, G. Gorodyska, S. Minko, D. Jehnichen, P. Simon, A.A. Fokin, and M. Stamm. One-dimensional aggregation of regioregular polyalkylthiophenes. *Nano Letters*, 3(6):707–712, 2003.

[78] Y.D. Park, H.S. Lee, Y.J. Choi, D. Kwak, J.H. Cho, S. Lee, and K. Cho. Solubility-Induced Ordered Polythiophene Precursors for High-Performance Organic Thin-Film Transistors. *Advanced Functional Materials*, 19(8):1200–1206, 2009.

[79] U. Zhokhavets, T. Erb, H. Hoppe, G. Gobsch, and N. Serdar Sariciftci. Effect of annealing of poly(3-hexylthiophene)/fullerene bulk heterojunction composites on structural and optical properties. *Thin Solid Films*, 496(2):679–682, 2006.

[80] L. Magnani, G. Rumbles, I.D.W. Samuel, K. Murray, S.C. Moratti, A.B. Holmes, and R.H. Friend. Photoluminescence studies of chain interactions in electroluminescent polymers. *Synthetic Metals*, 84:899–900, 1997.

[81] P.E. Shaw, A. Ruseckas, and Ifor D.W. Samuel. Exciton Diffusion Measurements in Poly(3-hexylthiophene). *Advanced Materials*, 20(18):3516–3520, 2008.

[82] S. Trotzky, T. Hoyer, W. Tuszynski, C. Lienau, and J. Parisi. Femtosecond up-conversion technique for probing the charge transfer in a P3HT:PCBM blend via photoluminescence quenching. *Journal of Physics D: Applied Physics*, 42(5):055105, 2009.

[83] C.-X. Sheng, M. Tong, S. Singh, and Z.V. Vardeny. Experimental determination of the charge/neutral branching ratio η in the photoexcitation of π-conjugated polymers by broadband ultrafast spectroscopy. *Physical Review B*, 75(8):085206, 2007.

[84] R. Jakubiak, C.J. Collison, W.C. Wan, L.J. Rothberg, and B.R. Hsieh. Aggregation quenching of luminescence in electroluminescent conjugated polymers. *The Journal of Physical Chemistry A*, 103:2394–2398, 1999.

[85] J. Piris, T.E. Dykstra, A.A. Bakulin, P.H.M. Van Loosdrecht, W. Knulst, M. T. Trinh, J.M. Schins, and L.D.A. Siebbeles. Photogeneration and Ultrafast Dynamics of Excitons and Charges in P3HT/PCBM Blends. *The Journal of Physical Chemistry C*, 113(32):14500–14506, 2009.

[86] R.A. Marsh, J.M. Hodgkiss, S. Albert-Seifried, and R.H. Friend. Effect of annealing on P3HT:PCBM charge transfer and nanoscale morphology probed by ultrafast spectroscopy. *Nano Letters*, 10(3):923–30, 2010.

[87] P.J. Brown, D.S. Thomas, A. Köhler, J.S. Wilson, J.-S. Kim, C.M. Ramsdale, H. Sirringhaus, and R.H. Friend. Effect of interchain interactions on the absorption and emission of poly(3-hexylthiophene). *Physical Review B*, 67(6):064203, 2003.

[88] J. Zhao, A. Swinnen, G. Van Assche, J. Manca, D. Vanderzande, and B. Van Mele. Phase diagram of P3HT/PCBM blends and its implication for the stability of morphology. *The Journal of Physical Chemistry B*, 113(6):1587–91, 2009.

[89] B.W. Boudouris, C.D. Frisbie, and M.A. Hillmyer. Nanoporous Poly(3-alkylthiophene) Thin Films Generated from Block Copolymer Templates. *Macromolecules*, 41(1):67–75, 2008.

[90] S. Malik and A.K. Nandi. Crystallization mechanism of regioregular poly(3-alkyl thiophene)s. *Journal of Polymer Science Part B: Polymer Physics*, 40:2073–2085, 2002.

[91] R. Noriega, J. Rivnay, K. Vandewal, F.P.V. Koch, N. Stingelin, P. Smith, M.F. Toney, and A. Salleo. A general relationship between disorder, aggregation and charge transport in conjugated polymers. *Nature Materials*, 12(11):1038–1044, 2013.

[92] F.C. Spano. The spectral signatures of Frenkel polarons in H-and J-aggregates. *Accounts of Chemical Research*, 43(3):429–439, 2010.

[93] E.G. McRae and M. Kasha. Enhancement of Phosphorescence Ability upon Aggregation of Dye Molecules. *The Journal of Chemical Physics*, 28(4):721, 1958.

[94] J. Clark, C. Silva, R. Friend, and F. Spano. Role of Intermolecular Coupling in the Photophysics of Disordered Organic Semiconductors: Aggregate Emission in Regioregular Polythiophene. *Physical Review Letters*, 98(20):206406, 2007.

[95] F.C. Spano. Absorption in regio-regular poly(3-hexyl)thiophene thin films: Fermi resonances, interband coupling and disorder. *Chemical Physics*, 325(1):22–35, 2006.

[96] S.T. Turner, P. Pingel, R. Steyrleuthner, E.J.W. Crossland, S. Ludwigs, and D. Neher. Quantitative Analysis of Bulk Heterojunction Films Using Linear Absorption Spectroscopy and Solar Cell Performance. *Advanced Functional Materials*, 21(24):4640–4652, 2011.

[97] J. Guo, H. Ohkita, H. Benten, and S. Ito. Near-IR femtosecond transient absorption spectroscopy of ultrafast polaron and triplet exciton formation in polythiophene films with different regioregularities. *Journal of the American Chemical Society*, 131(46):16869–80, 2009.

[98] A.L. Ayzner, S.C. Doan, B. Tremolet de Villers, and B.J. Schwartz. Ultrafast Studies of Exciton Migration and Polaron Formation in Sequentially Solution-Processed Conjugated Polymer/Fullerene Quasi-Bilayer Photovoltaics. *The Journal of Physical Chemistry Letters*, 3:2281–2287, 2012.

[99] B. Grévin, P. Rannou, R. Payerne, A. Pron, and J.-P. Travers. Scanning Tunneling Microscopy Investigations of Self-Organized Poly(3-hexylthiophene) Two-Dimensional Polycrystals. *Advanced Materials*, 15(11):881–884, 2003.

[100] B. Grévin, P. Rannou, R. Payerne, A. Pron, and J.P. Travers. Multi-scale scanning tunneling microscopy imaging of self-organized regioregular poly(3-hexylthiophene) films. *The Journal of Chemical Physics*, 118(15):7097–7102, 2003.

[101] P.W.M. Blom, V.D. Mihailetchi, L.J. Anton Koster, and D.E. Markov. Device Physics of Polymer:Fullerene Bulk Heterojunction Solar Cells. *Advanced Materials*, 19(12):1551–1566, 2007.

[102] J. Peet, A.J. Heeger, and G.C. Bazan. "Plastic" solar cells: self-assembly of bulk heterojunction nanomaterials by spontaneous phase separation. *Accounts of Chemical Research*, 42(11):1700–8, 2009.

[103] C. Groves, R.A. Marsh, and N.C. Greenham. Monte Carlo modeling of geminate recombination in polymer-polymer photovoltaic devices. *The Journal of Chemical Physics*, 129(11):114903, 2008.

[104] J. Brazard, R.J. Ono, C.W. Bielawski, P.F. Barbara, and D.A Vanden Bout. Mimicking conjugated polymer thin-film photophysics with a well-defined triblock copolymer in solution. *The Journal of Physical Chemistry B*, 117(16):4170–6, 2013.

[105] I.D.W. Samuel, L. Magnani, G. Rumbles, K. Murray, B.M. Stone, S.C. Moratti, and A.B. Holmes. Photoluminescence in poly(3-hexylthiophene). *SPIE*, 3145:163,

1997.

[106] O. Inganäs, W.R. Salaneck, J.E. Österholm, and J. Laakso. Thermochromic and solvatochromic effects in poly(3-hexylthiophene). *Synthetic Metals*, 22:395–406, 1988.

[107] G. Rumbles, I.D.W. Samuel, and L. Magnani. Chromism and luminescence in regioregular poly(3-dodecylthiophene). *Synthetic Metals*, 76:47–51, 1996.

[108] T. Yamamoto, D. Komarudin, M. Arai, B.-L. Lee, H. Suganuma, N. Asakawa, Y. Inoue, K. Kubota, and S. Sasaki. Extensive Studies on π-Stacking of Poly(3-alkylthiophene-2,5-diyl)s and Poly(4-alkylthiazole-2,5-diyl)s by Optical Spectroscopy, NMR Analysis, Light Scattering Analysis, and X-ray Crystallography. *Journal of the American Chemical Society*, 120:2047–2058, 1998.

[109] J. Brandrup, E.H. Immergut, and E. Grulke. *Polymer Handbook*. John Wiley and Sons, Inc., 1999.

[110] S. Cook, A. Furube, and R. Katoh. Analysis of the excited states of regioregular polythiophene P3HT. *Energy & Environmental Science*, 1(2):294, 2008.

[111] F.C. Spano. Analysis of the UV/Vis and CD spectral line shapes of carotenoid assemblies: spectral signatures of chiral H-aggregates. *Journal of the American Chemical Society*, 131(12):4267–78, 2009.

[112] H. Yamagata and F.C. Spano. Interplay between intrachain and interchain interactions in semiconducting polymer assemblies: the HJ-aggregate model. *The Journal of Chemical Physics*, 136(18):184901, 2012.

[113] J.W. Blatchford, S.W. Jessen, L. Lin, T.L. Gustafson, D. Fu, H. Wang, T.M. Swager, A.G. MacDiarmid, and A.J. Epstein. Photoluminescence in pyridine-based polymers: Role of aggregates. *Physical Review B*, 54(13):9180–9189, 1996.

[114] S. Quan, F. Teng, Z. Xu, L. Qian, Y. Hou, Y. Wang, and X. Xu. Solvent and concentration effects on fluorescence emission in MEH-PPV solution. *European Polymer Journal*, 42(1):228–233, 2006.

[115] A. Feltrin and A. Freundlich. Material Considerations for Terawatt Level Deployment of Photovoltaics. *Renewable Energy*, 33(2):180–185, 2008.

[116] T.K. Todorov, J. Tang, S. Bag, O. Gunawan, T. Gokmen, Y. Zhu, and D.B. Mitzi. Beyond 11% Efficiency: Characteristics of State-of-the-Art $Cu_2ZnSn(S,Se)_4$ Solar Cells. *Advanced Energy Materials*, 3(1):34–38, 2013.

[117] Q. Guo, H.W. Hillhouse, and R. Agrawal. Synthesis of Cu_2ZnSnS_4 Nanocrystal Ink and its use for Solar Cells. *Journal of the American Chemical Society*, 131:11672–11673, 2009.

[118] C. Steinhagen, M.G. Panthani, V. Akhavan, B. Goodfellow, B. Koo, and B.A. Korgel. Synthesis of Cu_2ZnSnS_4 Nanocrystals for use in Low-Cost Photovoltaics. *Journal of the American Chemical Society*, 131(35):12554–12555, 2009.

[119] Q. Guo, G.M. Ford, W.-C. Yang, B.C. Walker, E.A. Stach, H.W. Hillhouse, and R. Agrawal. Fabrication of 7.2% Efficient CZTSSe Solar Cells Using CZTS Nanocrystals. *Journal of the American Chemical Society*, pages 17384–17386, 2010.

[120] A. Khare, A.W. Wills, L.M. Ammerman, D.J. Norris, and E.S. Aydil. Size Control and Quantum Confinement in Cu_2ZnSnS_4 Nanocrystals. *Chemical Communication*, 47(42):11721–11723, 2011.

[121] B. Flynn, W. Wang, C.-H. Chang, and G.S. Herman. Microwave Assisted Synthesis of Cu_2ZnSnS_4 Colloidal Nanoparticle Inks. *Physica Status Solidi A*, 209(11):2186–2194, 2012.

[122] B. Shin, O. Gunawan, Y. Zhu, N.A. Bojarczuk, S.J. Chey, and S. Guha. Thin Film Solar Cell with 8.4% Power Conversion Efficiency using an Earth-Abundant Cu_2ZnSnS_4 Absorber. *Progress in Photovoltaics*, 21:72–76, 2013.

[123] K. Tanaka, Y. Miyamoto, H. Uchiki, K. Nakazawa, and H. Araki. Donor-Acceptor Pair Recombination Luminescence from Cu_2ZnSnS_4 Bulk Single Crystals. *Physica Status Solidi A*, 203(11):2891–2896, 2006.

[124] J. Paier, R. Asahi, A. Nagoya, and G. Kresse. Cu_2ZnSnS_4 as a Potential Photovoltaic Material: A hybrid Hartree-Fock Density Functional Theory Study. *Physical Review B*, 79(11):1–8, 2009.

[125] C. Persson. Electronic and optical properties of Cu_2ZnSnS_4 and $Cu_2ZnSnSe_4$. *Journal of Applied Physics*, 107(5):053710, 2010.

[126] A. Khare, B. Himmetoglu, M. Cococcioni, and E.S. Aydil. First Principles Calculation of the Electronic Properties and Lattice Dynamics of $Cu_2ZnSn(S_{1-x}Se_x)_4$. *Journal of Applied Physics*, 111(12):123704, 2012.

[127] A.J. Nozik. Spectroscopy and Hot Electron Relaxation Dynamics in Semiconductor Quantum Wells and Quantum Dots. *Annual Review of Physical Chemistry*, 52:193–231, 2001.

[128] S. Kaniyankandy, S. Rawalekar, S. Verma, D.K. Palit, and H.N. Ghosh. Charge Carrier Dynamics in Thiol Capped CdTe Quantum Dots. *Physical Chemistry Chemical Physics*, 12(16):4210–4216, 2010.

[129] V.I. Klimov. Optical Nonlinearities and Ultrafast Carrier Dynamics in Semiconductor Nanocrystals. *Journal of Physical Chemistry B*, 104:6112–6123, 2000.

[130] M. Sanz, M.A. Correa-Duarte, L.M. Liz-Marzán, and A. Douhal. Femtosecond Dynamics of CdTe Quantum Dots in Water. *Journal of Photochemistry and Photobiology A*, 196(1):51–58, 2008.

[131] T. Gershon, B. Shin, N. Bojarczuk, T. Gokmen, S. Lu, and S. Guha. Photoluminescence characterization of a high-efficiency Cu2ZnSnS4 device. *Journal of Applied Physics*, 114(15):154905, 2013.

[132] M.V. Martínez-Díaz, G. de la Torre, and T. Torres. Lighting porphyrins and phthalocyanines for molecular photovoltaics. *Chemical Communications*, 46(38):7090–108, 2010.

[133] H. Imahori and S. Fukuzumi. Porphyrin- and Fullerene-Based Molecular Photovoltaic Devices. *Advanced Functional Materials*, 14(6):525–536, 2004.

[134] D. Gust, T.A. Moore, and A.L. Moore. Solar fuels via artificial photosynthesis. *Accounts of Chemical Research*, 42(12):1890–8, 2009.

[135] C. Borek, K. Hanson, P.I. Djurovich, M.E. Thompson, K. Aznavour, R. Bau, Y. Sun, S.R. Forrest, J. Brooks, L. Michalski, and J. Brown. Highly Efficient, Near-Infrared Electrophosphorescence from a PtMetalloporphyrin Complex. *Angewandte Chemie*, 119(7):1127–1130, 2007.

[136] T. Bessho, S.M. Zakeeruddin, C.-Y. Yeh, E. W.-G. Diau, and M. Grätzel. Highly efficient mesoscopic dye-sensitized solar cells based on donor-acceptor-substituted porphyrins. *Angewandte Chemie (International ed. in English)*, 49(37):6646–9, 2010.

[137] F. Gao, Y. Wang, D. Shi, J. Zhang, M. Wang, X. Jing, R. Humphry-Baker, P. Wang, S.M. Zakeeruddin, and M. Grätzel. Enhance the optical absorptivity of nanocrystalline TiO2 film with high molar extinction coefficient ruthenium sensitizers for high performance dye-sensitized solar cells. *Journal of the American Chemical Society*, 130(32):10720–8, 2008.

[138] W.M. Campbell, K.W. Jolley, P. Wagner, K. Wagner, P.J. Walsh, K.C. Gordon, L. Schmidt-Mende, M.K. Nazeeruddin, Q. Wang, M. Grtzel, and D.L. Officer. Highly efficient porphyrin sensitizers for dye-sensitized solar cells. *The Journal of Physical Chemistry C*, 111(32):11760–11762, 2007, http://pubs.acs.org/doi/pdf/10.1021/jp0750598.

[139] W.M. Campbell, A.K. Burrell, D.L. Officer, and K.W. Jolley. Porphyrins as light harvesters in the dye-sensitised TiO2 solar cell. *Coordination Chemistry Reviews*, 248(13-14):1363–1379, 2004.

[140] M. Baldo, C. Adachi, and S. Forrest. Transient analysis of organic electrophosphorescence. II. Transient analysis of triplet-triplet annihilation. *Physical Review B*, 62(16):10967–10977, 2000.

[141] I.-W. Hwang, T. Kamada, T. K. Ahn, D. M. Ko, T. Nakamura, A. Tsuda, A. Osuka, and D. Kim. Porphyrin boxes constructed by homochiral self-sorting assembly: optical separation, exciton coupling, and efficient excitation energy migration. *Journal of the American Chemical Society*, 126(49):16187–98, 2004.

[142] C.M. Marian. Spin-orbit coupling and intersystem crossing in molecules. *Wiley Interdisciplinary Reviews: Computational Molecular Science*, 2(2):187–203, 2012.

[143] S.P. McGlynn, T. Azumi, and M. Kasha. External Heavy-Atom Spin-Orbital Coupling Effect. V. Absorption Studies of Triplet States. *The Journal of Chemical Physics*, 40(2):507–515, 1964.

[144] J.A. Hinke. *Excited State Dynamics of Metalloporphyrins Utilized in Organic Photovoltaic Devices*. PhD thesis, University of Minnesota, 2013.

[145] S.T. Roberts, C.W. Schlenker, V. Barlier, R.E. McAnally, Y. Zhang, J.N. Mastron, M.E. Thompson, and S.E. Bradforth. Observation of Triplet Exciton Formation in a Platinum-Sensitized Organic Photovoltaic Device. *The Journal of Physical Chemistry Letters*, 2(2):48–54, 2011.

[146] J. Kalinowski, W. Stampor, J. Szmytkowski, M. Cocchi, D. Virgili, V. Fattori, and P. Di Marco. Photophysics of an electrophosphorescent platinum (II) porphyrin in solid films. *The Journal of Chemical Physics*, 122(15):154710, 2005.

[147] M.A. Baldo, D.F. O'Brien, Y. You, A. Shoustikov, S. Sibley, M.E. Thompson, and S.R. Forrest. Highly efficient phosphorescent emission from organic electroluminescent devices. *Nature*, 395(10):151–154, 1998.

[148] T.N. Singh-Rachford and F.N. Castellano. Photon upconversion based on sensitized triplettriplet annihilation. *Coordination Chemistry Reviews*, 254(21-22):2560–2573, 2010.

[149] W. Staroske, M. Pfeiffer, K. Leo, and M. Hoffmann. Single-Step Triplet-Triplet Annihilation: An Intrinsic Limit for the High Brightness Efficiency of Phosphorescent Organic Light Emitting Diodes. *Physical Review Letters*, 98(19):8–11, 2007.

[150] R.C. Kwong, S. Sibley, T. Dubovoy, M. Baldo, S.R. Forrest, and M.E. Thompson. Efficient, Saturated Red Organic Light Emitting Devices Based on Phosphorescent Platinum(II) Porphyrins. *Chemistry of Materials*, 11(12):3709–3713, 1999.

[151] P.E. Keivanidis, F. Laquai, W.F. Robertson, S. Baluschev, J. Jacob, K. Mullen, and G. Wegner. Electron-Exchange-Assisted Photon Energy Up-Conversion in Thin Films of π-Conjugated Polymeric Composites. *The Journal of Physical Chemistry Letters*, 2:1893–1899, 2011.

[152] P.E. Keivanidis, S. Baluschev, G. Lieser, and G. Wegner. Inherent photon energy recycling effects in the up-converted delayed luminescence dynamics of poly(fluorene)-Pt(II)octaethyl porphyrin blends. *ChemPhysChem*, 10(13):2316–26, 2009.

[153] P.E. Keivanidis, S. Baluschev, T. Miteva, G. Nelles, U. Scherf, A. Yasuda, and G. Wegner. Up-Conversion Photoluminescence in Polyfluorene Doped with Metal(II)Octaethyl Porphyrins. *Advanced Materials*, 15(24):2095–2098, 2003.

[154] X. Zhang, E.C. Wasinger, A.Z. Muresan, K. Attenkofer, G. Jennings, J.S. Lindsey, and L.X. Chen. Ultrafast stimulated emission and structural dynamics in nickel porphyrins. *The Journal of Physical Chemistry A*, 111(46):11736–42, 2007.

[155] H.S. Eom, S.C. Jeoung, D. Kim, J.-H. Ha, and Y.-R. Kim. Ultrafast vibrational relaxation and ligand photodissociation/photoassociation processes of nickel (II) porphyrins in the condensed phase. *The Journal of Physical Chemistry A*, 101(20):3661–3669, 1997.

[156] A. Antipas and M. Gouterman. Porphyrins. 44. Electronic States of Co, Ni, Rh, and Pd Complexes. *J. Am Chem. Soc.*, 105(15):4896–4901, 1983.

[157] J. Mezyk, J. Kalinowski, F. Meinardi, and R. Tubino. Triplet exciton interactions in solid films of an electrophosphorescent Pt (II) porphyrin. *Applied Physics Letters*, 86(11):111916, 2005.

[158] E. Engel, K. Leo, and M. Hoffmann. Ultrafast relaxation and excitonexciton annihilation in PTCDA thin films at high excitation densities. *Chemical Physics*, 325(1):170–177, 2006.

[159] M. Inokuti and F. Hirayama. Influence of Energy Transfer by the Exchange Mechanism on Donor Luminescence. *The Journal of Chemical Physics*, 43(6):1978, 1965.

Appendix A

Coding Examples

This appendix contains examples of code used throughout this thesis. When using Maple it was often difficult or impossible to transfer plain-text code and, as such, code is presented as figures. MATLAB code is presented in plain-text with supplementary figures as necessary.

A.1 Calculating Franck-Condon Factors

Franck-Condon factors were calculated as described by Henderson.[25] The integrals of Hermite polynomials were completed using Maple and the results are presented below. The first page sets up the factors and integrals needed, while the second page calculates the first seven Franck-Condon factors for a given set of parameters and illustrates an absorption spectrum made by multiplying Lorentzian lineshapes by the associated Franck-Condon factors.

```
> restart; with(orthopoly) : with(plots) :
> alpha := sqrt(wpp); beta := sqrt(wp); delta := alpha/beta; s := (1+δ^2)^(-1/2); c := delta·s; p
    := alpha·Delta/(1+δ^2)^(1/2);
```

$$\alpha := \sqrt{wpp}$$

$$\beta := \sqrt{wp}$$

$$\delta := \frac{\sqrt{wpp}}{\sqrt{wp}}$$

$$s := \frac{1}{\sqrt{1+\frac{wpp}{wp}}}$$

$$c := \frac{\sqrt{wpp}}{\sqrt{wp}\sqrt{1+\frac{wpp}{wp}}}$$

$$p := \frac{\sqrt{wpp}\ \Delta}{\sqrt{1+\frac{wpp}{wp}}} \qquad (1)$$

```
> Np := (n)->sqrt(alpha/(2^n·n!·sqrt(Pi)));
```

$$Np := n \to \sqrt{\frac{\alpha}{2^n\, n!\, \sqrt{\pi}}} \qquad (2)$$

```
> Npp := (n)->sqrt(beta/(2^n·n!·sqrt(Pi)));
```

$$Npp := n \to \sqrt{\frac{\beta}{2^n\, n!\, \sqrt{\pi}}} \qquad (3)$$

```
> II := (n1,n2)->int(H(n2,c·x+s·p)·H(n1,s·x-c·p)·exp(-(x^2+p^2)/2), x=-infinity
    ..infinity)
```

$$II := (n1,n2) \to \int_{-\infty}^{\infty} H(n2, c\,x + s\,p)\, H(n1, s\,x - c\,p)\, e^{-\frac{1}{2}x^2 - \frac{1}{2}p^2}\, dx \qquad (4)$$

```
> R := (n1,n2)->(Npp(n2)·Np(n1)·c/alpha·II(n1,n2))^2
```

$$R := (n1,n2) \to \frac{Npp(n2)^2\, Np(n1)^2\, c^2\, II(n1,n2)^2}{\alpha^2} \qquad (5)$$

Figure A.1: Setting up factors and integrals necessary to calculate Franck-Condon factors in Maple.

Define variables here and then make Franck-Condon factors

```
> w0 := 1600; wp := 100; wpp := 100; Dp := 1.5; Delta := Dp· sqrt(1/wpp) : width := 45; n
      := 6; waxis := Vector(n + 1, i→w0 + (i − 1)·wpp) :
  tempsum := 0 : Lorentp := { } : FC := Vector(n + 1) : Spectrum := 0 :
  for i from 0 to n do
  FC[i + 1] := evalf(simplify(R(0, i))) :
   temp := FC[i + 1]·width / ((w − waxis[i + 1])^2 + width^2);
  Lorentp := Lorentp union {plot(temp, w = w0 − wpp..w0 + (n + 1)·wpp, numpoints = 1000,
      linestyle = dash)};
  Spectrum := Spectrum + temp; od:
  pointplot(waxis, FC);
  display(Lorentp union {plot(Spectrum, w = w0 − wpp..w0 + (n + 1)·wpp, numpoints
      = 1000)}) ;
```

$$w0 := 1600$$
$$wp := 100$$
$$wpp := 100$$
$$Dp := 1.5$$
$$width := 45$$
$$n := 6$$

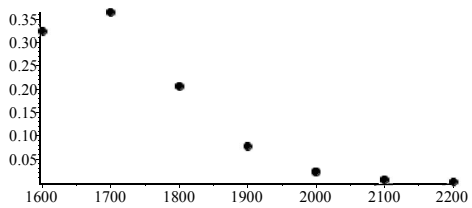

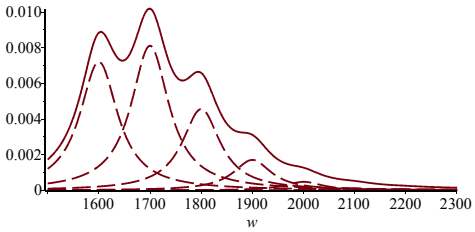

Figure A.2: Calculation of the first 7 Franck-Condon Factors in Maple with a 0-0 frequency of 1600 cm^{-1}, initial and final vibrational spacing of 100 cm^{-1}, and a displacement of the harmonic oscillators of $1.5*(\hbar/\omega)^{1/2}$. Absorption spectrum is simulated with Lorentzian broadening of 45 cm^{-1}

A.2 3D Random Walk

The root mean square (rms) distance for a 3D random walk was found by randomly choosing a direction in 3D space to step and repeating N times. The whole walk was then repeated until the rms distance converged. Walk carried out in MATLAB.

```
%% Start Switches %%%%%%%%%%%%%%%%%%

%Number of Steps
numsteps=1000;

%Number of Runs
numruns=100000;

%Step Size
stepsize=1;

%% End Switches %%%%%%%%%%%%%%%%%%

%% Start Code %%%%%%%%%%%%%%%%%%%%

%start timer
tic

%Initialize some things
xfinal=0;yfinal=0;zfinal=0;d=0;

%Initialize waitbar
waith=waitbar(0,'Randomly walking. Please Wait.');

%Number of runs for loop
for j=1:numruns

    %initiaize starting location
    x=0; y=0; z=0;

    %Random walk for loop
    for i=1:numsteps
        %Get randomm numbers which will define direction of move
        xrand=rand-.5; yrand=rand-.5; zrand=rand-.5;

        %Calculate normalization constant
        normconst=sqrt(xrand^2+yrand^2+zrand^2);

        %Normalize each random number to total length, multiply by step size, and add to old
        x=x+xrand/normconst*stepsize;
        y=y+yrand/normconst*stepsize;
        z=z+zrand/normconst*stepsize;
    end

    %final distance from origin
```

```
    d(j)=x^2+y^2+z^2;

    %Update waitbar
    waitbar(j/numruns,waith);
end

delete(waith);

Ldsq=mean(d);
Ldsqstd=std(d);

%plot some things
figure(1)
hold off
plot(d,'k.')
hold on
hline(Ldsq,'k:');

%calculate root mean square distance
Ld=sqrt(Ldsq)

disp(['Average distance squared from origin was ' num2str(Ldsq) ...
    ' with a stdev of ' num2str(Ldsqstd) '.']);
disp(['RMS distance from orgin was ' num2str(Ld) '.']);

%stop timer
toc
```

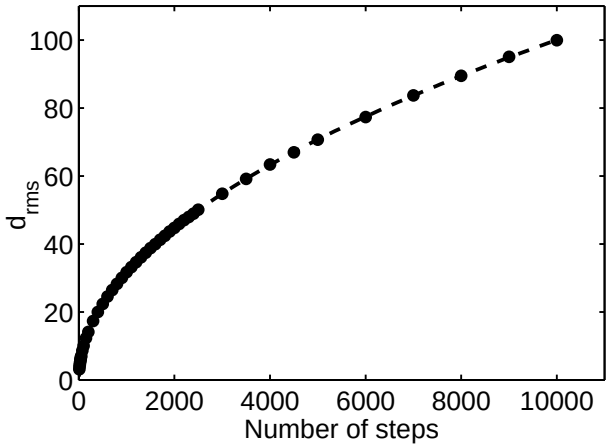

Figure A.3: Simulated d_{rms} (dots) for a three dimensional random walk with a step size $l = 1$ and varying number of steps, n. The dashed line is the theoretical result, $d_{rms} = \sqrt{nl^2}$.

A.3 Solution to the Diffusion Equation

A solution to the diffusion equation is proposed and it is shown to solve the diffusion equation and obey the boundary and initial conditions. It is then shown to be a probability density function and the expectation value of the displacement and the square of the displacement are found. The first figure is for one dimension, while the second is for three dimensions.

```
> restart;assume(d,'positive');assume(t,'positive');
```

'Guess' solution to diffusion equation

```
> w:=1/sqrt(4*d*Pi*t)*exp(-x^2/4/t/d);
```

$$w := \frac{1}{2}\,\frac{e^{-\frac{1}{4}\,\frac{x^2}{t\sim d\sim}}}{\sqrt{d\sim \pi\, t\sim}} \qquad (1)$$

Check Diffusion Equation

```
> simplify(diff(w,t)-d*diff(w,x,x));
```

$$0 \qquad (2)$$

Check that solution is a probability density function

```
> int(w,x=-infinity..infinity);
```

$$1 \qquad (3)$$

Boundary Condition; w(infinity)=0

```
> limit(w,x=infinity);
```

$$0 \qquad (4)$$

Boundary Condition; w'(infinity)=0

```
> limit(diff(w,x),x=infinity);
```

$$0 \qquad (5)$$

Initial Condition; Delta function at zero

```
> plot(eval(w,[d=1,t=.0001]),x=-1..1);
```

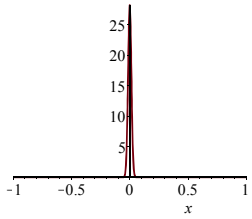

Expectation value of x:

```
> expx:=int(x*w,x=-infinity..infinity);
```

$$expx := 0 \qquad (6)$$

Expectation value of x^2:

```
> expx2:=int(x^2*w,x=-infinity..infinity);
```

$$expx2 := 2\, t\sim d\sim \qquad (7)$$

Figure A.4: Solution to the 1D diffusion equation in Maple as well as the expectation value of the displacement and the displacement squared.

```
> restart; with(plots): assume(d,'positive'); assume(t,'positive');
```

'Guess' solution to diffusion equation

```
> w:=1/(4*Pi*d*t)^(3/2)*exp(-r^2/4/d/t);
```

$$w := \frac{1}{16}\,\frac{\sqrt{4}\,e^{-\frac{1}{4}\,\frac{r^2}{d\sim t\sim}}}{(\pi\, d\sim t\sim)^{3/2}} \qquad (1)$$

Check Diffusion Equation

```
> simplify(diff(w,t)-d*1/r^2*diff(r^2*diff(w,r),r));
```

$$0 \qquad (2)$$

Initial Condition, Delta function at zero

```
> plot(eval(w,[t=0.001,d=1]),r=-5..5,axes=framed);
```

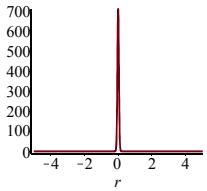

Boundary Condition; w(infinity)=0

```
> limit(w,r=infinity);
```

$$0 \qquad (3)$$

Boundary Condition; w'(infinity)=0

```
> limit(diff(w,r),r=infinity);
```

$$0 \qquad (4)$$

Check that this is a probablity density function

```
> simplify(int(w*r^2,r=-infinity..infinity)*2*Pi);
```

$$1 \qquad (5)$$

Expectation value of r:

```
> exr:=simplify(int(w*r*r^2,r=-infinity..infinity)*2*Pi);
```

$$exr := 0 \qquad (6)$$

Expectation value of r^2:

```
> exr2:=simplify(int(w*r^2*r^2,r=-infinity..infinity)*2*Pi);
```

$$exr2 := 6\, d\sim t\sim \qquad (7)$$

Figure A.5: Solution to the 3D diffusion equation in Maple as well as the expectation value of the displacement and the displacement squared.

A.4 Plotting of Modes in an Oscillator

Below is MATLAB code to plot the electric field squared for a series of modes in a cavity with either random phases or locked phases.

```
%% Begin Inputs

%Number of modes (should be odd)
N = 31;

%center wavelength (nm)
lambda = 800;

%cavity length (m)
d = 1;

%time min and max
tmin=-d/3E-8;
tmax=3*d/3E-8;

%number of points in time vector
tnum=1000;
%% End Inputs

%% Begin code

%center frequency and frequency spacing
w0=2*pi*3E-8/(lambda*10^-9);
dw=2*pi*3E-8/(2*d);

%build time vector
t=linspace(tmin,tmax,tnum);

ind=0;
%Build components
for i = -(N-1)/2:(N-1)/2
    ind=ind+1;
    E(ind,:)=exp(1i*((w0+i*dw)*t+rand*2*pi)); %random phase
%     E(ind,:)=exp(1i*((w0+i*dw)*t)); %same phase
end

Esum=sum(E);
Esquared=Esum.*conj(Esum);

figure(1); clf
plot(t,Esquared)
figure(2); clf
plot(t,E)
```

A.5 Creating Phase-Matching Curves for NOPA

Below is MATLAB code to create phase-matching curves for Type-I NOPA in a negative uniaxial crystal such as BBO. The first function (phasematchinganglenl.m) finds the phase-matching angle for a specific signal and pump wavelength. The second function (phasematchingnl.m) uses the first function to find the phase-matching angle for a range of signal wavelengths and a specific pump wavelength. The third function (sellm.m) is simply used to calculate the ordinary and extraordinary indices of refraction for BBO at different wavelengths.

```
function angle=phasematchinganglenl(wlp,wls,thetap)

%function that finds phase matching angle given pump (wlp) and signal (wls)
%wavelengths in nm and the pump angle in degrees (thetap).  Assume Type-I
%phase matching in a negative uniaxial crystal (BBO)


%% INPUTS

%material info (options: 'BBO')
material='BBO';

%initial guess for phase matching angle (degrees)
guess=35;

%% SOME GOOD INFO
%{
We make the decision: wls < wli
note the designation of signal/idler is arbitrary, but in all of our code the 'signal'
has the smaller wavelength

Phase-matching methods (Type I or Type II) for uniaxial crystals:
(Boyd Nonlinear Optics 3rd edition p. 82)
         Positive uniaxial (ne>no)      Negative uniaxial (ne<no)
Type I     pump-o signal-e idler-e        pump-e signal-o idler-o
Type II    pump-o signal-e idler-o        pump-e signal-o idler-e

Sellmeier Equation Explanation: Saleh and Teich Photonics 2nd edition p. 180
%}

%% CODE
```

```
%Change pump angle to radians:
thetap=thetap*pi/180;

%Calculate idler wavelength in nm
wli=1/(1/wlp-1/wls);

%Calculate the required indecies of refraction (ordinary and extraordinary)
nop=sellm(wlp,0,material);
nep=sellm(wlp,1,material);

nos=sellm(wls,0,material);

noi=sellm(wli,0,material);

%Make functions for each overall index of refraction (dependant on theta)
np=@(theta)1/sqrt(cos(theta+thetap)^2/nop^2+sin(theta+thetap)^2/nep^2);
ns=nos;
ni=noi;

%Make overall phase function (see Cerullo & De Silvestri, Rev Sci Instr 74 1 2003, eqn 31):
%The argument of the first cosine is solving Cerullo's 31b for Omega.
pmf=@(theta)abs( ni/wli*cos(asin(np(theta)/ni*wli/wlp*sin(thetap))) + ns/wls ...
    - np(theta)/wlp*cos(thetap) );

%Change initial guess to radians:
guess=guess*pi/180;

%Run fminsearch:
options = optimset('Display','none','MaxIter',1000,'TolFun',1e-40,'TolX',1e-40);
angle=fminsearch(pmf,guess,options)*180/pi;
```

```
function data = phasematchingnl(wlp,wlsmm,thetap)

%function to create a phase matching plot given pump wl (wlp) and a min/max
%signal wl (wlsmm) in nm and the pump angle in degrees

%% INPUTS

%signal wavelength step size (in nm)
wlsstep=2;

%what to plot (0=signal,idler; 1=signal; 2=signal with opposite axes)
plotswt=1;
%% CODE

%get min and max out of wlsmm
wlsmin=wlsmm(1);wlsmax=wlsmm(2);

%make wavelength vector
wls=[wlsmin:wlsstep:wlsmax]';

%number of wavelength elements
wlsn=size(wls,1);

%calculate idler wavelength
wli=1./(1/wlp*ones(wlsn,1)-1./wls);

%calculate phase matching angle
for i=1:wlsn
    angle(i)=phasematchinganglenl(wlp,wls(i),thetap);
end

%make output matrix
data=[angle' wls wli];

%create matricies for plots
signal=[angle' wls];idler=[angle' wli];

signal2=[wls angle'];

%plots:
if plotswt==0
    ep(signal,idler);
    xlabel('Angle (degrees)');
    ylabel('Wavelength (nm)');
elseif plotswt==1
    ep(signal)
    xlabel('Angle (degrees)');
    ylabel('Wavelength (nm)');
elseif plotswt==2
    ep(signal2)
    xlabel('Wavelength (nm)');
    ylabel('Angle (degrees)');
end
```

```
%% Function to calculate index of refraction in a material
%Inputs: wl - wavelength (in nm)
%        eo - axis (0=ordinary; 1=extraordinary)
%        material - string giving material (options: 'BBO')

function n=sellm(wl,oe,material)

%wl to microns:
wl=wl/1000;

switch material
    case 'BBO'
        if oe==0
            n = sqrt(2.7359+0.01878/(wl^2-0.01822)-0.01354*wl^2);
        elseif oe==1
            n = sqrt(2.3753+0.01224/(wl^2-0.01667)-0.01516*wl^2);
        end
end
```

A.6 Fitting Data to a Series of Gaussians

Below is MATLAB code to fit a set of data to a series of Gaussians as well as some other options. The first function is the optimization function. The next three functions are examples of models used in the optimization. The first model creates a series of Gaussians where each Gaussian is given a weight, center, FWHM, and y-offset. There is an option to give all the Gaussians the same width. The second model is similar to the first except only the center of the first Gaussian is given. Each subsequent Gaussian is a set distance from the previous Gaussian. The third model is similar to the first model with the addition of an external data set with a given weight.

```
% Fitting full frequency data to a series of gaussians
% Written by Tom Pundsack 20130904

% I need two functions to do this.  The function that defines the fit
% and the function that optimizes the fit to the data.

% This is the function that does the optimization.

function out=ffgausopt(data,ig)

%% Start Inputs

%Optimize window
optmin=1.5;
optmax=2.6;

%Step size for returned fit
fitstep=.003;

%Number of optimize iterations
optits=300;

%Display of optimize steps ('iter' or 'final' or 'none')
dispsw='iter';

%Confidence interval reported (commonly 95 or 68.2)
confint=95;

%What Model to use
modelnum=4;
```

```
%% End Inputs

%% Start Code

%Find indicies for optimize window in data
optmini=nearestvaluei(data(:,1)',optmin);
optmaxi=nearestvaluei(data(:,1)',optmax);

%cut data to optimize window
optdata=data(optmini:optmaxi,:);

%Set up optimize options
options=statset('Display',dispsw,'MaxIter',optits,'TolFun',1e-40,'TolX',1e-40);

% eval(['ffgausmodel' num2str(modelnum) '([ig 0],optdata(:,1))']);epo(optdata)
% pause

%Run optimization
eval(['[fitpar,resids,jacob,covar,mse]=nlinfit(optdata(:,1),optdata(:,2),@ffgausmodel' ...
num2str(modelnum) ',ig,options);']);

%Determine the confidence intervals
fitpar_err=nlparci(fitpar,resids,jacob,(1-(0.01*confint)));

%Redo the fit on the original axis to calculate the residual
eval(['fitoriginal=ffgausmodel' num2str(modelnum) '([fitpar],optdata(:,1));']);
resid=sum((fitoriginal-optdata(:,2)).^2);

%Redo fit on a new time axis to have a nice smooth fit for plotting purposes
fitt=[min(data(:,1)):fitstep:max(data(:,1))]';
eval(['fitout=[fitt ffgausmodel' num2str(modelnum) '([fitpar 0],fitt)];']);


%Plot things
plot(data(:,1),data(:,2),'color',WhatColor(3,1))
xlim([optmin-(optmax-optmin)*.05,optmax+(optmax-optmin)*.05])
vline(optmin);vline(optmax)

%Make output
parameters=[optmin optmax confint];
out={fitpar,fitpar_err,fitout,data,resid,ig,parameters,clock};
eval([inputname(1) '_fitcell=out;'])

%Ask if the user wants to save
savesw=input('Save fit variables (will overwrite)? (no=0, yes=1): ');

%Save if requested
if savesw==1
    save([inputname(1) '_fitcell.mat'],[inputname(1) '_fitcell'])
    save([inputname(1) '_fitpar.dat'],'fitpar','-ascii','-tabs')
    disp(['save of ' inputname(1) '_fitpar.dat complete']);
    save([inputname(1) '_fit.dat'],'fitout','-ascii','-tabs')
    disp(['save of ' inputname(1) '_fit.dat complete']);
    save([inputname(1) '_fitconf.dat'],'fitpar_err','-ascii','-tabs')
    disp(['save of ' inputname(1) '_fitconf.dat complete']);
end
%% End Code
```

```
% Fitting full frequency data to a series of gaussians
% Written by Tom Pundsack 20130904

% I need two functions to do this.  The function that defines the fit
% and the function that optimizes the fit to the data.

% This is the function that makes the fit.

% Model 1: Given E00, E01, E02, etc.

function yfitout=ffgausmodel1(inputs,xin)

%output: yfitout - y values of the fit
%input: inputs - array of fitting parameters (only put in parameters that
% are not held constant)
%       xin - array of x values

%% Start Input

%number of gaussians
ngaus=3;

%switch to optimize weights of exponentials (1=optimize; 0=don't optimize)
gausweightsw=[1 1 1];

%weights if they are held constant (if they are optimized, these values are ignored)
gausweight=[0 0 0];

%switch to opimize gaus center (1=optimize; 0=don't optimize)
gauscentersw=[1 1 1];

%gaus centers if they are held constant (if they are optimized, these values are ignored)
gauscenter=[0 0 0];

%switch for single fwhm (1=single fwhm; 0=different fwhm for each gaussian)
gausfwhmsnglsw=1;

%switch to optimize gaus fwhm (1=optimize; 0=don't optimize)
gausfwhmsw=[1];

%gaus fwhm if they are held constant (if they are optimized, these values are ignored)
gausfwhm=[0];

%switch to optimize y offset (1=optimize; 0=don't optimize)
gausyoffsetsw=[0 0 0];

%y offset if they are held constant (if they are optimized, these values are ignored)
gausyoffset=[0 0 0];

%

%% End Input


%% Start Main Code

%Check if input length is correct
if gausfwhmsnglsw==0 %all different fwhm
```

```
    if length(inputs)~=min(sum(gausweightsw),ngaus)+min(sum(gauscentersw),ngaus)+ ...
     min(sum(gausfwhmsw),ngaus)+min(sum(gausyoffsetsw),ngaus) && ...
     length(inputs)-1~=min(sum(gausweightsw),ngaus)+min(sum(gauscentersw),ngaus)+ ...
     min(sum(gausfwhmsw),ngaus)+min(sum(gausyoffsetsw),ngaus)
        disp('Input vector wrong size')
    end
elseif gausfwhmsnglsw==1 %all same fwhm
    if length(inputs)~=min(sum(gausweightsw),ngaus)+min(sum(gauscentersw),ngaus)+ ...
     gausfwhmsw(1)+min(sum(gausyoffsetsw),ngaus) && ...
     length(inputs)-1~=min(sum(gausweightsw),ngaus)+min(sum(gauscentersw),ngaus)+ ...
     gausfwhmsw(1)+min(sum(gausyoffsetsw),ngaus)
        disp('Input vector wrong size')
    end
end

%First thing is to define variables if they are optimized or held constant
%Also need to keep track of where we are in the inputs vector
%(start at 1 and iterate each time you get a number)
inputsindex=1;

%Weights
for i=1:ngaus
    if gausweightsw(i)==1
        gausweight(i)=inputs(inputsindex);
        inputsindex=inputsindex+1;
        %otherwise keep definition above
    end
end

%Centers
for i=1:ngaus
    if gauscentersw(i)==1
        gauscenter(i)=inputs(inputsindex);
        inputsindex=inputsindex+1;
        %otherwise keep definition above
    end
end

%FWHM
if gausfwhmsnglsw==0 %different FWHM's
    for i=1:ngaus
        if gausfwhmsw(i)==1
            gausfwhm(i)=inputs(inputsindex);
            inputsindex=inputsindex+1;
            %otherwise keep definition above
        end
    end
elseif gausfwhmsnglsw==1 %same FWHMS's
    if gausfwhmsw(1)==1
        for i=1:ngaus
            gausfwhm(i)=inputs(inputsindex); %all fwhm equal inputted fwhm
        end
        inputsindex=inputsindex+1;
    else
        for i=1:ngaus
            gausfwhm(i)=gausfwhm(1); %all fwhm equal constant fwhm above
        end
    end
end
```

```
%Y offset
for i=1:ngaus
    if gausyoffsetsw(i)==1
        gausyoffset(i)=inputs(inputsindex);
        inputsindex=inputsindex+1;
        %otherwise keep definition above
    end
end

%Check fitting parameters (this should be commented out)
% gausweight
% gauscenter
% gausfwhm
% gausyoffset

%Build gaussians
for i=1:ngaus
    fitcomp(:,i)=sqrt(gausweight(i)^2)*(exp(-(xin-gauscenter(i)).^2* ...
    4*log(2)/gausfwhm(i)^2)+gausyoffset(i));
end

%Sum gaussians to get final fit
yfitout=sum(fitcomp,2);

%Plot if last input was a zero
if length(inputs)==inputsindex
    if inputs(inputsindex)==0
        fighand=figure(1);
        clf
        for i=1:ngaus
            plot(xin,fitcomp(:,i),'--','color',WhatColor(3,3))
            hold on
        end
        plot(xin, yfitout,'color',WhatColor(3,2));
    end
end



%% End Main Code
```

```
% Fitting full frequency data to a series of gaussians
% Written by Tom Pundsack 20130904

% I need two functions to do this.  The function that defines the fit
% and the function that optimizes the fit to the data.

% This is the function that makes the fit.

% Model 2: Given E00, equidistance between E00, E01, E01, etc.

function yfitout=ffgausmodel2(inputs,xin)

%output: yfitout - y values of the fit
%input: inputs - array of fitting parameters (only put in parameters that
% are not held constant)
%       xin - array of x values

%% Start Input

%number of gaussians
ngaus=4;

%switch to optimize weights of exponentials (1=optimize; 0=don't optimize)
gausweightsw=[1 1 1 1];

%weights if they are held constant (if they are optimized, these values are ignored)
gausweight=[0 0 0 0];

%switch to opimize E00 (1=optimize; 0=don't optimize)
E00sw=1;

%E00 if held constant (if optimized, this value is ignored)
E00=0;

%switch to optimize DeltaE (1=optimize; 0=don't optimize)
deltaEsw=1;

%DeltaE if held constant (if optimized, this value is ignored)
deltaE=0;

%switch for single fwhm (1=single fwhm; 0=different fwhm for each gaussian)
gausfwhmsnglsw=1;

%switch to optimize gaus fwhm (1=optimize; 0=don't optimize)
gausfwhmsw=[1];

%gaus fwhm if they are held constant (if they are optimized, these values are ignored)
gausfwhm=[0];

%switch to optimize y offset (1=optimize; 0=don't optimize)
gausyoffsetsw=[0 0 0 0];

%y offset if they are held constant (if they are optimized, these values are ignored)
gausyoffset=[0 0 0 0];

%

%% End Input
```

```
%% Start Main Code

%Check if input length is correct
if gausfwhmsnglsw==0 %all different fwhm
    if length(inputs)~=min(sum(gausweightsw),ngaus)+E00sw+deltaEsw+ ...
     min(sum(gausfwhmsw),ngaus)+min(sum(gausyoffsetsw),ngaus) && ...
     length(inputs)-1~=min(sum(gausweightsw),ngaus)+E00sw+deltaEsw+ ...
     min(sum(gausfwhmsw),ngaus)+min(sum(gausyoffsetsw),ngaus)
        disp('Input vector wrong size')
    end
elseif gausfwhmsnglsw==1 %all same fwhm
    if length(inputs)~=min(sum(gausweightsw),ngaus)+E00sw+deltaEsw+ ...
     gausfwhmsw(1)+min(sum(gausyoffsetsw),ngaus) && ...
     length(inputs)-1~=min(sum(gausweightsw),ngaus)+E00sw+deltaEsw+ ...
     gausfwhmsw(1)+min(sum(gausyoffsetsw),ngaus)
        disp('Input vector wrong size')
    end
end

%First thing is to define variables if they are optimized or held constant
%Also need to keep track of where we are in the inputs vector
%(start at 1 and iterate each time you get a number)
inputsindex=1;

%Weights
for i=1:ngaus
    if gausweightsw(i)==1
        gausweight(i)=inputs(inputsindex);
        inputsindex=inputsindex+1;
        %otherwise keep definition above
    end
end

%E00
if E00sw==1
    E00=inputs(inputsindex);
    inputsindex=inputsindex+1;
    %otherwise keep definition above
end

%deltaE
if deltaEsw==1
    deltaE=inputs(inputsindex);
    inputsindex=inputsindex+1;
    %otherwise keep definition above
end

%FWHM
if gausfwhmsnglsw==0 %different FWHM's
    for i=1:ngaus
        if gausfwhmsw(i)==1
            gausfwhm(i)=inputs(inputsindex);
            inputsindex=inputsindex+1;
            %otherwise keep definition above
        end
    end
elseif gausfwhmsnglsw==1 %same FWHMS's
```

```
    if gausfwhmsw(1)==1
        for i=1:ngaus
            gausfwhm(i)=inputs(inputsindex); %all fwhm equal inputted fwhm
        end
        inputsindex=inputsindex+1;
    else
        for i=1:ngaus
            gausfwhm(i)=gausfwhm(1); %all fwhm equal constant fwhm above
        end
    end
end


%Y offset
for i=1:ngaus
    if gausyoffsetsw(i)==1
        gausyoffset(i)=inputs(inputsindex);
        inputsindex=inputsindex+1;
        %otherwise keep definition above
    end
end

%Check fitting parameters (this should be commented out)
% gausweight
% gauscenter
% gausfwhm
% gausyoffset

%Build gaussians
for i=1:ngaus
    fitcomp(:,i)=-sqrt(gausweight(i)^2)*(exp(-(xin-(E00+(i-1)*deltaE)).^2* ...
    4*log(2)/gausfwhm(i)^2)+gausyoffset(i));
end

%Sum gaussians to get final fit
yfitout=sum(fitcomp,2);

%Plot if last input was a zero
if length(inputs)==inputsindex
    if inputs(inputsindex)==0
        fighand=figure(1);
        clf
        for i=1:ngaus
            plot(xin,fitcomp(:,i),'--','color',WhatColor(3,3))
            hold on
        end
        plot(xin, yfitout,'color',WhatColor(3,2));
    end
end

%% End Main Code
```

```
% Fitting full frequency data to a series of gaussians
% Written by Tom Pundsack 20130904

% I need two functions to do this.  The function that defines the fit
% and the function that optimizes the fit to the data.

% This is the function that makes the fit.

% Model 3: gaussians and a data set as a component

function yfitout=ffgausmodel3(inputs,xin)

%output: yfitout - y values of the fit
%input: inputs - array of fitting parameters (only put in parameters that
% are not held constant)
%       xin - array of x values

%% Start Input

%number of gaussians
ngaus=3;

%switch to optimize weights of exponentials (1=optimize; 0=don't optimize)
gausweightsw=[1 1 1];

%weights if they are held constant (if they are optimized, these values are ignored)
gausweight=[0 0 0];

%switch to opimize gaus center (1=optimize; 0=don't optimize)
gauscentersw=[1 1 1];

%gaus centers if they are held constant (if they are optimized, these values are ignored)
gauscenter=[0 0 0];

%switch for single fwhm (1=single fwhm; 0=different fwhm for each gaussian)
gausfwhmsnglsw=1;

%switch to optimize gaus fwhm (1=optimize; 0=don't optimize)
gausfwhmsw=[1];

%gaus fwhm if they are held constant (if they are optimized, these values are ignored)
gausfwhm=[0];

%switch to optimize y offset (1=optimize; 0=don't optimize)
gausyoffsetsw=[0 0 0];

%y offset if they are held constant (if they are optimized, these values are ignored)
gausyoffset=[0 0 0];

%File path and name of data to add to fit
fitdatasetpath='c:\Blank\rr000.dat';

%switch to optimize weight of dataset added to fit(1=optimize; 0=don't optimize)
fitdatasetweightsw=1;

%weight of dataset added to fit if held constant (if they are optimized, this value is ignored)
fitdatasetweight=0;
```

```
%

%% End Input


%% Start Main Code

%Check if input length is correct
if gausfwhmsnglsw==0 %all different fwhm
    if length(inputs)~=min(sum(gausweightsw),ngaus)+min(sum(gauscentersw),ngaus)+ ...
     min(sum(gausfwhmsw),ngaus)+min(sum(gausyoffsetsw),ngaus)+fitdatasetweightsw && ...
     length(inputs)-1~=min(sum(gausweightsw),ngaus)+min(sum(gauscentersw),ngaus)+ ...
     min(sum(gausfwhmsw),ngaus)+min(sum(gausyoffsetsw),ngaus)+fitdatasetweightsw
        disp('Input vector wrong size')
    end
elseif gausfwhmsnglsw==1 %all same fwhm
    if length(inputs)~=min(sum(gausweightsw),ngaus)+min(sum(gauscentersw),ngaus)+ ...
     gausfwhmsw(1)+min(sum(gausyoffsetsw),ngaus)+fitdatasetweightsw && ...
     length(inputs)-1~=min(sum(gausweightsw),ngaus)+min(sum(gauscentersw),ngaus)+ ...
     gausfwhmsw(1)+min(sum(gausyoffsetsw),ngaus)+fitdatasetweightsw
        disp('Input vector wrong size')
    end
end

%First thing is to define variables if they are optimized or held constant
%Also need to keep track of where we are in the inputs vector
%(start at 1 and iterate each time you get a number)
inputsindex=1;

%Weights
for i=1:ngaus
    if gausweightsw(i)==1
        gausweight(i)=inputs(inputsindex);
        inputsindex=inputsindex+1;
        %otherwise keep definition above
    end
end

%Centers
for i=1:ngaus
    if gauscentersw(i)==1
        gauscenter(i)=inputs(inputsindex);
        inputsindex=inputsindex+1;
        %otherwise keep definition above
    end
end

%FWHM
if gausfwhmsnglsw==0 %different FWHM's
    for i=1:ngaus
        if gausfwhmsw(i)==1
            gausfwhm(i)=inputs(inputsindex);
            inputsindex=inputsindex+1;
            %otherwise keep definition above
        end
    end
elseif gausfwhmsnglsw==1 %same FWHMS's
    if gausfwhmsw(1)==1
        for i=1:ngaus
```

```
            gausfwhm(i)=inputs(inputsindex); %all fwhm equal inputted fwhm
        end
        inputsindex=inputsindex+1;
    else
        for i=1:ngaus
            gausfwhm(i)=gausfwhm(1); %all fwhm equal constant fwhm above
        end
    end
end


%Y offset
for i=1:ngaus
    if gausyoffsetsw(i)==1
        gausyoffset(i)=inputs(inputsindex);
        inputsindex=inputsindex+1;
        %otherwise keep definition above
    end
end

%Fitdata Amplitude
if fitdatasetweightsw==1
    fitdatasetweight=inputs(inputsindex);
    inputsindex=inputsindex+1;
    %otherwise keep definition above
end

%Check fitting parameters (this should be commented out)
% gausweight
% gauscenter
% gausfwhm
% gausyoffset

%Load fit data set
fitdataset=load(fitdatasetpath);

%Normalize fit data set; then multiply by amplitude
fitdataset=en(fitdataset);
fitdataset(:,2)=sqrt(fitdatasetweight^2)*fitdataset(:,2);

%Spline fitdata set onto new x axis
fitdatasetspline=spline(fitdataset(:,1),fitdataset(:,2),xin);

%Build gaussians
for i=1:ngaus
    fitcomp(:,i)=sqrt(gausweight(i)^2)*(exp(-(xin-gauscenter(i)).^2* ...
    4*log(2)/gausfwhm(i)^2)+gausyoffset(i));
end

%Sum gaussians and fit data to get final fit
yfitout=sum(fitcomp,2)+fitdatasetspline;

%Plot if last input was a zero
if length(inputs)==inputsindex
    if inputs(inputsindex)==0
        fighand=figure(1);
        clf
        for i=1:ngaus
            plot(xin,fitcomp(:,i),'--','color',WhatColor(4,4))
```

```
            hold on
        end
        plot(xin,fitdatasetspline,'--','color',WhatColor(4,3))
        plot(xin, yfitout,'color',WhatColor(4,2));
    end
end

%% End Main Code
```

A.7 Globally Fitting Multiple Data Sets

Below is MATLAB code to fit a series of data sets to a global model. The first set of code is a macro (nl_opt.m) which loads the data sets, concatenates them, passes them to the model function, and optimizes the returned fit. The second set of code is the model function (nl_funct.m) which is where the global model is defined.

```
%%%%% nl_opt.m
%% Start Inputs

%Initial guess:
ig;

%Number of Data Files:
numdata=5;

%Data files:

% datafile1='C:\Blank\Thesis\PtOEP\work\Kinetic Fits\fl221.dat';
% datafile2='C:\Blank\Thesis\PtOEP\work\Kinetic Fits\fl227.dat';
% datafile3='C:\Blank\Thesis\PtOEP\work\Kinetic Fits\fl258.dat';

datafile1='C:\Blank\Thesis\PtOEP\work\Kinetic Fits\PtOEP_2_58eVdecay_2_54E19exc_cm3.dat';
datafile2='C:\Blank\Thesis\PtOEP\work\Kinetic Fits\PtOEP_2_58eVdecay_4_12E19exc_cm3.dat';
datafile3='C:\Blank\Thesis\PtOEP\work\Kinetic Fits\PtOEP_2_58eVdecay_7_94E19exc_cm3.dat';
datafile4='C:\Blank\Thesis\PtOEP\work\Kinetic Fits\PtOEP_2_58eVdecay_1_58E20exc_cm3.dat';
datafile5='C:\Blank\Thesis\PtOEP\work\Kinetic Fits\PtOEP_2_58eVdecay_1_93E20exc_cm3.dat';

% datafile6='C:\Blank\Data\Jon\20120523\fl221.dat';
% datafile7='C:\Blank\Data\Jon\20120523\fl227.dat';
% datafile8='C:\Blank\Data\Jon\20120523\fl258.dat';

%CZTS blueshift data:

% datafile1='D:\Blank\Data\20121012 Tom czts small vs large\Small Blueshift\vis_s_200000.dat';
% datafile1='D:\Blank\Writings\20130211 CZTS Paper\large_blueshift_ev.dat';

%Optimization iterations:
its=30;

%Range on x-axis to calculate residual:
% xrmin=fitpar(2)-80;
% xrmax=xrmin+140;
xrmin=0;
xrmax=6E15;

%% End Inputs
```

```
xsize(1)=0;
for i=1:numdata
    eval(['data' num2str(i) '=load(datafile' num2str(i) ');']);
    eval(['data' num2str(i) '=sortrows(data' num2str(i) ',1);']);
    eval(['irmin = nearestvaluei(data' num2str(i) '(:,1)' char(39) ',xrmin);']);
    eval(['irmax = nearestvaluei(data' num2str(i) '(:,1)' char(39) ',xrmax);']);
    eval(['xdata' num2str(i) '=data' num2str(i) '(irmin:irmax,1);']);
    eval(['ydata' num2str(i) '=data' num2str(i) '(irmin:irmax,2);']);
    xsize(i+1)=xsize(i)+irmax-irmin+1;
end

es(xsize);

xdata=[];ydata=[];
for i=1:numdata
    eval(['xdata=[xdata;xdata' num2str(i) '];']);
    eval(['ydata=[ydata;ydata' num2str(i) '];']);
end

options= statset('Display','iter','MaxIter',its,'TolFun',1e-40,'TolX',1e-40);

[fitpar,resid,jac]=nlinfit(xdata,ydata,@nl_funct,ig,options);

confint=nlparci(fitpar,resid,'Jacobian',jac,'alpha',.05);
```

```
function fit=nl_funct(ig,xdata)

%% Start Inputs

%Adjust fit to zero before time zero? (or before x=0) (1=yes, 2=no)
swzfit=1;

%% End Inputs

xsize=load('xsize.dat');
numdata=length(xsize)-1;

%split entered xdata into its parts:
for i=1:numdata
    eval(['xdata' num2str(i) '=xdata(xsize(i)+1:xsize(i+1));']);
end

%calculate seperate fits's:

%%%%% Second Order Kinetics

flu=[.5763E15,.9349E15,1.801E15,3.585E15,4.380E15];
aa=44083;

% fit1=ig(2)*xdata1*aa./(1+2*xdata1*aa*ig(1)*10)+ ...
ig(3)*xdata1*aa.*xdata1*aa*ig(1)*10./(1+2*xdata1*aa*ig(1)*10);
% fit2=ig(4)*xdata2*aa./(1+2*xdata2*aa*ig(1)*10)+ ...
ig(5)*xdata2*aa.*xdata1*aa*ig(1)*10./(1+2*xdata1*aa*ig(1)*10);
% fit3=ig(6)*xdata3*aa./(1+2*xdata3*aa*ig(1)*10);

fit1=ig(2)*flu(1)*aa./(1+2*flu(1)*aa*ig(1)*xdata1);
fit2=ig(3)*flu(2)*aa./(1+2*flu(2)*aa*ig(1)*xdata2);
fit3=ig(4)*flu(3)*aa./(1+2*flu(3)*aa*ig(1)*xdata3);
fit4=ig(5)*flu(4)*aa./(1+2*flu(4)*aa*ig(1)*xdata4);
fit5=ig(6)*flu(5)*aa./(1+2*flu(5)*aa*ig(1)*xdata5);

% fit6=ig(7)*xdata6*aa./(1+2*xdata6*aa*ig(1)*10)+ ...
ig(8)*xdata6*aa.*xdata6*aa*ig(1)*10./(1+2*xdata6*aa*ig(1)*10);
% fit7=ig(9)*xdata7*aa./(1+2*xdata7*aa*ig(1)*10)+ ...
ig(10)*xdata7*aa.*xdata7*aa*ig(1)*10./(1+2*xdata7*aa*ig(1)*10);
% fit8=ig(11)*xdata8*aa./(1+2*xdata8*aa*ig(1)*10);

%set fits below zero to zero
if swzfit==1
    for i=1:numdata
        eval(['tzi=nearestvaluei(xdata' num2str(i) char(39) ',0);']);
        eval(['fit' num2str(i) '(1:tzi)=0;']);
    end
end

%combine y's into returned y:
temps='fit1';
for i=2:numdata
    temps=[temps ';fit' num2str(i)];
end

eval(['fit=[' temps '];'])
```

A.8 Dexter and Förster Fitting Models for TTA

MATLAB code for Dexter and Förster TTA models is given below. These models can be used in the fitting routines given in Appendix A.7. The Dexter model uses a subroutine (annihdexg.m) which numerically approximates the integral, $g(x)$, presented in Equation 6.17.

```
%%%%%%%%% Dexter Energy Transfer leading to annihilation
flu=[.5763E15,.9349E15,1.801E15,3.585E15,4.380E15];
aa=44083;
%
fit1=ig(3)*flu(1)*aa./(1+pi/6*ig(1)^3*flu(1)*aa*annihdexg(ig(2)*xdata1)');
fit2=ig(4)*flu(2)*aa./(1+pi/6*ig(1)^3*flu(2)*aa*annihdexg(ig(2)*xdata2)');
fit3=ig(5)*flu(3)*aa./(1+pi/6*ig(1)^3*flu(3)*aa*annihdexg(ig(2)*xdata3)');
fit4=ig(6)*flu(4)*aa./(1+pi/6*ig(1)^3*flu(4)*aa*annihdexg(ig(2)*xdata4)');
fit5=ig(7)*flu(5)*aa./(1+pi/6*ig(1)^3*flu(5)*aa*annihdexg(ig(2)*xdata5)');
fit6=ig(8)*xdata6*aa./(1+pi/6*ig(1)^3*xdata6*aa*annihdexg(ig(2)*10))+ ...
ig(9)*(xdata6*aa).^2*(pi/12*ig(1)^3*annihdexg(ig(2)*10))./ ...
(1+pi/6*ig(1)^3*xdata6*aa*annihdexg(ig(2)*10));
fit7=ig(10)*xdata7*aa./(1+pi/6*ig(1)^3*xdata7*aa*annihdexg(ig(2)*10))+ ...
ig(11)*(xdata7*aa).^2*(pi/12*ig(1)^3*annihdexg(ig(2)*10))./ ...
(1+pi/6*ig(1)^3*xdata7*aa*annihdexg(ig(2)*10));
fit8=ig(12)*xdata8*aa./(1+pi/6*ig(1)^3*xdata8*aa*annihdexg(ig(2)*10));
%
%%%%%%%%%%%%%%%%%%%%%%%%%%%%%%%%%%%%%%%%%%%%%%%%%%

%%%%%%%%%  Forster Energy Transfer leading to annihilation (IN THESIS)
flu=[.5763E15,.9349E15,1.801E15,3.585E15,4.380E15];
aa=44083;
%
fit1=ig(2)*flu(1)*aa./(1+4*pi^(3/2)/3*ig(1)*flu(1)*aa*sqrt(xdata1));
fit2=ig(3)*flu(2)*aa./(1+4*pi^(3/2)/3*ig(1)*flu(2)*aa*sqrt(xdata2));
fit3=ig(4)*flu(3)*aa./(1+4*pi^(3/2)/3*ig(1)*flu(3)*aa*sqrt(xdata3));
fit4=ig(5)*flu(4)*aa./(1+4*pi^(3/2)/3*ig(1)*flu(4)*aa*sqrt(xdata4));
fit5=ig(6)*flu(5)*aa./(1+4*pi^(3/2)/3*ig(1)*flu(5)*aa*sqrt(xdata5));
fit6=ig(7)*xdata6*aa./(1+4*pi^(3/2)/3*ig(1)*xdata6*aa*sqrt(10))+ ...
ig(8)*2*pi^(3/2)/3*ig(1)*(xdata6*aa).^2*sqrt(10)./(1+4*pi^(3/2)/3*ig(1)*xdata6*aa*sqrt(10));
fit7=ig(9)*xdata7*aa./(1+4*pi^(3/2)/3*ig(1)*xdata7*aa*sqrt(10))+ ...
ig(10)*2*pi^(3/2)/3*ig(1)*(xdata7*aa).^2*sqrt(10)./(1+4*pi^(3/2)/3*ig(1)*xdata7*aa*sqrt(10));
fit8=ig(11)*xdata8*aa./(1+4*pi^(3/2)/3*ig(1)*xdata8*aa*sqrt(10));
%
%%%%%%%%%%%%%%%%%%%%%%%%%%%%%%%%%%%%%%%%%%%%%%%%%%
```

```
function g=annihdexg(x)

% The g(x) function used in dexter TTA calculations.
An approximation of: g(x) = -x*int(exp(-xy)*(ln(y))^3,y=0..1)

%size of x
n=length(x);

%vector for summing if x is small
m=[0:50];

for i=1:n
    %if x is small, expand the integrand and term-by-term integrate
    if x(i) < 7
        g(i)=6*x(i)*sum((-x(i)).^m./(factorial(m).*(m+1).^4));
    %if x is not small use equation from Inokuti
    else
        g(i)=log(x(i))^3+1.73164699*log(x(i))^2+5.93433597*log(x(i))+5.44487446;
    end
end
```